



Terms and Conditions of Use of Digitised Theses from Trinity College Library Dublin

Copyright statement

All material supplied by Trinity College Library is protected by copyright (under the Copyright and Related Rights Act, 2000 as amended) and other relevant Intellectual Property Rights. By accessing and using a Digitised Thesis from Trinity College Library you acknowledge that all Intellectual Property Rights in any Works supplied are the sole and exclusive property of the copyright and/or other IPR holder. Specific copyright holders may not be explicitly identified. Use of materials from other sources within a thesis should not be construed as a claim over them.

A non-exclusive, non-transferable licence is hereby granted to those using or reproducing, in whole or in part, the material for valid purposes, providing the copyright owners are acknowledged using the normal conventions. Where specific permission to use material is required, this is identified and such permission must be sought from the copyright holder or agency cited.

Liability statement

By using a Digitised Thesis, I accept that Trinity College Dublin bears no legal responsibility for the accuracy, legality or comprehensiveness of materials contained within the thesis, and that Trinity College Dublin accepts no liability for indirect, consequential, or incidental, damages or losses arising from use of the thesis for whatever reason. Information located in a thesis may be subject to specific use constraints, details of which may not be explicitly described. It is the responsibility of potential and actual users to be aware of such constraints and to abide by them. By making use of material from a digitised thesis, you accept these copyright and disclaimer provisions. Where it is brought to the attention of Trinity College Library that there may be a breach of copyright or other restraint, it is the policy to withdraw or take down access to a thesis while the issue is being resolved.

Access Agreement

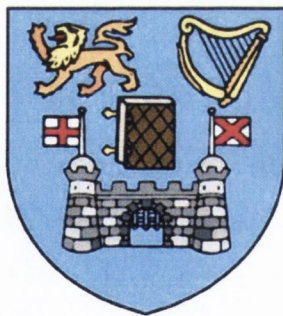
By using a Digitised Thesis from Trinity College Library you are bound by the following Terms & Conditions. Please read them carefully.

I have read and I understand the following statement: All material supplied via a Digitised Thesis from Trinity College Library is protected by copyright and other intellectual property rights, and duplication or sale of all or part of any of a thesis is not permitted, except that material may be duplicated by you for your research use or for educational purposes in electronic or print form providing the copyright owners are acknowledged using the normal conventions. You must obtain permission for any other use. Electronic or print copies may not be offered, whether for sale or otherwise to anyone. This copy has been supplied on the understanding that it is copyright material and that no quotation from the thesis may be published without proper acknowledgement.

Computational Studies of the Structure and Dynamics of Packings of Grains and Bubbles

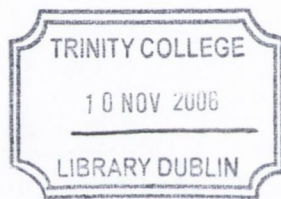
by
Gary Delaney

A Thesis submitted to
The University of Dublin
Trinity College
for the degree of
Doctor of Philosophy



SCHOOL OF PHYSICS
UNIVERSITY OF DUBLIN
TRINITY COLLEGE

2006



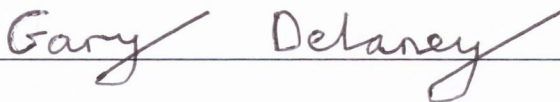
THESIS
8002.

Declaration

This thesis has not been submitted as an exercise for a degree at any other University.

Except where otherwise stated, the work described herein has been carried out by the author alone.

This thesis may be borrowed or copied upon request with the permission of the Librarian, Trinity College Dublin, University of Dublin. The copyright belongs jointly to the University of Dublin and Gary Delaney.



Gary Delaney

Dublin 02.05.2006

Summary

Since the dawn of civilization people have been intrigued by packing problems. They have a great significance in the practicalities of our everyday lives, with people always seeming to try to find more efficient ways of packing things together. Even though scientists have studied them for over 2,500 years, they are still prevalent today in almost every area of science. Much of the work that scientists have done on packing problems to date has been in considering sphere packings. These have been used widely to investigate the properties of granular materials and as simple models for everything from packings of atoms to packings of bubbles.

We shall begin by considering one of the simplest granular systems (and indeed one of the simplest packings of spheres) by performing the most detailed examination to date into the physics of Newton's Cradle. This simple system is shown to exhibit many complex dynamic effects that give insights into the general behaviour of granular materials and highlight how seemingly simple systems can exhibit complex behaviour.

The theme of sphere-packing is continued when we consider bubble packings in the wet foam limit. These packings are composed of almost spherical bubbles that have been observed experimentally to demonstrate a surprising degree of order. We consider the similarities between these systems and computationally generated sphere packings. We also perform two-dimensional simulations of packings of bubbles trapped between glass plates. The control of the position of the bubbles in the packing is being investigated as a potential technology with applicability to the emerging area of Discrete Microfluidics.

Packing models composed of spheres are characterised by forces that act under compression only with dense hard-sphere packings for instance not being able to withstand expansions of the system but may withstand compressions. We turn the traditional packing model "inside-out" by defining a system where interactions

act under extension only. This system is seen to exhibit an onset of rigidity for sufficient expansions that may in some sense be considered to be the inverse of the onset of ‘jamming’ in compressed soft sphere systems.

We also go beyond traditional sphere packing models, by considering the important role that shape plays in packings of grains. The author has created a software program called `ARBITRARYPACKER` that allows for the investigation of the packing properties of grains of arbitrary shape. The properties of random packings of elliptical grains is investigated, with a very interesting variation in the packing density of the grains observed as the ellipticity is varied.

Sequential packing of grains is considered and a new model that incorporates the rotational degree of freedom of asymmetric objects is investigated. We also present a new model which we term “Packing-driven shape evolution of grains”, where the shape evolution of the grains is determined by how they pack together in a dense random packing.

Acknowledgments

Firstly I would like express my gratitude to my supervisor, Dr. Stefan Hutzler, whose expertise, enthusiasm, drive and support was invaluable throughout the carrying out of the research that this thesis now presents. I thank Prof. Denis Weaire for his guidance and support which added greatly to my graduate experience. I would like to gratefully acknowledge Dr. Simon Cox for his technical assistance with all things Surface Evolver and Wiebke Drenckhan and Antje van der Net for their experimental expertise. I would also like to thank Prof. John Hinch for very helpful discussions on Newton's Cradle.

A big thanks goes to the enthusiastic and dedicated project students who worked with me during the course of my PhD: Robert Clancy, Seamus Murphy, David Barrett and Edmond Daly.

Thank-you to all the members of our group who provided helpful discussions and support: Eric, Vincent, Norbert, Lola, Aengus and in particular Finn MacLeod, who wrote the original code I used to model Newton's cradle.

A very personal thanks goes to all my friends who supported me and made Trinity College such a great place to be: Aaron, Cathal, Ciara, Colin, Denis, John, Lorna, Martin, Orla, Rory and Siobhan.

Special thanks go to:

- Laura for the laughs, the dinners and all the things that went with salt and lemon!
- Jennie and Paul for many great times and providing the best day out I had in College!

- Barry, Eibhlin, James, Paul, Peter, Debbie, Johnny and Zillah for more great nights than I could count.
- Clare for great nights and great holidays.
- Laina for being a brilliant holiday buddy.
- Gemma - my support scientist, my vice-convenor and lots lots more.
- Iain for many helpful technical and scientific conversations and for being a great friend over many years.

Thank-you to all the members of rooms 4.03 and 2.22 for making the office a great place to be: Aron, Berry, Ben, Michael, Paul and James.

I would like to acknowledge computational support from IITAC, the Trinity Center for High Performance Computing and the Irish Center for High End Computing.

Financial support for this PhD was provided by Enterprise Ireland Research Grant SC/2002/0011 and a Trinity College Postgraduate Award.

Many thanks to Sonya for being everything anyone could wish for in a Sister and to Andrew for making her so happy.

And finally to my parents, who supported me in so many ways throughout my education and to whom I dedicate this thesis.

Publications

G. Delaney, D. Weaire and S. Hutzler. Onset of rigidity for stretched string networks, *Europhysics Letters*, **72**, 990-996, 2005.

W. Drenckhan; S.J. Cox, G. Delaney, H. Holste; D. Weaire and N. Kern. Rheology of ordered foams on the way to Discrete Microfluidics, *Colloids And Surfaces A-Physicochemical And Engineering Aspects*, **263** 52-64, 2005.

G. Delaney, D. Weaire, S. Hutzler and S. Murphy. Random packing of elliptical disks. *Philosophical Magazine Letters*, **85** 2005, 89-96, 2005.

S. Hutzler, G. Delaney, D. Weaire and F. MacLeod. Rocking Newton's cradle. *American Journal Of Physics*, **72** 2004, 1508-1516, 2004.

Contents

1	Introduction	1
1.1	The importance of packing to us all	1
1.2	Sphere Packings	2
1.3	The role of shape	5
1.4	Jamming, constraints and contact numbers	6
1.5	Packing inside-out	7
1.6	Sequential packing models	8
1.7	Bubble packings and foams	9
1.8	Application of Computational Methods.	10
1.9	Writing Style	13
2	Newton's Cradle	15
2.1	Introduction	15
2.2	Modeling Newton's cradle	19
2.3	Results	22
2.4	Theory of a two-ball cradle	25
2.5	The effects of dissipation	30
2.6	Experiments	34
2.7	Conclusion	39
3	Random Packing of Elliptical Disks	41

3.1	Introduction	41
3.2	Simulation of 2D packings of ellipses	42
3.3	Results and Analysis	45
3.4	Conclusion	50
4	Packing Limited Growth	51
4.1	Introduction	51
4.2	Theory	53
4.3	Computational Implementation	56
4.4	Simulation Results	57
4.4.1	The transition from straight edged to circular objects	60
4.4.2	The role of ellipticity	62
4.4.3	Concave objects considered	64
4.5	Conclusion and Outlook	67
5	Packing-driven shape evolution of grains.	71
5.1	Introduction	71
5.2	Description of the Model	74
5.3	Measures of Shape	76
5.4	Simulation Results	77
5.4.1	Short Term Simulations	80
5.4.2	Long Term Simulations	85
5.4.3	Sundry parameter variations	91
5.5	Discussion and Conclusion	94
6	The inverse packing problem	99
6.1	Introduction	99
6.2	Simulation Technique	101
6.3	Simulation results for the triangular lattice	103

6.4	Interpretation	106
6.5	Results for the square lattice	107
6.6	Results for the hexagonal lattice	109
6.7	Conclusion	110
7	3D sphere and bubble packings	113
7.1	Introduction	113
7.2	Bubbles in the Wet Foam Limit	116
7.3	Random Sphere Packing	117
7.4	Dynamic sphere packing model	118
7.5	Simulation Results	120
7.5.1	Formation of a surface layer	120
7.5.2	Deposition of spheres onto a triangular packing	122
7.5.3	Deposition of spheres onto a square packing	125
7.5.4	Formation of an ordered surface layer	127
7.6	Discussion	128
8	Flow of Ordered Arrays of Bubbles	133
8.1	Introduction	133
8.2	Manipulation of ordered arrays of bubbles	134
8.2.1	Adding/removing or replacing bubbles	135
8.2.2	Sorting of bubbles into different branches of a network	135
8.2.3	Controlled neighbour switching in a U-bend	137
8.2.4	Success of traditional simulation techniques	138
8.3	Viscous Froth Model	139
8.3.1	Quasi-static Soap Froth	139
8.3.2	Grain growth	141
8.3.3	Computational Implementation	142

8.3.4	The Dimensionless Viscous Froth Equation	143
8.3.5	Curvature	143
8.3.6	Determination of Bubble Pressures	144
8.3.7	Velocities and Displacement	146
8.4	Simulation Results	146
8.5	Variation of system parameters	151
8.5.1	Variation of the radius of the bend	152
8.5.2	Variation of the width of the tube	153
8.5.3	Variation of the area of the bubbles	155
8.5.4	Determining the viscous drag parameter λ	157
8.6	Conclusion	159
9	Conclusion and Outlook	161
A	Scaling relationships in PLG models.	165
B	RAP and RRAP simulations.	169
C	Implementation of a Cell List	173

List of Figures

1.1	Order of layers in HCP packing (ABABABA) and FCC packing (ABCBCA).	3
1.2	A simulation of a random packing of 500 spheres with packing fraction $\Phi = 0.637$.	4
1.3	The Apollonian packing.	8
1.4	The Kelvin Structure and the Weaire-Phelan Structure.	9
1.5	RAP packing of pentagons.	12
2.1	Diagram of Newton's cradle.	16
2.2	The overlap of two balls.	19
2.3	Displacement of the balls as a function of time.	22
2.4	A detailed view of the first three sets of collisions.	23
2.5	Long-time behavior of the dissipation-free $N = 5$ cradle.	24
2.6	Plot of the relative position X_r for the $N = 2$ cradle as a function of time.	27
2.7	Collision points for the $N = 2$ system	28
2.8	Two phase portraits that characterize the motion of the $N = 2$ cradle.	29
2.9	Energy variation in the dissipative cradle.	31
2.10	Loss of energy due to the Stokes damping and viscoelastic dissipation for the $N = 5$ cradle.	32
2.11	Experimental data for Newton's cradle with $N = 2, 3,$ and 4 balls.	34

2.12	Variation of the amplitude of ball 1 in a $N = 2$ cradle with time. . . .	35
2.13	Variation in amplitude of ball 1 for the $N = 3$ cradle.	36
2.14	Variation in amplitude of ball 1 for the $N = 4$ cradle.	37
2.15	Variation in amplitude of ball 1 for a $N = 2$ cradle with a 1 mm gap between the rest positions of the balls.	38
3.1	Computer simulations of dense packings of ellipses.	43
3.2	Variation of packing fraction Φ with $1 - \lambda$	45
3.3	Variation of packing fraction for system without ellipse rotations. . .	46
3.4	Variation of number of contacts, Z , with distance from edge of disks. .	47
3.5	Variation of the average contact number with aspect ratio.	48
4.1	RAP and RRAP packings of triangles and squares.	54
4.2	The decay of the pore space volume for triangles, pentagons and oc- tagons.	58
4.3	Plot of $N(r)$, the frequency of objects of size r , for triangles, pen- tagons and octagons.	59
4.4	The transition from straight edged to circular objects.	60
4.5	Variation of exponents β and β' for triangle to circle transition. . . .	61
4.6	RRAP packings of ellipses	63
4.7	Variation of exponents β and β' with ellipticity.	64
4.8	Concave objects considered.	65
4.9	RAP and RRAP packings of concave objects	66
4.10	Variation of exponents β and β' with the concaveness γ of the object. .	67
5.1	Flow diagram for erosion model.	74
5.2	Images of order of events in simulation.	75
5.3	Evolution of the shapes of the grains for a short term simulation . . .	78

5.4	Images show the evolution of the shapes of the grains for a short term simulation with $\Delta\Phi' = 0.02$ and $\Delta\Phi' = 0.03$	79
5.5	Variation of packing fraction with number of iterations for short term simulation.	80
5.6	Variation of convexity ratio with number of iterations.	81
5.7	Variation of the standard deviation σ_{area} of the areas of the grains with number of iterations.	82
5.8	Variation of the average area-perimeter ratio f_{AP} with number of iterations.	83
5.9	Shape evolution of the of the grains for a long term simulation.	84
5.10	Variation of the packing fraction Φ with iteration number.	85
5.11	Variation of the convexity ratio f_C with number of iterations for a long term simulation.	86
5.12	Variation of the standard deviation σ_{area} of the area of the grains with number of iterations for a term simulations.	87
5.13	Variation of the average area-perimeter ratio f_{AP} of the grains with number of iterations for long term simulations.	88
5.14	Images of simulations with large initial range of radii.	89
5.15	Images of simulations using elliptical grains.	90
5.16	Shape evolution of two grains during the long term simulation.	93
6.1	Expansion of a triangular lattice.	100
6.2	Increase in the number of taut strings as the periodic box is expanded, for a triangular lattice with 49152 strings.	102
6.3	Average coordination number for a Triangular lattice above the threshold of rigidity.	103
6.4	Variation in the fraction of vertices with coordination numbers $z = 2$ to $z = 6$ as the network is expanded.	104

6.5	Variation of the average coordination number Z_{crit} at the threshold of rigidity.	105
6.6	Disregarding vertices with coordination $z \leq 2$	106
6.7	Expansion of a square lattice.	108
6.8	Variation in the fraction of vertices with coordination numbers $z = 2$ to $z = 6$ for a square lattice.	109
6.9	Expansion of a hexagonal lattice.	110
6.10	Variation of the average coordination number Z_{crit} at the threshold of rigidity for a hexagonal lattice.	111
<hr/>		
7.1	Packings of bubbles in wet foam.	115
7.2	Ordered terraces at the bottom of the packing of bubbles.	115
7.3	Forces on spheres in the dynamics simulation.	118
7.4	Formation of the surface layer.	121
7.5	Packing onto a triangular layer.	122
7.6	Vertical density variation for sphere packings onto a triangular packed layer.	123
7.7	Ordered packings generated by sequential addition of spheres.	124
7.8	Packings generated by allowing spheres to settle on a fixed square packed layer.	125
7.9	Vertical density variation for the sphere packing onto a fixed square packed layer.	126
7.10	Formation of an ordered surface layer using an attractive force between the surface spheres.	127
8.1	Replacement of bubbles by controlling flow/pressure in the channels.	135
8.2	Two rows of bubbles are sorted into two narrow channels.	135
8.3	An asymmetric neck is used to rearrange the bubbles/	136

8.4	Diagram showing a neighbour switching T1 process.	137
8.5	A phase shift in order of the bubbles caused by passing around a U-bend.	137
8.6	Forces acting on a film segment of length l	140
8.7	Flow diagram for viscous froth simulation.	142
8.8	The curvature K , at the point where edges e_1 and e_2 meet.	144
8.9	Comparison of the distortion of a foam structure going around a bend.	147
8.10	Case 1: The leading 3 sided bubble is on the outside as the bubbles enter the bend.	149
8.11	Case 2: The leading 3 sided bubble is on the inside as the bubbles enter the bend.	149
8.12	Case 3: The third possibility is that the tube is already filled with bubbles, before the bubbles start to be pushed.	149
8.13	T1 process for Case 1.	150
8.14	T1 process for Case 2.	151
8.15	Variation of the critical T1 velocity v_{crit} with the radius of the tube.	152
8.16	Variation of the critical T1 velocity v_{crit} with the width of the tube for the case of the leading outer bubble (case 1).	154
8.17	Variation of the critical T1 velocity v_{crit} with the width of the tube for the case of the leading inner bubble (case 2).	154
8.18	Variation of the critical T1 velocity v_{crit} with the area of the bubbles for case 1.	156
8.19	Variation of the critical T1 velocity v_{crit} with the area of the bubbles for case 2.	156
8.20	The shortest edge length L as a function of foam flow velocity v around the U-bend.	158
8.21	Determination of the viscous drag parameter λ	159

B.1	Variation of exponents α and α' for triangle to circle transition.	169
B.2	Variation of exponents α and α' with ellipticity.	170
B.3	Variation of exponents α and α' with the concaveness γ of the object.	170
C.1	Use of a cell list for a RAP packing of triangles.	173
C.2	Implementation of a cell list.	174

Chapter 1

Introduction

1.1 The importance of packing to us all

The problem of how objects pack together has been of interest to scientists for millennia [8]. Indeed Bernal remarked that the problem of packing objects into a container is one of the oldest problems known to man [12]. It can be of importance in all our daily lives, from when we try to squeeze those last souvenirs into our suit cases to times when we ponder upon how the bees know how to pack their honey cells together [97].

Packing problems are still prevalent today in almost every area of science. Physicists investigate with how things fit together in nature. Mathematicians concern themselves with the theoretical aspects of packing, expending great energy at times attempting to prove what type of packing is best in a given situation [47]. Chemists have historically had great success in taking a Newtonian view and considering how atoms pack together, relating this structure to the observed physical and chemical properties of substances [8]. Biologists even consider the geometrical contribution to the structure of living things, for example considering the cellular packing structures of biological cells [100, 40].

We are surrounded in our everyday lives by granular packings, from the grains of sand on the beach to the box of cereal that sits on the breakfast table [56]. They play an important role in a great number of our industries, including construction, mining and pharmaceuticals [26]. They also have great importance in geological processes which can have a great impact on all our lives. The study of granular packings gives great insights into the physical mechanisms of landslides, erosion and even plate tectonics, where the dense packing of the Earth's plates is considered [55].

1.2 Sphere Packings

Often in the packing problems found in nature, as in life, the goal is maximum density. Indeed, the dense packing of hard objects is a recurrent paradigm in physics, from early models of crystallinity to modern theories of granular materials which are under active debate today [8, 66]. Generally speaking the objects are taken to be spheres in three-dimensions (or circular disks in two dimensions), leading to the formulation of the Kepler Problem: what is their densest packing?. When considering questions of the density of packings we refer to the packing fraction Φ . For a 2D packing of circles, this is simply the area covered by the circles divided by the total area, while in the 3D case of spheres, it is the volume of the spheres divided by the total volume.

For circular disks, the answer to the Kepler problem is a triangular packing with packing fraction $\Phi = 0.906$. For spheres the answer has long been *known* to be the f.c.c. or h.c.p structures, both with packing fraction $\Phi = 0.7404$. (However the proof of this problem eluded mathematicians for centuries, until Thomas Hales finally produced a complete proof in 1998 [47].) These structures are formed by packing layers of spheres in the triangular packing configuration. However as shown in Figure 1.1, when we consider a triangular packed layer, there is a choice of two

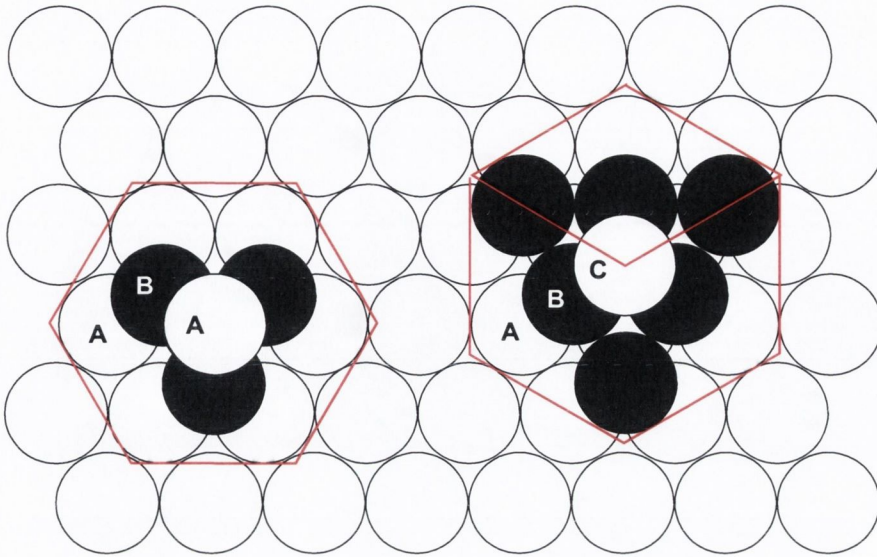


Figure 1.1: Order of layers in HCP packing (ABABABA) and FCC packing (ABCABCA).

different locations in which the next layer can be placed, the layer B or layer C positions. For hexagonal close-packed (hcp) structures, the sequence ABABAB... is followed, while for cubic close-packed (fcc) the sequence is ABCABC...

When we consider disordered packings the problem becomes yet more complicated. In 2D, monodisperse circular discs have a very high tendency to order, quite easily finding the triangular structure. However if a small amount of polydispersity is introduced, then the resulting packing will show a high degree of disorder, and in general for a dense packing only achieve the random close packing of circles value of $\Phi \approx 0.84$ [75, 7].

Bernal began the investigations by Physicists into disordered packings of spheres [12]. However it still remains difficult to give a precise definition of “densest random packing” of spheres [96]: nevertheless it is a concept to which the Physicist has become accustomed and one that is supported by the approximate reproducibility of the density found in a variety of experimental and computational procedures . It may be estimated as $\Phi = 0.64 \pm 0.01$, where the uncertainty reflects a small variation

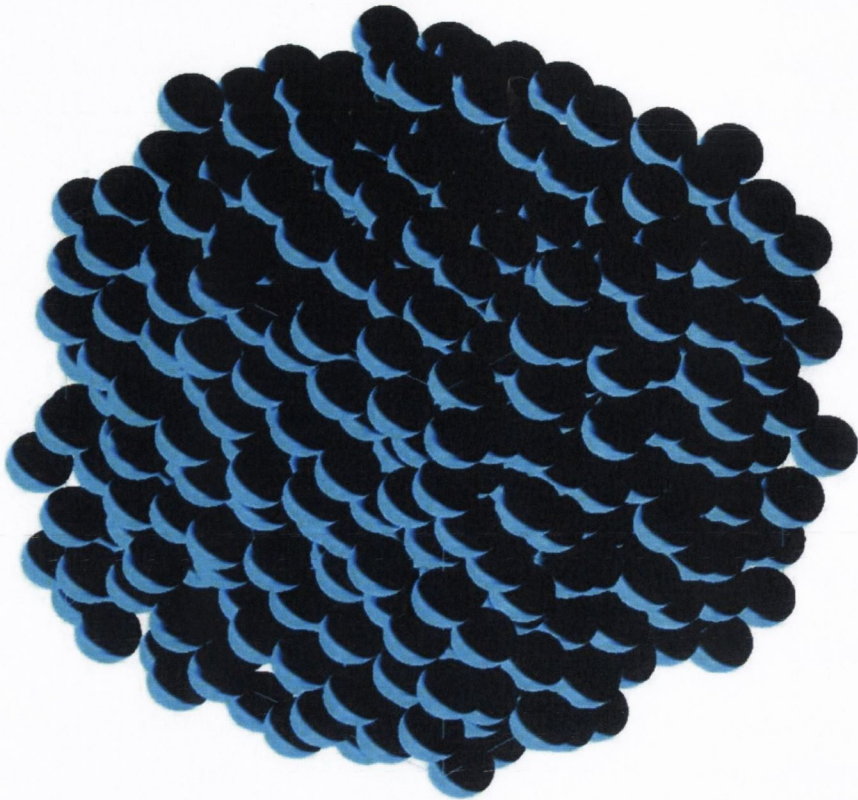


Figure 1.2: A simulation of a random packing of 500 spheres with packing fraction $\Phi = 0.637$.

in dense packings prepared by one procedure to another (See Figure 1.2) [88, 12]. While significant, this variation is small compared to the difference between random and ordered packings.

If we consider a finite number of spheres confined within a box, at low packing fractions Φ , if we shake the box, each sphere can move without impediment from its neighbours. If we reduce the size of the box, eventually a packing fraction will be reached where the system will resist further compression, with each grain locked in position by the grains that it contacts with. Exactly the packing fraction at which this happens will depend upon many factors including the relative size of the spheres and the box, the shape of the box and exactly how we treat the system during the

packing process. If the container is shaken while we pour the spheres into it, the shaking helps to optimise the packing and a packing fraction of $\Phi \approx 0.64$ can be achieved. However, when spheres are gently rolled into a stationary container a packing fraction of $\Phi \approx 0.60$ is obtained. While attempts at measuring the loosest random packing (LRP) of spheres using neutrally buoyant spheres in liquid have found a value of $\Phi \approx 0.56$ [84].

Recently new insights into the structure of random sphere packings have been made using X-ray computed tomography of packings of up to 150,000 mono-sized spheres with packing densities ranging from 0.58 to 0.64 [6, 5, 4]. These studies have among other things shown that disordered sphere packings can be locally more efficient than the fcc and hcp crystal packings, yet more evidence of the large number of interesting effects that can be seen in sphere packings.

1.3 The role of shape

Computational studies of random packing of particles have focused on the simulation of sphere packings. This is the natural choice, as spheres allow a single simple calculation to determine when two grains are in contact. However, most granular materials do not consist of exactly spherical particles, and their shapes must play a role in their properties - even the most basic property, namely density [29, 33]. Little has been done on such cases, because it is computationally demanding to deal with the conditions of contact of irregular bodies. We utilise an approach that discretises the edges of the objects, allowing us to consider random packings of objects of arbitrary shape. In Chapter 3, we consider dense random packings of ellipses, investigating the transition in the packing properties as the shape transitions from circular to highly elliptical.

The shape of the individual elements that make up granular packings observed

in nature changes over time. This is due both to the interactions of the grains with one another and interactions with their surroundings. We could for example consider beach pebbles, which are subject to erosion from both their interactions with the sea and with each other [67, 38]. In Chapter 5 we will consider a model in which the shape of randomly packed two-dimensional grains are allowed to evolve based on how the grains themselves pack together. This model consists of successive generation of dense random packings of grains and the removal of small amount of each of grain where it contacts with its neighbouring grains. It is thus the structure of the packing of the grains itself which determines the shape evolution of the grains. Full details of the implementation of this model are given in Chapter 5.

1.4 Jamming, constraints and contact numbers

For a given configuration of particles, there exists a threshold packing fraction Φ_c at which jamming occurs, where the particles can no longer avoid each other and the bulk and shear moduli simultaneously become nonzero [79, 81] Attempts have been made to give a strict definition of jamming, based on three hierarchical jamming categories that range from “locally jammed”, where each particle is trapped by its neighbours, to “collectively jammed” where no subset of particles can simultaneously be displaced so that its members move out of contact with all particles, to “strictly jammed” where no globally uniform volume-nonincreasing deformation of the system boundary is possible [96, 36]. A recent analysis of computationally generated packings of particles found that random sphere packings with $\Phi \approx 0.64$ and random bi-disperse disk packings with $\Phi \approx 0.84$ were for practical purposes strictly jammed [36].

The standard arguments for the mean number of contacts of each particle in a random packing (due to James Clerk Maxwell [71] and Charles Bennett [11]) have

been based on the concept of jamming. They consider that to constrain the system, two contacts per degree of freedom are required. Thus for a random packing of circles with two degrees of freedom (the two coordinates describing the position of the circle) one would expect a mean contact number of 4. While for an asymmetric object in 2-d one would expect a mean contact number of 6 (the extra degree of freedom being given by the angle describing the object's orientation). These simple arguments that equate the number of contacts an object makes with its available degrees of freedom infer a discontinuous jump in contact number with the addition of an infinitesimal degree of asymmetry. This is in contrast to the smooth transition that we observe when we consider the transition from circles to highly elliptical objects in Chapter 3.

1.5 Packing inside-out

Packing models are characterised by forces that act under compression only [81, 35, 82]. Jammed hard-particle packings for instance cannot withstand expansions of the system but may withstand compressions. Commonly considered models of compression of randomly packed soft disks and spheres are founded on Hooke's Law interactions which act under compression only. We will begin considering these forces in Chapter 2 when we consider the behaviour of the spheres in a Newton's Cradle and give further consideration when we examine sphere packings in Chapter 7. We will also turn this model "inside-out" in Chapter 6, by defining Hooke's Law interactions under extension only, and hence a model of elastic strings that are loose under compression [30]. These systems exhibit an onset of rigidity for sufficient expansions that may in some sense be considered to be the inverse of the onset of 'jamming' in compressed soft sphere systems.

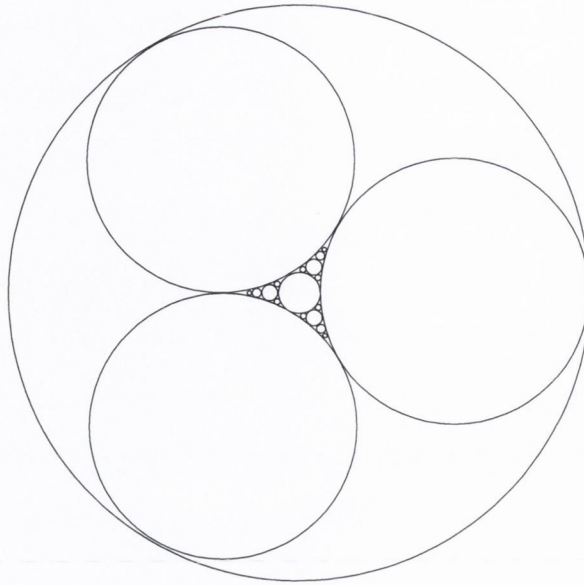


Figure 1.3: The Apollonian packing. This packing is formed by filling the space between three mutually touching discs by placing a disc so that it just touches the other three. The procedure is then continually repeated, filling the new gaps generated by the addition of each new disc.

1.6 Sequential packing models

There exists many space filling packing models in which non-overlapping units of smaller and smaller sizes are placed according to a given set of rules. The oldest known packing of this kind is the Apollonian packing (AP) introduced by Apollonius of Perga around 200 BC [37]. (See Figure 1.6). This packing is formed by filling the space between three mutually touching discs by placing a disc so that it just touches the other three. The procedure is then continually repeated, filling the new gaps generated by the addition of each new disc. Apollonian packing leads to a dense system, with the size of the circles inserted into the pores becoming smaller and smaller and the packing fraction approaching $\Phi = 1$ in the limit of an infinite packing. This model has been generalised to consider the case where the object centers are chosen randomly (RAP) [39]. Using our approach of considering objects

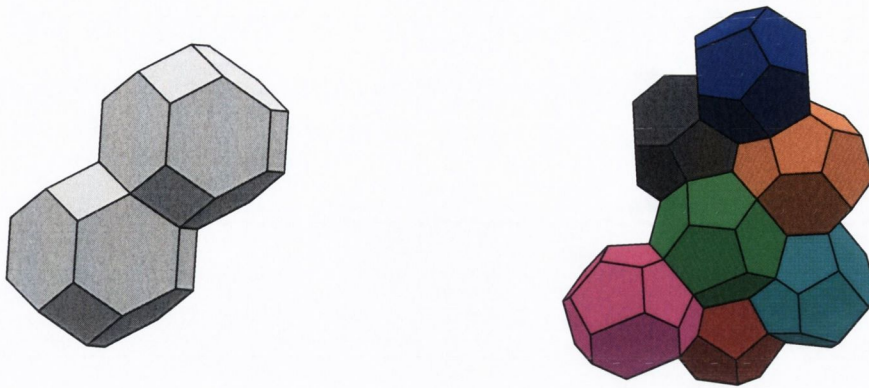


Figure 1.4: In 1887, Lord Kelvin posed the problem of how to pack cells of equal volume such that the total area of the interfaces between the cells is a minimum. His solution, the Kelvin Structure (Left), stood for over a century until in 1993 the Weaire-Phelan structure (Right) was discovered, beating Kelvin's partition by 0.3% in area [106]. (Images generated using the Surface Evolver).

with discretised edges, we will consider the behavior of the RAP model for objects with various shapes in Chapter 4. We will also define a new model in which the objects are allowed to rotate during the packing process. We will term this new model Rotational Random Apollonian Packing (RRAP).

1.7 Bubble packings and foams

When we consider packings of bubbles, like those in a glass of beer, the system has a more subtle behaviour than the simple achievement of maximum density. When the bubbles are packed tightly together they form a foam, adjusting their shape in an attempt to minimise their surface area. (We will consider the behaviour of such bubble packings in Chapter 8). In these cases the water from the foam drains out under gravity, leaving a dry foam composed of a disordered packing of bubbles of polyhedral shape. The exact shape of the bubbles depends very strongly on the liquid fraction, but for dry foams even when monodisperse bubbles are used the packing of

bubbles are highly disordered, except for where the packings are generated in vessels or channels of small dimension, with only a very low number of bubbles spanning the diameter of the channel [54].

The behaviour of these foam systems are closely linked to the problem posed by Lord Kelvin in 1887, that of how to pack cells of equal volume such that the total area of the interfaces between the cells is a minimum (See Figure 1.6). His solution, the Kelvin Structure, stood for over a century and is indeed observed in confined dry monodisperse foams [54]. However in 1993 the Weaire-Phelan structure was discovered, beating Kelvin's partition by 0.3% in area [106]. This structure is not observed in foam systems.

The effect of gravity driven drainage is greatly reduced as the size of the bubbles is decreased. This allows one, when using sufficiently small bubbles, to generate a very wet foam composed of spherical bubbles, a system with a very strong analogy to the classically considered systems of sphere packings. When such packings of bubbles are created they show a very large degree of ordering. We will consider such packings in Chapter 7, comparing and contrasting their behaviour with simulation results for sphere packings.

1.8 Application of Computational Methods.

The Surface Evolver

There is a long history of the application of computational methods to the study of granular packings and to the study of bubbles and foams [104, 95]. A key software tool used by the foam community is the Surface Evolver [15]. This software was written by Ken Brakke more than 20 years ago and is still under active development. Surface Evolver is an interactive program for the study of surfaces shaped by surface tension and other energies and has been widely applied to the study of foams. Using

this software a user is able to define the foam structure and evolve it toward a minimal surface energy by a gradient descent method.

Surface Evolver can also be used to implement other models using its command language. The advantage of this approach is that one can take advantage of Surface Evolver's topological book keeping (for definitions of vertices, edges, bubbles etc.) and its implementation of a highly optimised minimisation routine. This approach was taken by Simon Cox when implementing a dynamic model (the Viscous Froth Model) for the evolution of 2d foams subject to viscous forces and we utilise this implementation in Chapter 8.

We also make novel use of the Surface Evolver when we consider the inverse packing problem in Chapter 6. We modified Surface Evolver's source code to make the Hookean spring interaction defined in the code one-sided. We were then able to take advantage of Surface Evolver's implementation of periodic boundary conditions, and its built in optimised minimisation routines.

Packing of Arbitrary Shapes.

We have developed a software program called `ARBITRARYPACKER`, that allows us to consider the packing behaviour of arbitrarily shaped grains in 2D. The software is written in the C programming language with graphics generated using *OPENGL* [25]. At the core of the software is the definition of the shape of 2D objects as polygons and the utilising of a polygon library *CLIPPOLY* [74] to determine when objects are in contact and the degree to which their areas overlap. Details of the various computational models implemented in `ARBITRARYPACKER` are given in the relevant Chapters and Appendix C gives details of the cell list technique used to greatly increase performance for sequential packing models.

Using this program we are able to generate dense jammed random packings of grains of any desired shape using a monte-carlo technique [93]. This is used in

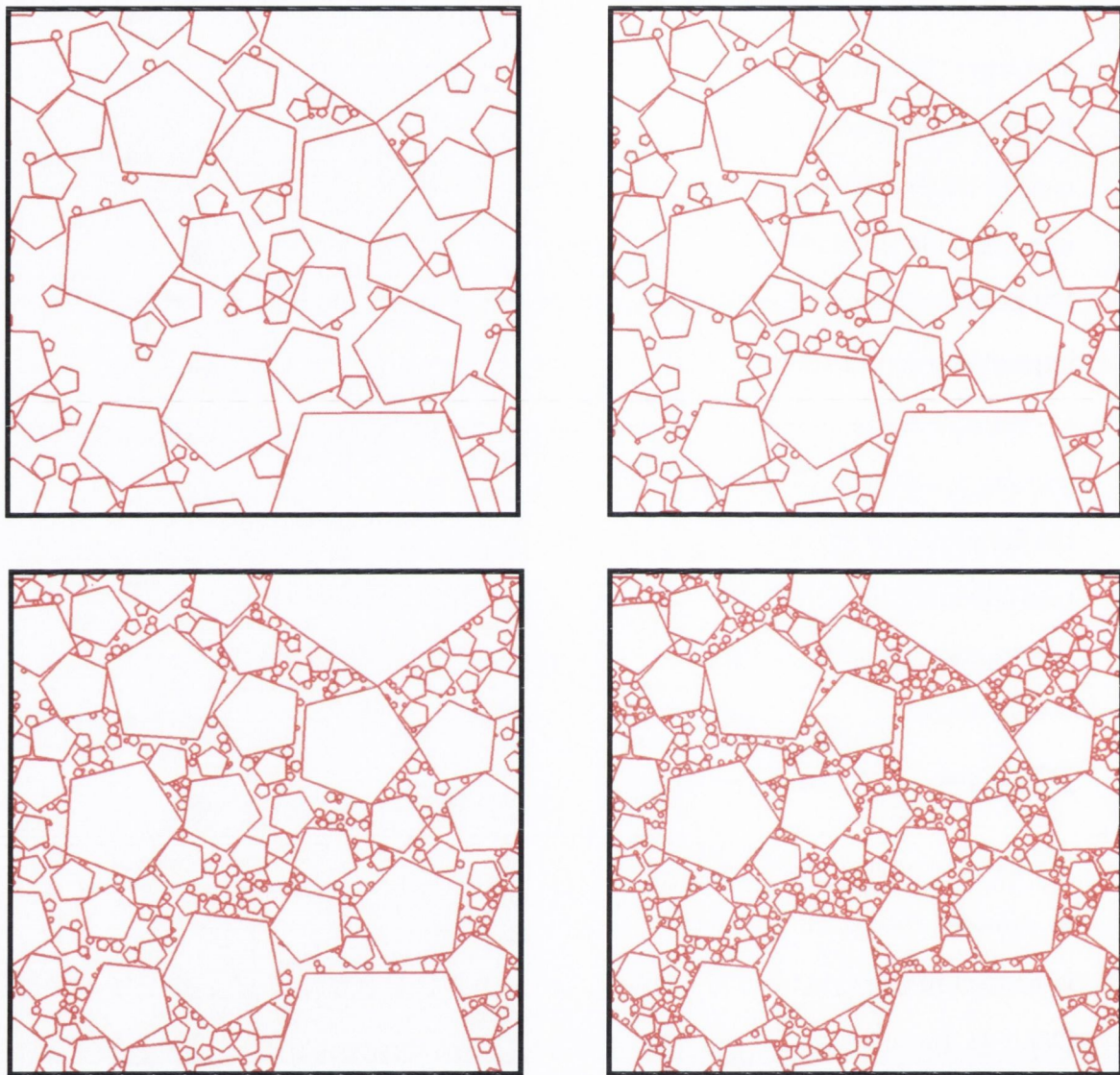


Figure 1.5: RAP packing of pentagons of pentagons generated using `ARBITRARYPACKER`. (Top left) 100 pentagons packed. (Top right) 200 pentagons packed. (Bottom left) 500 pentagons packed. (Bottom right) 1000 pentagons packed.

Chapter 3 when we consider the random packing behaviour of ellipses and further details of the implementation of the packing algorithm are given in Section 3.2.

ARBITRARYPACKER also implements both the RAP and our new RRAP model allowing us to study the role of shape in sequential packing models. Figure 1.5 shows random packings of pentagons generated using ARBITRARYPACKER and the RAP model. Full details of the implementation of the RAP and RRAP model are given in Chapter 4.

ARBITRARYPACKER is again used in our packing-driven shape evolution of grains model in Chapter 5. Here we take advantage of the ability of the program to pack objects of any desired shape and to even vary the shape of the objects as the simulation proceeds. Full details of the model are given in Chapter 5.

Finally a 3D extension to ARBITRARYPACKER that can consider sphere packings is utilised in Chapter 7. Here both a monte-carlo packing algorithm is implemented and a fully dynamic 3D model similar to that used in Chapter 2 where we consider Newton's Cradle. Full details of the 3D implementation are given in Chapter 7.

1.9 Writing Style

In preparing a document such as this, one must decide on a writing style to use. I take the view that the passive voice is less pleasant to read and understand, thus a choice between the use of "I" or "We" is necessary. I have chosen to use we to refer to work presented in this thesis with consideration of the fact that research is so often a collaborative effort, with contributions made to this work from supervisors, group members, project students, collaborators and many many helpful discussions with fellow scientists. Except where I have explicitly acknowledged the computational implementations of others, I have been the developer of the software used in the generation of the computational results presented in this thesis, in particular

the `ARBITRARYPACKER` software used in Chapters 3, 4, 5 and 7 and the modifications to `Surface Evolver` used in Chapter 6. The numerical results in Chapter 2, I obtained by modifying a 2D code written by Finn MacLeod [53] and the implementation of the viscous froth model in `Surface Evolver` that I utilise in Chapter 8 was implemented by Simon Cox [58].

And now let us begin by considering the surprising insights that we can gain into the behaviour of soft sphere systems by examining one of the simplest - Newton's Cradle.

Chapter 2

Newton's Cradle

2.1 Introduction

A line of touching spherical balls suspended from a rail by pairs of inelastic strings is often called a Newton's cradle (see Fig. 2.1). The spheres are arranged at rest in what is referred to as a sausage packing [8]. Interestingly, it is conjectured that for $N \leq 56$, such sausage packings offer the best arrangement which minimize the volume of the smallest convex figure containing all the spheres [108, 23].

Here we will consider Newton's cradle in the context of a 1-dimensional granular system. The forces that govern the interaction of the spheres are the same as those considered in the study of three-dimensional granular packings. However as we shall see even this simple 1-dimensional system displays complex dynamic behaviour and provides excellent insights into the nature of the forces involved in 3-dimensional granular packings.

In introductory physics textbooks, Newton's Cradle is generally introduced as an illustration of the conservation of momentum and energy [18, 89, 78, 72, 24, 109]. When one ball is displaced from the other four and released, it is claimed that the collisions will result in the ball at the opposite end of the line being ejected, with

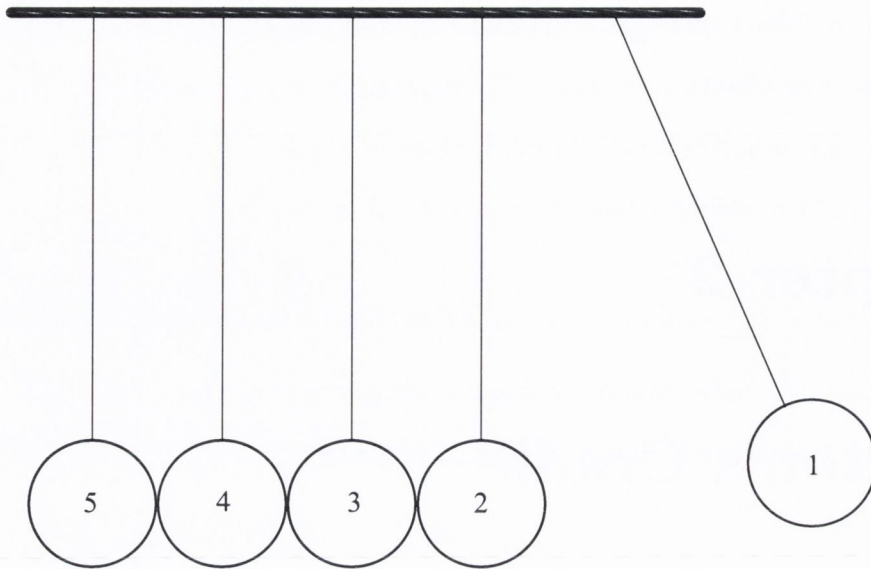


Figure 2.1: Newton's cradle. Ball 1 on the right is released and swings down to impact the line of stationary balls. It is generally suggested that only ball 5 on the left is ejected. However, both experiments and our simulations show that all balls will move after the impact.

all other balls remaining stationary. As the ejected ball swings back, it will collide with the line of balls. According to the common description, only the ball that was released initially will be ejected, while all other balls remain stationary.

However the actual experiment reveals a slightly different scenario. Careful observation shows that the first collision will break up the line of balls with the effect that all balls move. After further collisions all balls will eventually swing in phase, with an ever decreasing amplitude. The observed breakup of a line of balls after the impact of one ball was analyzed recently by Hinch and Saint-Jean.[52] We extend their work to consider the multiple collisions that follow thereafter. We believe that a closer examination of Newton's cradle can enhance and extend the pedagogical value of the original demonstration [49, 50, 86].

Newton's cradle has a long history. In 1662 papers on its underlying physics were presented to the Royal Society by no less than three eminent researchers,[24] John

Wallis (known for his presentation of π as an infinite product), Christopher Wren (mathematician, astronomer and architect of St. Paul's Cathedral in London), and Christiaan Huygens (author of a book on the wave theory of light and contributions to probability theory). Huygens pointed out that an explanation required both conservation of momentum and kinetic energy. (He did not use the kinetic energy but referred to a quantity proportional to mass and velocity squared.)

However, two equations are not sufficient to describe the behavior of Newton's cradle as was pointed out in Ref. [49]. A characterization of Newton's cradle consisting of N balls requires N velocities, but the conservation laws only give two equations. Herrmann and Schmäzle[49] analyzed Newton's cradle in terms of elastic forces between the contacting balls. They argued that a necessary condition for consistency with the simplified textbook description is that there be no dispersion in the relation between frequency and wavenumber for the vibrational motion of the chain of contacting balls. Their conclusion was based on their experiments with gliders on an air-track, where each glider was equipped with a spring bumper. These experiments effectively model the first set of collisions in Newton's cradle. When all gliders are in contact, the gliders may be represented as a linear chain, allowing for the calculation of eigenfrequencies and corresponding wave numbers. Only when the masses of the gliders and the spring constants were chosen to achieve a dispersion-free linear relation, did the gliders behave as in the textbook description.[49, 86]

In a follow-up paper Herrmann and Seitz[50] re-examined the actual cradle experiment and found in both the experiments and simulations that the first impact of a ball leads to a break-up of the line, contrary to the textbook description. In their simulations they modeled the interaction between balls as points of mass m that are connected by (Hertzian) springs. The force between two such masses is given by

$$F = k(y_n - y_{n-1})^\alpha, \quad (2.1)$$

where y_n is the displacement of ball n from its equilibrium position, k is a spring

constant, and the exponent $\alpha = 3/2$. The comparison of the propagation time of a perturbation through a line of balls obtained from both experiments and simulations using a range of different values of α showed that the assumption of Hertzian springs in Eq. (2.1) is valid. From their simulations of a five-ball cradle Herrmann and Seitz found that after the first collision, balls 1, 2, and 3 move backward, while balls 4 and 5 move forward with ball 4 carrying about 12% of the initial momentum of the incident ball. (We have labeled the balls in the direction from the incoming ball (ball 1) to the ball at the opposite end of the line (ball 5).) The momentum of ball 5 after the collision is nearly as large as that of ball 1 before the collision.

Without performing further simulations Herrmann and Seitz[50] concluded that when ejected ball 5 swings back, it would impact not on a compact line of balls (because the line has been broken up by the first impact), but rather there should be a sequence of independent collisions. However, in general there can be multiple collisions, involving more than two balls in contact during the collision as we will see in Sec. 2.2. This issue will be examined further in relation to our experimental results discussed in Sec. 2.6.

Hinch and Saint-Jean[52] conducted an exhaustive numerical and theoretical study of the fragmentation of a line of N balls by an impact. They find that some balls at the far end detach from the line and fly off, some in the middle hardly move, and the impacting ball rebounds backward bringing with it some of its nearby balls. They reproduced the numerical results of Ref. [50] for the first impact, and also set their results into a wider context. For a linear contact force law ($\alpha = 1$), the number of balls that are detached from the line is

$$N_{\text{detach}} = 1.5N^{1/3}, \quad (2.2)$$

while the majority of balls rebound. For the Hertzian force law ($\alpha = 3/2$) only a few balls rebound together with the impacting ball, with a velocity greater than 1% of the impact velocity. For example, for a line of $N = 5$ balls, two balls will leave

in the forward direction, for $N = 15$ this number increases to three. However, no power law analogous to Eq. (2.2) was established.

Despite the above studies and recent work in the engineering literature [21], there still is a need for further work on the nature of Newton's cradle for the following reasons. Because gravity was not included, the discussion was limited to the first impact. What happens in subsequent collisions? If we assume a dissipation-free system, will the motion settle down to a regular behavior or will it be chaotic? In what way will dissipation affect the motion? We will discuss these questions by presenting the results of theory, experiments, and simulations where gravity has explicitly been included, together with dissipative effects due to collisions and friction. Our work by no means exhausts the possible corrections that might be added to the model, but it seems sufficient for the available data.

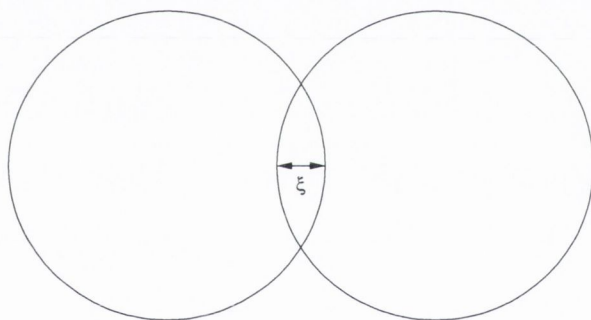


Figure 2.2: The overlap of two balls.

2.2 Modeling Newton's cradle

We define the overlap $\xi_{m,n}$ between two balls m and n as

$$\xi_{m,n} = (2R - r_{mn})_+, \quad (2.3)$$

where R is the radius of the balls and r_{mn} is the distance between their centers (see Fig. 2.2). The notation $()_+$ specifies that the value of the bracket is zero if the

expression inside is negative, as required for the representation of contact forces that cannot be in tension. If we model the contact forces as described in Sec. I, the force on ball n may be written as

$$m\ddot{x}_n = k[\xi_{n-1,n}^\alpha - \xi_{n,n+1}^\alpha], \quad (2.4)$$

where x_n denotes the position of ball n .

The introduction of gravity requires some discussion. Although Eq. (2.4) holds for a one-dimensional line of balls where the impact is in the same direction as the line, Newton's cradle is two-dimensional. The balls are attached to a frame by an inelastic string of length L and can swing about their respective equilibrium positions $(x_{o,n}, L)$ along arcs of circles. This motion causes the collisions to become off-centered if the balls are a finite distance away from their equilibrium positions. Our model neglects this effect. It is restricted to small angles or amplitudes $|x_n - x_{o,n}| \ll L$, in order to maintain a one-dimensional description of the cradle.

In the same approximation, gravity can be modeled as a simple restoring force, that is, a harmonic spring which acts to move each ball back to its equilibrium positions $x_{o,n}$. The gravitational spring constant is given by $k_g = mg/L$.

The equations of motion for the dissipation-free Newton's cradle are thus:

$$m\ddot{x}_n = k\xi_{n-1,n}^\alpha - k\xi_{n,n+1}^\alpha + k_g(x_{o,n} - x_n), \quad (2.5)$$

where n ranges from 1 to N . Modeling contacting spheres requires $\alpha = 3/2$ (Hertz law).[63] The spring constant k may be written in terms of material constants as

$$k = \sqrt{2RE}/[3(1 - \nu^2)], \quad (2.6)$$

where E is Young's modulus, ν is Poisson's ratio, and R is the radius of the balls [52]. We solved Eq. (2.5) for $N = 5$ using the second-order velocity Verlet algorithm[45] and the initial conditions for $x_n(t = 0)$: $x_1(0) = A$, $x_n(0) = x_{o,n}$ for $2 \leq n \leq 5$, and $\dot{x}_n(0) = 0$ for all n , corresponding to one ball being released with an amplitude A on to a stationary line of balls (see Fig. 2.1).

The velocity Verlet algorithm determines the positions, velocities and accelerations at time $t + \Delta t$ for each of the n balls in the following way:

$$x_n(t + \Delta t) = x_n(t) + \dot{x}_n(t)\Delta t + \frac{1}{2}\ddot{x}_n\Delta t^2 \quad (2.7)$$

$$\dot{x}_n(t + \frac{\Delta t}{2}) = \dot{x}_n(t) + \frac{1}{2}\ddot{x}_n(t)\Delta t \quad (2.8)$$

$$\ddot{x}_n(t + \Delta t) = -(\frac{1}{m})F_n(x_n(t + \Delta t)) \quad (2.9)$$

$$\dot{x}_n(t + \Delta t) = \dot{x}_n(t + \frac{\Delta t}{2}) + \frac{1}{2}\ddot{x}_n(t + \Delta t)\Delta t \quad (2.10)$$

where F_n is the total force on ball n .

It is common to introduce dimensionless variables before solving the equations of motion numerically. However, in our problem there are two time and length scales. Although the swinging balls may best be described in terms of their period $T_0 = 2\pi\sqrt{L/g}$ and string length L , individual collisions occur on a much shorter time scale $t_0 = (m^2/k^2v)^{1/5}$ and displacement scale $l_0 = (m^2v^4/k^2)^{1/5}$. Here v is the velocity of the impacting ball, given by $v = A\sqrt{g/L}$.

Because Eq. (2.5) describes a conservative system, the appropriate time step Δt for the numerical integration may be found by checking for energy conservation. Our chosen time step of approximately $2.5 \times 10^{-3} t_0$ lead to a relative error in the energy of not more than 0.005% over a time of over 10000 T_0 .

An initial test of our code was undertaken by setting $k_g = 0$ to model the impact on a line of balls in the absence of gravity. This simulation reproduced the results of Ref. [52] for the final velocities of all balls after the impact.

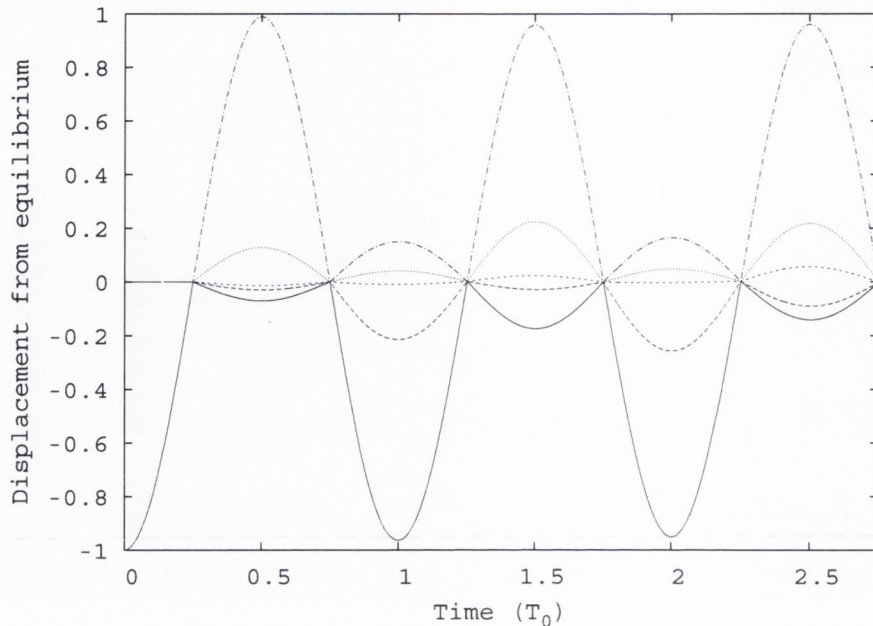


Figure 2.3: Displacement from their respective equilibrium positions of each of the five balls as a function of time. Note that the first impact results in a fragmentation of the line of balls. Contrary to textbook explanations of Newton's cradle, all balls are subsequently in motion. In the early stages of this dissipation-free simulation, the largest amplitudes of motion are exhibited by balls 1 and 5. (The displacement is plotted as a fraction of the initial amplitude of the incident ball. Time is displayed in multiples of the period of a single ball $T_0 = \sqrt{\frac{L}{g}}$.)

2.3 Results

For $k_g > 0$ we found that the first collision breaks up the line of balls. As the balls move back toward their respective equilibrium positions, however, they do not return to their individual stationary starting positions. This difference leads to a different scenario for the second set of collisions. As time evolves, an oscillatory motion becomes established, as we will demonstrate in Sec. 2.4 for the case of $N = 2$.

Figure 2.3 shows the displacements of the balls for $N = 5$ where ball 1 has been released from an amplitude $A = 0.27L$ onto a line of four balls. The collision (at

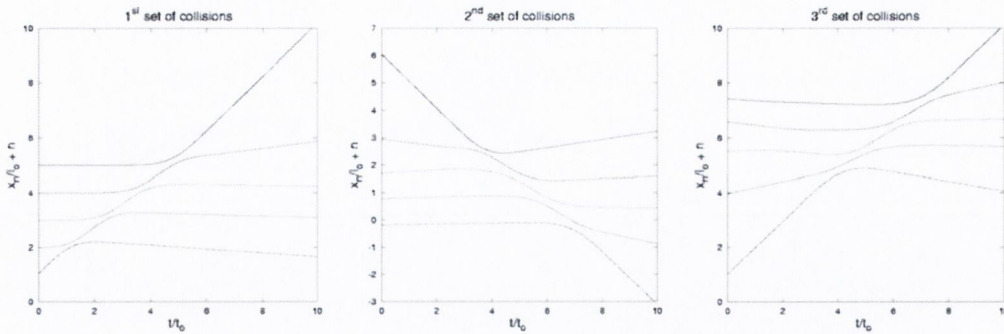


Figure 2.4: A detailed view of the first three sets of collisions reveals the symmetry breaking that occurs due to the break-up of the line in the first collision. Time is displayed in multiples of $(m^2/k^2v)^{1/5}$. We have chosen the time origin as the moment when the incident ball passes through its equilibrium position. The displacements are made dimensionless by dividing by the length scale l_0 . For visual clarity they are shifted by n , where the balls are labeled from 1 to 5 as in Fig. 2.1.

time $\pi/2\sqrt{\frac{L}{g}}$) results in the break-up of the line with balls 4 and 5 moving forward and balls 1, 2, and 3 rebounding. Ball 5 reaches its maximum displacement at time $\pi\sqrt{\frac{L}{g}}$. As it swings back, it will no longer hit a stationary line at time $3\pi/2\sqrt{L/g}$. The second set of collisions, shown in Fig. 2.4(b) is thus not anti-symmetric to the first set (see Fig. 2.4(a)). Figure 2.4(c) displays the third set of collisions, which is clearly different from the first set.

Due to the fragmentation of the line of balls at the initial collision, there are no obvious symmetry considerations that can explain the configurations in the latter collisions. The question arises whether the system of five balls will develop any periodicity in its long-term behavior or will be chaotic. Our data for a time of more than $10000T_0$ is best displayed by showing phase portraits at various times (see Fig. 2.5). Generally there is one ball colliding with a line of four slightly separated balls. However, the amplitudes of the first ball and the line of balls display very low

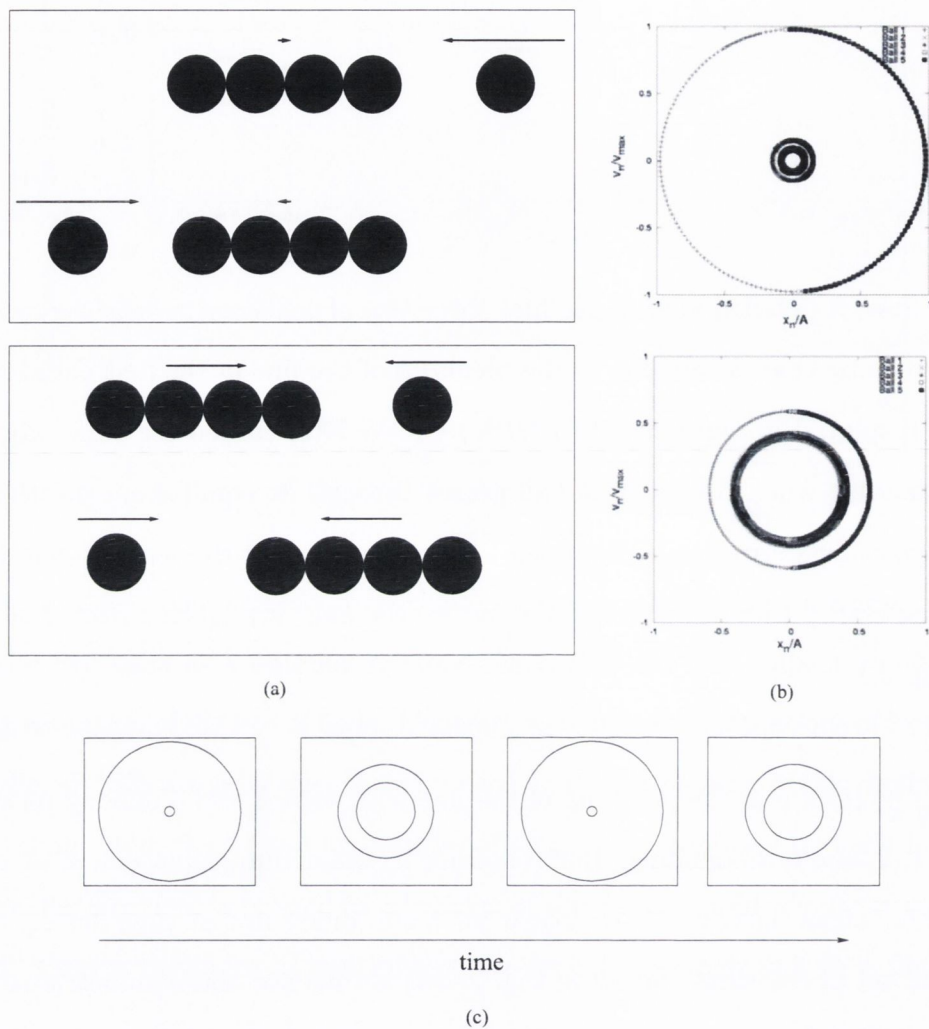


Figure 2.5: (a) The long-time behavior of the dissipation-free $N = 5$ cradle is characterized by a slow oscillation between two modes of motion. Both modes involve the collision of one ball against a group of four. In mode II all balls move with a similar speed, in mode I the cluster moves much slower than the single ball. (b) Simulation results in the form of phase-portraits. (c) A sketch of the evolution of these portraits.

frequency oscillations between two modes of motion. In mode I the cluster of four balls moves much slower than the single ball while in mode II all balls move with a similar speed. This behavior is particularly pronounced for $N = 2$, but also is well pronounced for $N = 4$ and $N = 5$ as shown in Fig. 2.5.

2.4 Theory of a two-ball cradle

We now present an analytical treatment of the relatively simple two-ball cradle, which leads to the identification of the behavior with the phenomenon of beats. We will show that the softness of the balls leads to an oscillation of the collision points. This variation of the phase portrait in time is also seen in our simulations of the three and four ball cradles.

Even if the balls are not infinitely hard, the standard textbook description is still valid in the sense that the impacting ball comes to a complete standstill while the impacted ball moves off with the same velocity as the impacting ball. However, what is generally ignored is the fact that the impact does not take place instantaneously. During this finite interaction time, both balls have a nonzero velocity and their point of contact will move a certain distance along the direction of the impact. (For a discussion of the related case of a bullet shot into a hanging block, see Ref. [37].) The impacted ball will move away from its equilibrium position by a distance Δx and will consequently swing back after the collision. From our simulations we find that Δx scales as $\Delta x \propto m^{5/2} v^{5/4} k^{-2/5}$, consistent with the displacement scale introduced in Ref. [52].

The subsequent behavior, sketched in Section 2.3, can be analyzed as follows. If we denote the positions of each ball relative to their respective equilibrium position by x_1 and x_2 , the center of mass X_c is given by

$$X_c = \frac{(x_1 + x_2)}{2}, \quad (2.11)$$

while the relative position X_r is

$$X_r = x_1 - x_2. \quad (2.12)$$

For simplicity we shall assume a harmonic force law (with spring constant K_r), where the subscript r signifies that the interaction is due to the relative positions of the balls. The validity of the argument will however not be restricted to this force law. The cradle will be seen to be equivalent to a pair of coupled oscillators that are coupled only when the two balls are in contact ($X_r > 0$).

Each ball is subject to gravitation, modeled as a spring with spring constant $K_c = mg/L$, as in Sec. 2.2. (Previously this constant was called k_g , but we shall use K_c in the following discussion to remind us that the spring acts on the center of gravity of the two balls.) The potential energy of each ball is given by $\frac{1}{2}K_c X_c^2$. The potential energy of contact is given by $\frac{1}{2}K_r X_r^2$ for $X_r > 0$ and is zero for $X_r \leq 0$. The natural frequencies associated with the two spring constants for mass m are given by $\Omega^2 = K_c/m$ and $\omega^2 = K_r/m$.

We consider the case where ball 1 is released from $x_1 = -A$ and $x_2 = 0$. Then initially we have

$$X_c = \frac{x_1 + x_2}{2} = -A \quad (2.13a)$$

$$X_r = -A. \quad (2.13b)$$

The center of mass motion is that of a mass $2m$ acted on by external forces ($F = -K_c x_c$) only. Hence, the motion is simple harmonic with frequency Ω :

$$X_c = -\frac{A}{2} \cos \Omega t. \quad (2.14)$$

The dependence of the relative position X_r on the time as obtained from our simulation is shown in Fig. 2.6.

The cradle features two time scales, the collision time, τ_0 and the time between collisions, $\Gamma_0 \gg \tau_0$, given by

$$2\Gamma_0 = \frac{2\pi}{\Omega}, \quad (2.15)$$

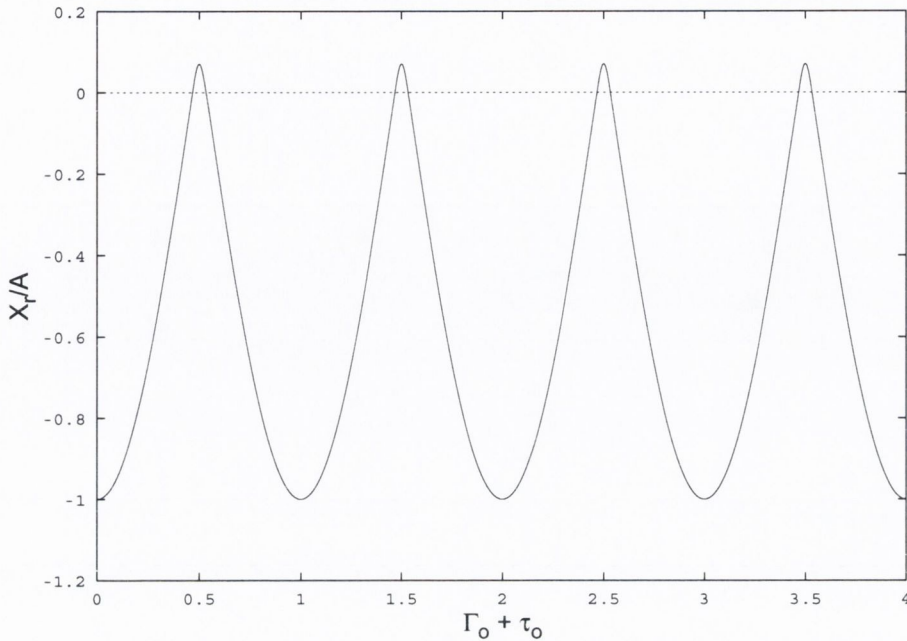


Figure 2.6: Plot of the relative position X_r for the $N = 2$ cradle as a function of time plotted in multiples of $\Gamma_0 + \tau_0$ (time between collisions + interaction time). The simulation was performed with a small ratio $K_r/K_c = 100$ to increase the collision time τ_0 .

corresponding to free motion under the action of K_c with $X_r \leq 0$.

We make the approximation that during a collision ($X_r > 0$), where the repulsive force due to K_r dominates, we neglect K_c . Then the motion is another (short) half cycle under K_r , as is seen in Fig. 2.6. We find for the interaction time τ_0

$$2\tau_0 = \frac{2\pi}{\sqrt{2}\omega} = \frac{\sqrt{2}\pi}{\omega}. \quad (2.16)$$

Note that $\sqrt{2}\omega$ is the frequency of a single ball with a doubled spring constant.

To represent the resulting motion of the balls, it is helpful to switch identities after every collision, so that ball 1 \leftrightarrow ball 2 and thus $X_r \leftrightarrow -X_r$. We may then approximate X_r by

$$X_r = -A \cos \frac{\pi t}{\Gamma_0 + \tau_0}. \quad (2.17)$$

If we combine Eq. (2.17) with Eq. (2.11) for X_c , we find “beats” for the motion of

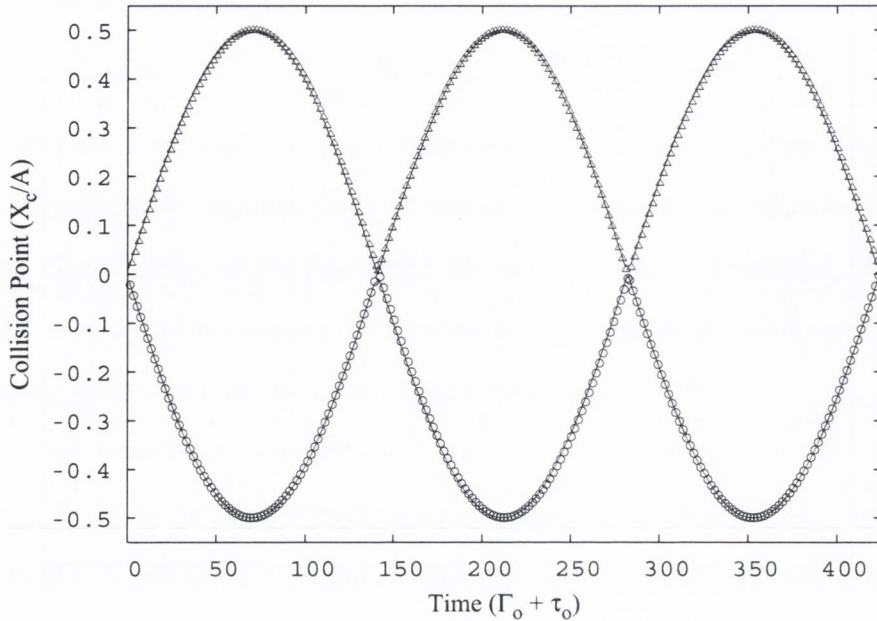


Figure 2.7: For $N = 2$ successive collisions take place in turn on the left (circles) and on the right (triangles) of the center of the system. The numerically determined points are well described by theory (continuous line), Eq. (2.20).

one ball (with the above role reversal implied). For $\tau_0 \ll \Gamma_0$, we obtain

$$\begin{aligned} \hat{x} &= -\frac{A}{2} \cos \frac{\pi t}{\Gamma_0} - \frac{A}{2} \cos \frac{\pi t}{\Gamma_0 + \tau_0} \\ &\approx -A \cos \frac{\pi t}{\Gamma_0} \cos \frac{\pi \tau_0}{2\Gamma_0^2} t, \end{aligned} \quad (2.18)$$

where \hat{x} denotes that the identity switches between x_1 and x_2 after each collision. Thus we have high-frequency oscillations with a frequency Ω which are modulated by the low frequency $\pi\tau_0/2\Gamma_0^2 = \Omega^2/2\sqrt{2}\omega$.

We also can calculate the positions of the collisions. When they occur, we have $X_r = 0$ and the position of the collision is X_c . From Eq. (2.17) we obtain

$$\frac{\pi t_i}{\Gamma_0 + \tau_0} = \pi i + \frac{\pi}{2}, \quad (2.19)$$

where t_i is the time of the i th collision. Hence the corresponding position is given

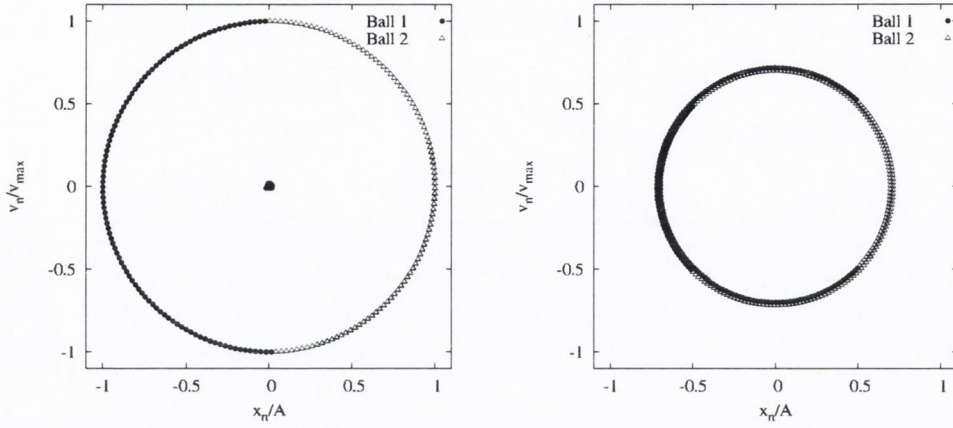


Figure 2.8: Two phase portraits that characterize the motion of the $N = 2$ cradle. The system slowly oscillates between the case where both balls move with the same speed and the case where one ball collides with a stationary ball. The axes are made dimensionless by dividing the velocity of each ball by the maximum velocity of the incoming ball and the position by the initial amplitude.

by

$$\begin{aligned}
 x_i &= X_c = -\frac{A}{2} \cos\left(\frac{\pi}{\Gamma_0}\left(i + \frac{1}{2}\right)(\Gamma_0 + \tau_0)\right) \\
 &\approx \frac{A}{2}(-1)^i \sin\frac{\pi\tau_0}{\Gamma_0^2}t,
 \end{aligned} \tag{2.20}$$

where we have used the definition of X_c in Eq. (2.11) and the approximation $\Gamma \gg \tau_0$. Figure 2.7 shows the excellent agreement between the analytical expression in Eq. (2.20) and our simulation.

The oscillation of the collision points for $N = 2$ is caused by the finite elastic response of the balls. Plotting phase portraits at different times, as shown in Fig. 2.8, reveals the same characteristics we had obtained for the $N = 5$.

2.5 The effects of dissipation

Although the study of a dissipation-free version of Newton's cradle is interesting in its own right, any realistic simulation of the experiment needs to include dissipation. Two obvious such mechanisms are the velocity-dependent viscous drag of air and the viscoelastic dissipation associated with the collisions of the balls. We chose a simple linear dependence on the velocity $F_{\text{fr}} = \eta v$ (Stokes law).

The inelastic character of the collisions is modeled by including a viscoelastic dissipation force of the form [110]

$$F_{\text{diss}} = -\gamma \frac{d}{dt}(\xi^\beta), \quad (2.21)$$

into the equation of motion. Here ξ is the overlap between two balls as defined in Eq. (2.3) and $\beta = 3/2$ (Hertz-Kuwabara-Kono model).[110]

The equation of motion for the dissipative Newton's cradle is then given by

$$m\ddot{x}_n = k\xi_{n-1,n}^\alpha - k\xi_{n,n+1}^\alpha + k_g(x_{o,n} - x_n) - \eta v - \gamma \frac{d}{dt}(\xi^\beta). \quad (2.22)$$

The Stokes term continually removes energy from the system, while viscoelastic dissipation occurs only during collisions. Due to the velocity dependent forces in the system we utilize the Euler-Richardson method to solve our new equation of motion (Eq.2.22) [102]. The Euler Richardson method determines the positions, velocities and accelerations at time $t + \Delta t$ for each of the n balls in the following way:

$$\dot{x}_n^{\text{mid}} = \dot{x}_n(t) + \frac{1}{2}\ddot{x}_n(t)\Delta t \quad (2.23)$$

$$x_n^{\text{mid}} = x_n(t) + \frac{1}{2}\dot{x}_n(t)\Delta t \quad (2.24)$$

$$\ddot{x}_n^{\text{mid}} = F_n(x_n^{\text{mid}}, \dot{x}_n^{\text{mid}}, t + \frac{1}{2}\Delta t) \quad (2.25)$$

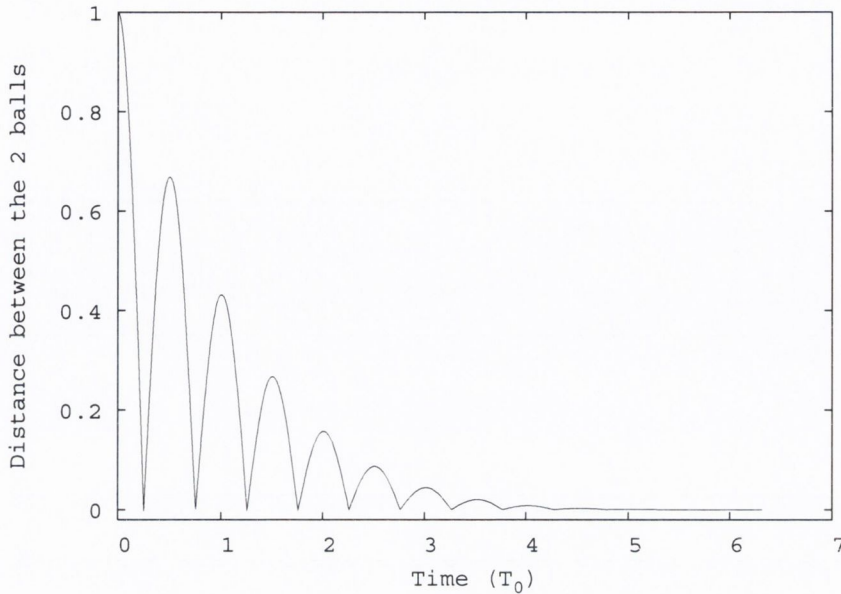


Figure 2.9: Due to energy dissipation during the collisions, the distance between the centers of the balls decreases in time and the balls will swing in phase. The data is for $N = 2$.

$$\dot{x}_n(t + \Delta t) = \dot{x}(t) + \ddot{x}^{\text{mid}} \Delta t \quad (2.26)$$

$$x_n(t + \Delta t) = x(t) + \dot{x}^{\text{mid}} \Delta t \quad (2.27)$$

where x_n^{mid} , \dot{x}_n^{mid} and \ddot{x}_n^{mid} are the position, velocity and acceleration of the ball n at the half way point of the time step Δt .

We use the same time step as for our dissipation free simulations. The time step was tested using the Euler-Richardson method for the dissipation-free case and seen again to give excellent energy conservation.

To demonstrate the effect of the viscoelastic dissipation on the behavior of the system, simulations were run where the Stokes term was neglected ($\eta = 0$). In Fig. 2.9 we plot the distance between the two balls as a function of time. This simulation demonstrates that the final collective motion of the balls that is reached

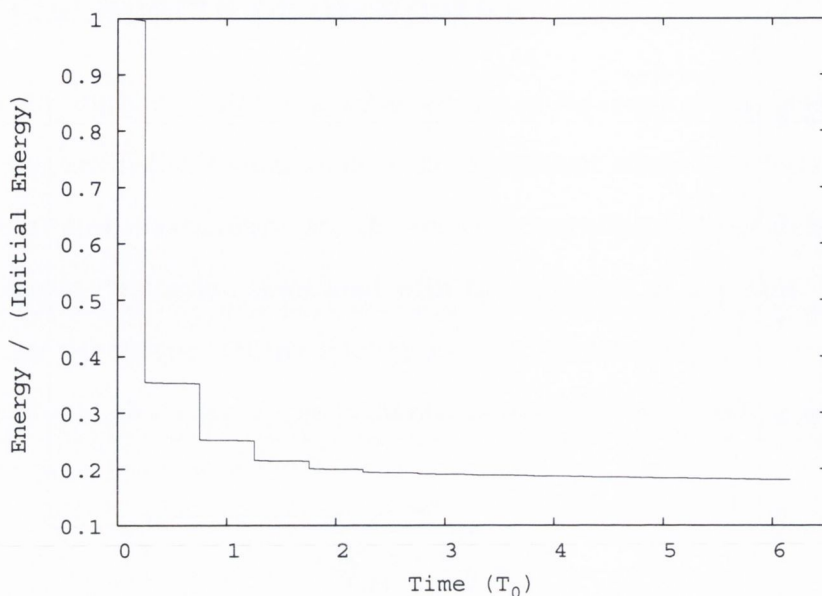


Figure 2.10: Loss of energy due to the Stokes damping and viscoelastic dissipation for the $N = 5$ cradle. The y -axis is made dimensionless by dividing by the initial energy of the system.

experimentally is caused by the energy dissipation due to the collisions. The final amplitude of swing can be predicted in the following way.

Consider an N -ball cradle with initially only one ball moving with velocity v_0 . The total initial kinetic energy $S_0 = \frac{1}{2}mv_0^2$ may be written as the sum of the kinetic energy due to the motion of the center of mass S_c plus the kinetic energy relative to the center of mass, S_r ,

$$S_0 = S_c + S_r, \quad (2.28)$$

with $S_c = \frac{1}{2}Nm(\frac{1}{N}\sum_{i=1}^N v_i)^2$. Because all velocities are zero apart from $v_1 = v_0$, S_c reduces to $S_c = \frac{S_0}{N}$. From Eq. (2.28) we immediately obtain

$$S_r = \frac{N-1}{N}S_0. \quad (2.29)$$

Because all this relative kinetic energy will be dissipated in subsequent collisions,

the final energy of the system is given by

$$S_{\text{final}} = S_0 - S_r = \frac{S_0}{N}. \quad (2.30)$$

The final energy of each ball, neglecting the Stokes term, is simply given by E_{initial}/N^2 . Note that this value is independent of the coefficient of dissipation, which specifies only the time it takes for the relative kinetic energy to be fully dissipated and thus the time it takes for all balls to swing in phase.

For a finite value of η , the Stokes damping constantly removes energy from the system, causing the amplitude of all the balls to diminish eventually to zero. In Fig. 2.10 we show the variation of the total energy with time for a five-ball cradle where both Stokes damping and viscoelastic dissipation is included in the simulation. Here we see that the energy decays quickly to approximately 1/5 of the initial energy, where the collective motion state is reached. It then continues to decay due to the Stokes damping.

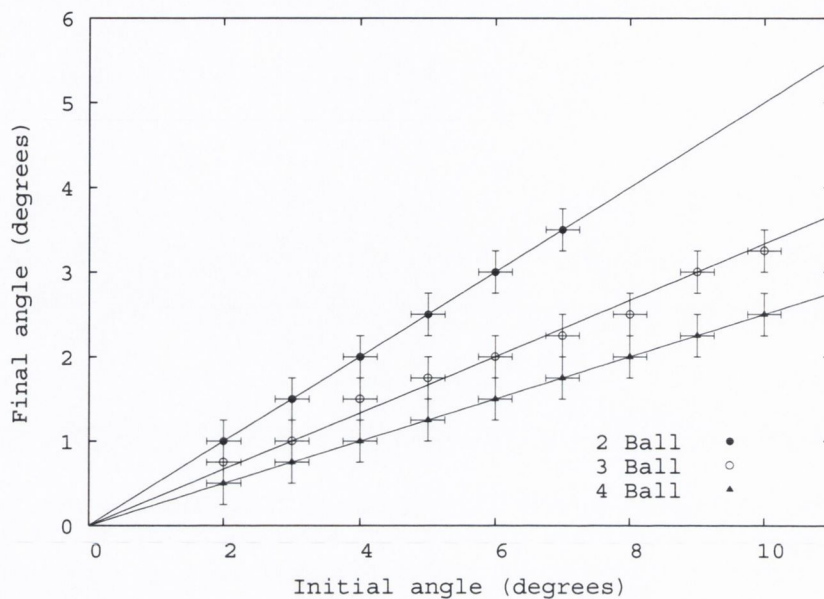


Figure 2.11: Experimental data for Newton's cradle with $N = 2, 3,$ and 4 balls. A single ball is released from an angle θ_0 . After many collisions, the balls settle into a collective mode of motion where all move together with amplitude θ_c . The data is well described by $\theta_c = \theta_0/N$ (solid line). We take the error in the final angle of swing to be the accuracy of the protractors used, $\pm 0.25^\circ$.

2.6 Experiments

To examine the validity of our simulations, we have carried out experiments using a specially constructed large Newton's cradle consisting of four metal balls (diameter 6.8 cm, mass 0.7 kg) suspended from 1.3 m long wires. (The balls we used were commercial sand-filled metal boules.) Specially constructed large protractors were used for accurate measurements of the angle of swing to an accuracy of $\pm 0.25^\circ$.

Our first set of experiments investigated our prediction for the amplitude of the collective motion of the balls described in Sec. 2.5. A single ball was released from an angle θ_0 onto a line of N balls. Once the state of collective motion was reached, we determined its amplitude θ_c . The time required for the system of balls to settle into the collective mode is between one and two minutes. This time compares with

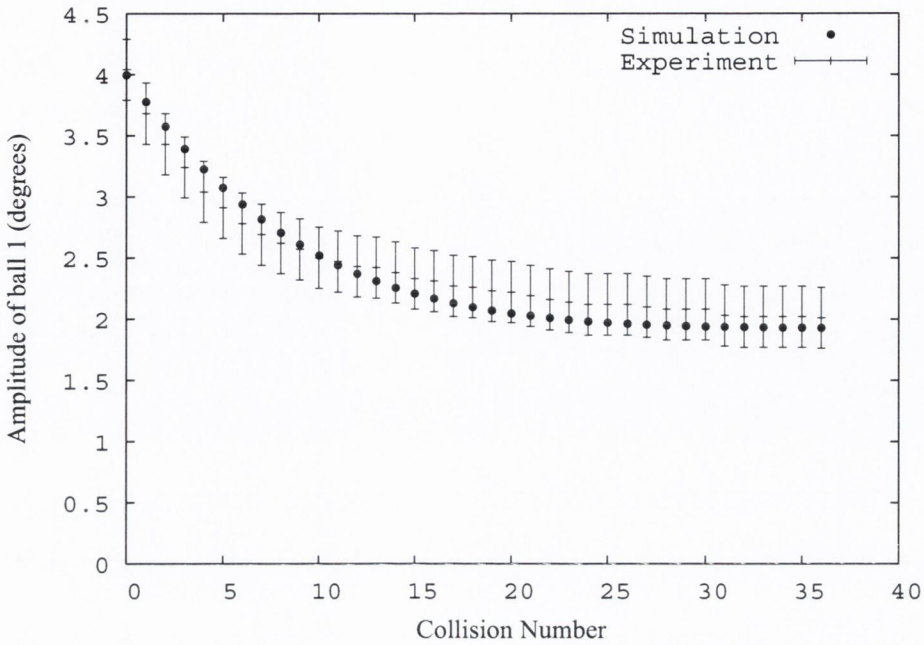


Figure 2.12: Variation of the amplitude of ball 1 in a $N = 2$ cradle with time. Shown are experimental data and results from our simulations. (The experimental data in Figs. 12–15 are averaged over 10 runs of the experiment, and the error in the amplitude is taken to be the accuracy of the angle measurement $\pm 0.25^\circ$.)

the time of about one hour for the system to come to rest.

Figure 2.11 shows measurements of θ_c as a function of θ_0 for $N = 2, 3,$ and 4 . The data is well described by $\theta_c = \theta_0/N$, consistent with Eq. (2.30) and our conclusion that the collisions will only remove energy of the relative motion of the balls.

Our second set of experiments focused on energy dissipation due to the collisions of the balls. Again a single ball was released from an angle θ_0 and collided with a line of 2, 3, or 4 balls. We determined its amplitude after every collision with its neighboring ball. The experimental data, shown in Figs. 2.12–2.14, reveals that the textbook explanation of Newton’s Cradle with its prediction of a constant amplitude fails.

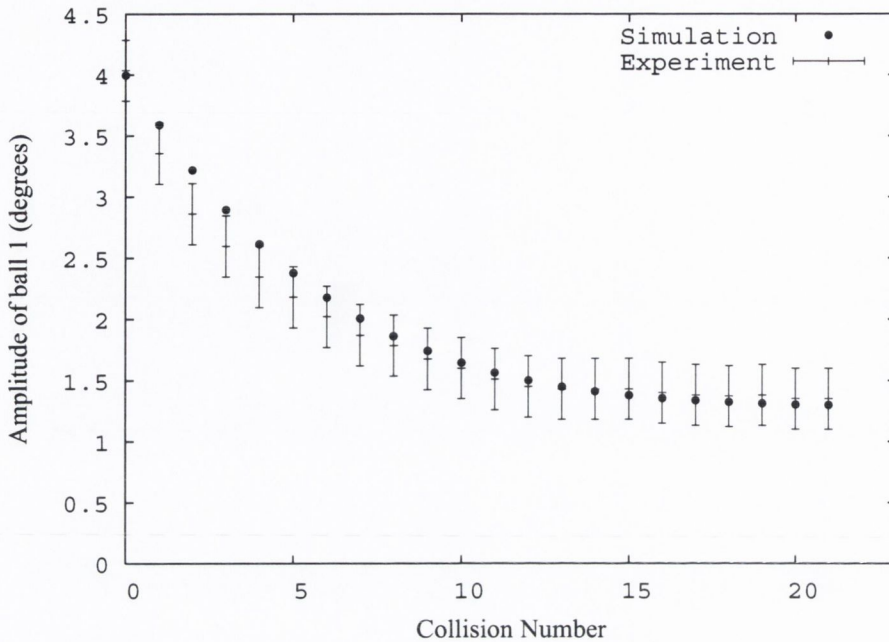


Figure 2.13: Variation in amplitude of ball 1 for the $N = 3$ cradle. The simulation used the same set of parameters as for the two-ball case.

To determine a value for the damping constant η , the time-dependence of the amplitude was determined for a single ball and fitted to $\theta_{\max}(t) = \theta_0 \exp(-\eta t/2m)$ to give $\eta = 6.8 \pm 0.136 \times 10^{-4} \text{ kg s}^{-1}$. The constant k was calculated from Eq. (2.6) with $E = 2 \times 10^{11} \text{ Pa}$ and $\nu = 0.33$ for steel and was found to be $k = 1.38 \times 10^{10} \text{ kg m}^{-1/2} \text{ s}^{-2}$.

The viscoelastic dissipation parameter γ was then estimated by adjusting it in the simulation to match the dissipation seen in the 2 ball experiment. The value was found to be $\gamma = 1.47 \times 10^2 \text{ kg s}^{-1} \text{ m}^{-2}$. This value was then used in the three and four ball simulations shown in Figs. 2.13 and 2.14.

We find from our simulations that the exact separation of the balls when a collision occurs has a very important influence on the behavior of the system. If balls 2–5 are initially in their exact equilibrium positions when they touch, the subsequent collisions will essentially be multi-ball collisions. In such collisions the energy

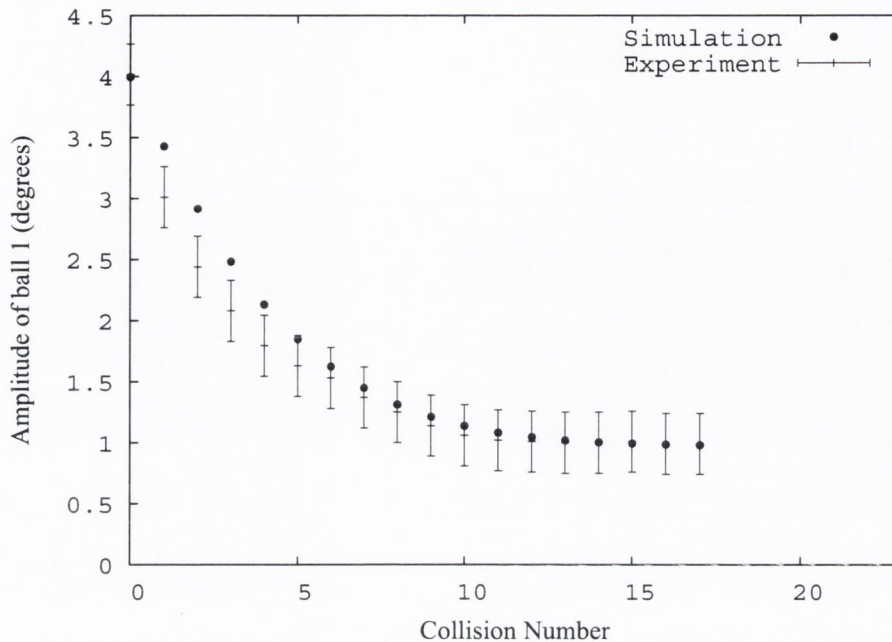


Figure 2.14: Variation in amplitude of ball 1 for the $N = 4$ cradle. The simulation used the same set of parameters as for the two-ball case.

dissipated is less than in a series of two-ball collisions. However, any experimental set-up has imperfections that will cause the system to deviate from this idealization, for example, small differences in the oscillation periods of the individual balls or the balls not hanging exactly at their equilibrium position.

To incorporate these imperfections into the simulation, we varied the value of k_g for each of the balls so that the periods of the balls vary slightly, and thus all collisions after the initial one are no longer multiball-collisions. In Figs. 2.12–2.14, the periods of the balls vary by $\Delta T = 0.01$ s or $1/240$ th of a period. (This variation has no noticeable effect in the two ball case because all collisions are two ball collisions.) When this effect is incorporated, we find good agreement between the simulations and the experimental data.

We have tested the effect of a range of differences in the periods of the balls. We found that there is little variation in the amplitudes obtained until we choose

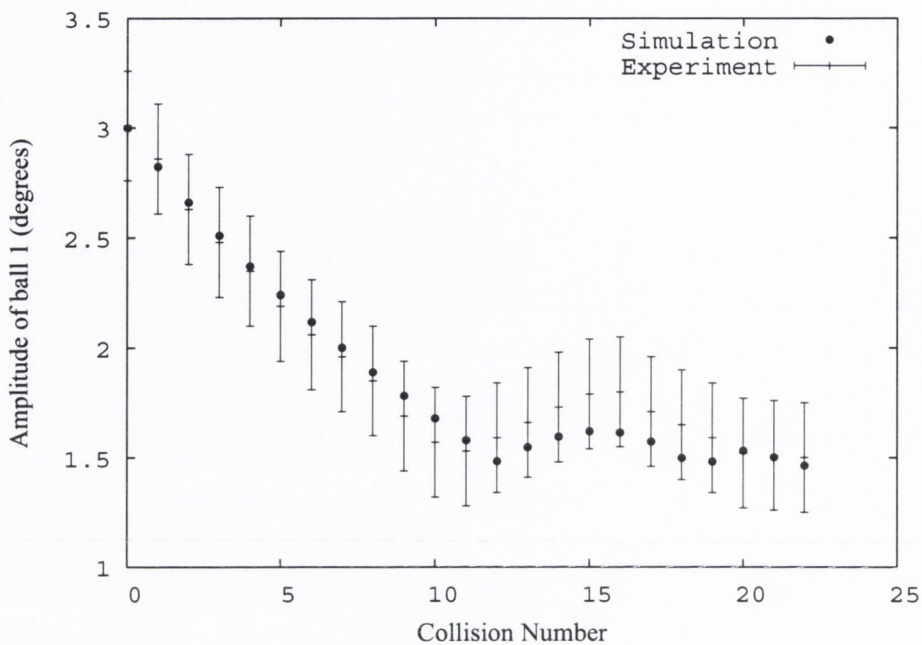


Figure 2.15: Variation in amplitude of ball 1 for a $N = 2$ cradle with a 1 mm gap between the rest positions of the balls. The simulation uses the same set of parameters as for the two-ball case of Fig. 2.12.

either very small values of ΔT that approach the idealized case, or large values of ΔT that no longer represent an accurate description of the experiment. We tested removing the multiball collisions by introducing very small gaps, Δx , between the balls in the simulation. For small values of $\Delta x \approx 0.1$ mm, the amplitudes obtained in the simulations are almost identical to those obtained from the simulations that incorporate small variations in the period of the balls.

We also have considered the case where there is an appreciable gap between the balls. Figure 2.15 highlights the importance of a careful experimental setup, where instead of touching, there is a $\Delta x = 1$ mm gap between the balls when they are in their rest positions. Here we see a “beating” effect where the amplitude of ball 1 does not simply decay, but oscillates. This behavior is well replicated by our simulation.

2.7 Conclusion

We have shown that the physics involved in Newton's cradle is far from trivial and that the standard textbook explanation is only a first approximation. In the context of physics education our study of Newton's cradle might fulfill two purposes. Students should see that apparently simple experiments, when closely examined, can raise a number of complicated questions. One also should be cautious about fully accepting well-established explanations of physical phenomena without carefully scrutinizing the arguments.

In considering Newton's cradle in the context of a 1D granular system this work provides us with an excellent introduction to the nature of the interactions between soft spheres and the complexity that these systems can demonstrate even in the simplest 1D cases. We will further examine systems composed of interacting spheres when we apply the same techniques used here to the investigation of 3D sphere packings in Chapter 7.

Kinoshita *et. al* have recently considered an experimental system which they term a quantum Newton's cradle [59, 90]. They confine an atomic gas to an array of one-dimensional tubes by a web of laser beams. Interestingly they observe a behaviour that could be considered similar to our observations of the long term behaviour of the dissipation free Newton's cradle, finding that their system does not relax to equilibrium even after each atom has collided several thousand times. So it does indeed seem that Newton's cradle, often considered a simple desktop toy, can yield beneficial insights into the behaviour of a wide range of physical systems.

Chapter 3

Random Packing of Elliptical

Disks

3.1 Introduction

Simulations of packings of grains have generally considered the grains to be circular (2D) or spherical (3D) [81]. However if we consider most granular materials that we find in nature, they do not consist of exactly spherical particles. From grains of sand on sand on the beach to packings of large rocks, real world granular materials have a wide variety of shapes [56]. Here we will begin our investigation into the contribution shape makes in the packing of non-circular grains, by considering dense random packings of elliptical grains.

To understand the role that shape plays in the properties of granular packings, it is natural to deal first with particles of uniform size and a simple shape. Computer simulations for the random packing of spherocylinders (cylinders with caps of semi-spheres at both ends) were performed by Williams and Philipse [107]. They found that the packing fraction reaches a maximum of $\Phi \simeq 0.70$ for an aspect ratio $\alpha = 0.4$ of cylinder length to diameter, for larger values of α it decreases continually (it

is below the Bernal value for $\alpha > 1.5$). Another obvious non-spherical packing candidate is the ellipsoid. Hence Chaikin has recently chosen the confectionery known as M&M's[®] for packing experiments [91].

Our own study was motivated in part by the desire to better understand the remarkable results of Chaikin. These indicated a high packing density relative to sphere packings [33]. They find for a packing of ellipsoids of revolution with an aspect ratio of 1.93, appropriate to M&M's[®], a higher packing fraction than the random packing of spheres. Furthermore computer simulations of packings of ellipsoids with principal axes having three different values, lead to random packings with packing fractions close to that of fcc/hcp.

To explain this arguments of constraints and jamming have been adduced, which been a part of the general subject and which we outlined in Chapter 1. In brief, these associate the maximum density with the exhaustion of degrees of freedom by the constraints due to contacts, in a style of argument that goes back to Clerk Maxwell in the general context of static equilibrium of structures [71]. For ellipsoids there are effectively more degrees of freedom than those of spheres, so it is argued that compaction can continue further, establishing more contacts and a greater density.

3.2 Simulation of 2D packings of ellipses

In 2D there is a strong tendency for monodisperse systems to order (resulting in the hexagonal honeycomb packing for circular disks) [8], so it is necessary to deal with a polydisperse system, if we wish to gain insights into the role of disorder.

We utilise a monte-carlo type packing algorithm implemented in our software program `ARBITRARYPACKER`. As determining whether two disks are in contact or overlap is a simple task only for circles, to allow us to study the packing of arbitrarily shaped objects, we discretised the surface of the disks. Each disk is represented as

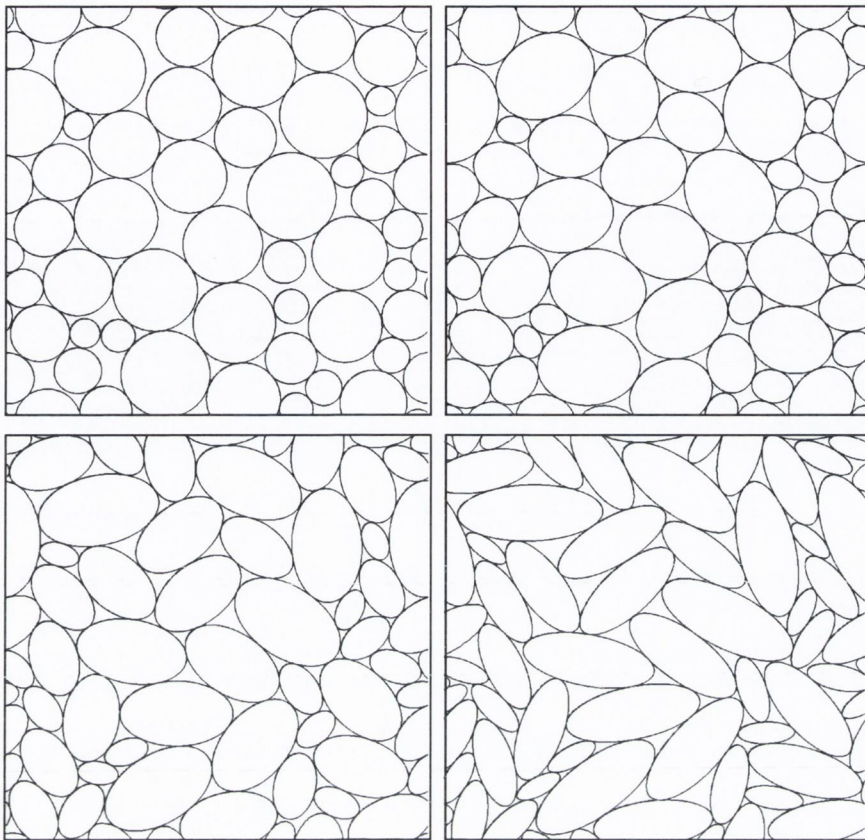


Figure 3.1: Computer simulations of dense packings of 50 ellipses with aspect ratio 1.0 (circles), 0.8, 0.6 and 0.4 respectively. The simulations use periodic boundary conditions.

a polygon with one hundred surface points (vertices) [74]. This gives us a highly accurate representation of an ellipse, introducing an error in packing fraction, Φ , of less than 0.001. (Calculated as the difference in Φ between the same packings of disks using 100 and 1000 surface points).

Our simulations are carried out using 50 disks of a given aspect ratio $\lambda = b/a$ (where a and b are respectively the semi-major and semi-minor axes). We use uniformly distributed random numbers to set the initial x and y coordinates of the disk centres (within a unit square) and the initial disk orientations (angle between semi-major axis and x -axis). The values of the semi-major axes a are taken from a

uniform distribution with a finite lower bound to avoid disks that are too small. The semi-minor axes are then given by $b = \lambda a$. There is no initial disk overlap. Periodic boundary conditions are employed in all simulations.

The compaction process consists of the following steps. First the area of each disk is increased such that the packing fraction is increased by $\Delta\Phi = 0.0001$. We then check for every disk if this has resulted in any overlap with its neighboring ellipses. If it has, it is moved in a random direction (and/or rotated by a random angle between $-\pi/2$ and $\pi/2$) that will reduce its total overlap with neighboring disks. (The overlap area between two disks is determined from the area of the overlap polygon using the CLIPPOLY polygon library [74]). If it already has zero overlap, then it attempts to make a random movement and rotation to another position that also represents zero overlap. This process is continued until all disks have zero overlap. Then the area of each disk is again increased such that the packing fraction is increased by $\Delta\Phi = 0.0001$.

The process of minimisation of the overlap to zero and increasing of the area of the disks is continued until it is no longer possible to obtain zero overlap. The packing fraction is then given by the ratio of the sum of all disk areas over the smallest box area at which the disks did not overlap.

Packings of ellipses of equal aspect ratios λ are produced as follows. We generate a densest packing of circles ($\lambda = 1$) using the above algorithm. For each subsequent packing, λ is reduced by 0.01, making the disks more elliptical while retaining the positions of the disk centres, and the orientation and length of their semi-major axes. The compaction of the disks then proceeds in the same way as before, resulting in a new dense packing of disks with the reduced aspect ratio. In this way, we generate packings of ellipses of equal aspect ratio λ , in the range from $\lambda = 1$ to $\lambda = 0.1$.

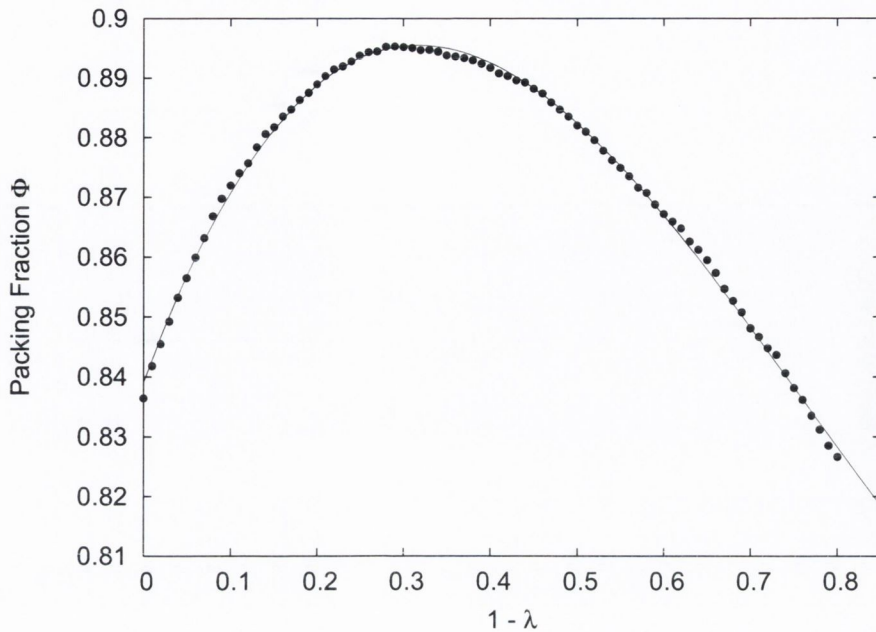


Figure 3.2: Variation of packing fraction Φ with $1 - \lambda$. Data shown is the average of 10 simulations of 50 disks for each aspect ratio. (The average standard deviation of the packing fractions obtained is 0.004.) The solid line is a fit to a third order polynomial with a maximum $\Phi = 0.895$ at $\lambda = 0.664$ and $\Phi(\lambda = 1) = 0.839$.

3.3 Results and Analysis

In 2D it is well established that polydisperse circular disks pack randomly with a density close to 0.84, for size distributions which involve substantial variations in size [8, 75]. This seems to apply quite widely, but cannot hold for extreme cases.

Figure 3.2 shows the variation of density Φ with aspect ratio, λ . In qualitative accord with Chaikin's observations [33] and the simulations of Williams and Philipse [107], we find that as one departs from a circular shape the packing fraction increases from an initial value of 0.837 to a maximum value of 0.895 for $\lambda \approx 0.7$. We see an initial linear increase in packing fraction as we increase the ellipticity and only see the packing fraction drop below that of the circular case for $\lambda < 0.25$. Our data is

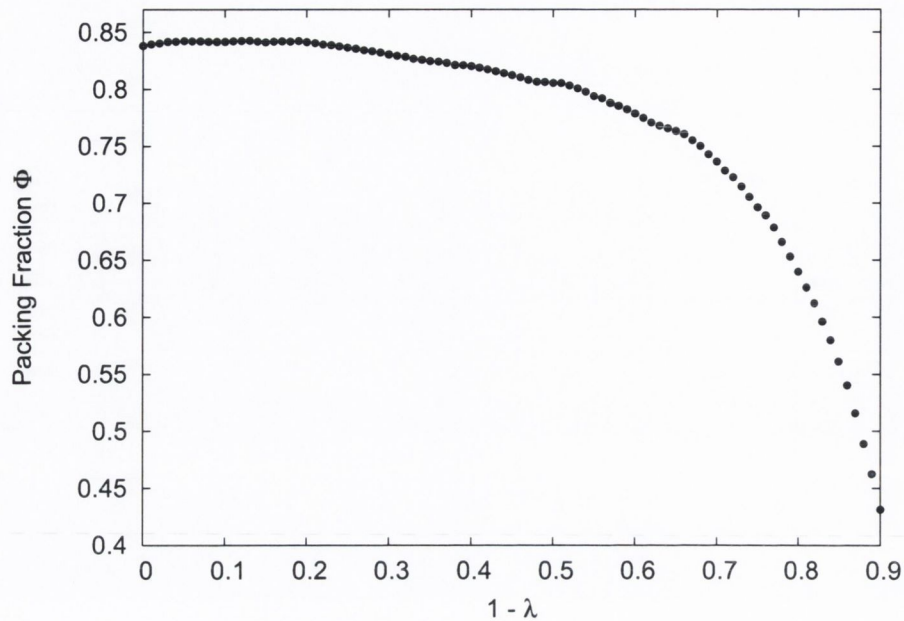


Figure 3.3: When we disallow disk rotations in our packing algorithm we find that the packing fraction Φ does not increase above the packing fraction of circular disks ($\Phi \approx 0.84$). There is a sharp decrease in packing fraction for aspect ratios less than 0.3. Data shown is the average of 10 simulations of 50 disks for each aspect ratio.

well represented by a third order polynomial as shown in Figure 3.2.

In considering these trends, we may first observe that for hard contacts there is always available to the system a structure with the same density ($\Phi \simeq 0.84$) as that of circular disks, since any degree of eccentricity may be introduced by a simple affine transformation, conserving area and the hard contacts. So in some sense both the initial linear increase and the eventual decrease of density are associated with the rotational disorder which is frozen in by the process used for compaction.

In order to shed some light on this, we have performed the following further calculation. As before, disks of a given value of λ were placed in a box with random initial locations and orientations. However, this time the disks were not allowed to rotate during the compaction process. Figure 3.3 shows that we no longer see the

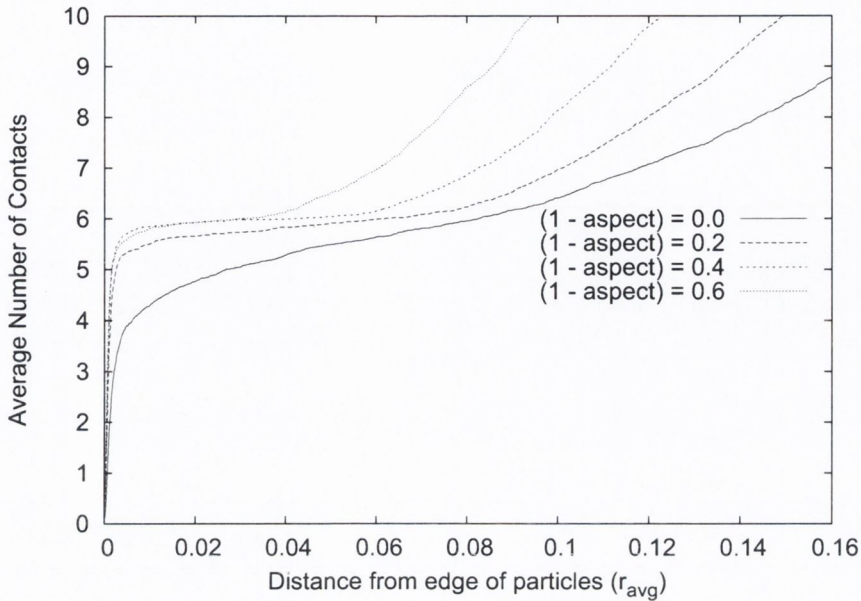


Figure 3.4: Variation of number of contacts, Z , with distance from edge of disks. We see a very clear plateau region at approximately 6 contacts for large aspect ratios.

large increase in packing fraction as we increase ellipticity away from that of a circle. Instead the packing fraction remains almost constant at $\Phi \approx 0.84$ up to $\lambda \approx 0.8$. We then observe a slow decrease in packing fraction for midrange values of λ . At high values of ellipticity there is a very large decrease in packing fraction, with a packing fraction as low as $\Phi \approx 0.43$ found for an aspect ratio of 0.1. These results show that as expected, the additional rotational degree of freedom in the case of ellipses is essential for an increase in the packing fraction above that of the circular case.

As discussed in Chapter 1, the standard arguments for the mean number of contacts (due to James Clerk Maxwell [71] and Charles Bennett [11]) have been based on the concept of “jamming”, that is, to constrain the system, two contacts per degree of freedom are required. Thus for a random packing of circles with two degrees of freedom (the two coordinates describing the position of the circle) one

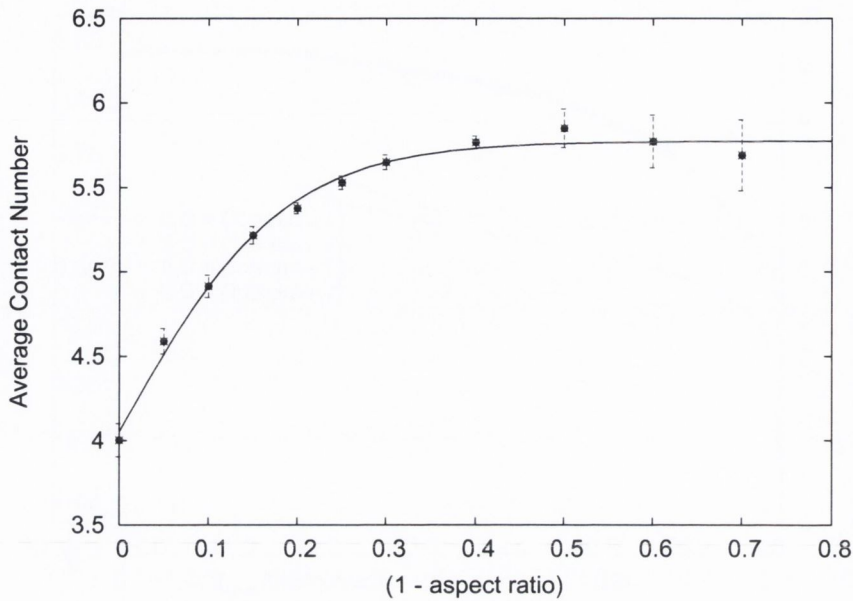


Figure 3.5: Variation of the average contact number with aspect ratio. The solid line is an empirical fit to $Z = a \tanh(b(1 - \lambda)) + c$, with $a = 1.72 \pm 0.06$, $b = 5.5 \pm 0.3$ and $c = 4.05 \pm 0.05$.

would expect a mean contact number of 4. While for the case of a random packing of ellipses one would expect a mean contact number of 6 (the extra degree of freedom being given by the angle describing the orientation of each ellipse).

The practical determination of contact numbers for computationally generated packings involves the definition of a cutoff (r_{cutoff}) distance around each particle where one considers any neighboring particle within that distance to be in contact. Figure 3.4 shows the average contact number obtained for increasing values of r_{cutoff} . (This is similar to a cumulative radial distribution function). We see that for circles there is a very sharp increase to a value of approximately four, while at higher ellipticities there is a clear plateau region in the graph at a value close to six. We find a value of 4.0 ± 0.1 for circles over the range $r_{cutoff} = 0.005 r_{avg} \rightarrow 0.007 r_{avg}$, where r_{avg} is the average semi-major length. For larger values of ellipticity a clear plateau is seen at approximately 6 and so it is appropriate to consider a larger value

of $r_{cutoff} = 0.02 r_{avg}$ in this case. Figure 3.5 shows the variation in contact number with aspect ratio where the error bars are determined from considering r_{cutoff} in the range $0.005 r_{avg} \rightarrow 0.007 r_{avg}$ for values of $\lambda \geq 0.6$ and $0.005 r_{avg} \rightarrow 0.02 r_{avg}$ for $\lambda < 0.6$.

The simple “jamming argument” is generally seen to be a very good indicator of the number contacts of particles in granular packings. However, it does imply that for an infinitesimal introduction of ellipticity there should be an immediate jump in contact number from 4 to 6. This is clearly contradicted by our simulation results, where a maximum contact number is only reached at an aspect ratio $\lambda \approx 0.7$. We find $Z = 4.0 \pm 0.1$ for circles consistent with the jamming argument, while for large ellipticities we find a value of $Z = 5.7 \pm 0.2$ for an aspect ratio of 0.3. This is slightly lower than the expected value of 6, consistent with the results of Donev [33] who found a maximum value of $Z = 9.8$ for spheroids and $Z = 11.4$ for ellipsoids to be compared with values determined from the jamming argument of $Z = 10$ and $Z = 12$.

The situation is different for *periodic* densest packings of identical ellipses. A list of 54 such packings was compiled by Nowacki [101], and was extended to 58 packings by Grünbaum and Shephard [9]. Their book details coordination numbers and packing fractions for all these packings. The density of the closest packing of circles, $\Phi_c = \Pi/\sqrt{12}$ is the conjectured maximum density of all packings, only taken by a subset of the listed 58 packings, all with coordination number six [92].

In three dimensions, quite surprisingly, the packing density of ordered arrangements of ellipsoids can exceed that for ordered sphere packing, as was shown recently by Donev [34, 68]. This is yet another indication of the intricate nature of packings and their dependence on dimensionality and order.

3.4 Conclusion

We have examined the pronounced effects that the ellipticity of grains can have on their packing properties. We have separated out the contribution to the packing of the grains from their rotational and translational degrees of freedom and demonstrated that the increase in Φ that we observe as the shape of the grains transitions from circular to elliptical is due to the additional degree of freedom that the elliptical grains have, with this large increase in Φ not observed in simulations where we disallow rotations of the grains.

We also see that the simple “jamming argument” argument that relates number of contacts to number of degrees of freedom is not valid for low ellipticities, with a smooth variation and not a discontinuous jump in contact number observed as we vary the shape of the grains away from that of circle towards a highly shape. We will further consider the packing properties of non-circular grains in Chapters 4 and 5. We will return to the subject of constraint theory in Chapter 6 when we consider the inverse packing problem.

Chapter 4

Packing Limited Growth of Arbitrarily Shaped Objects

4.1 Introduction

As was outlined in chapter 1, there exists many space filling packing models in which non-overlapping units of smaller and smaller sizes are placed according to a given set of rules. The Apollonian packing (AP) shown in Figure 1.6 in Chapter 1 is formed by filling the space between three mutually touching discs by placing a disc so that it just touches the other three. The procedure is then continually repeated, filling the new gaps generated by the addition of each new disc. If the packing consists of circles with a range in radii from r_{large} to r_{small} , then the packing fraction will be given by:

$$\phi = 1 - \left(\frac{r_{\text{small}}}{r_{\text{large}}} \right)^{d-D_f} \quad (4.1)$$

where D_f is the fractal dimension of the packing ($D_f = 1.305$ for an AP packing) and d is the number of dimensions of the system ($d = 2$ for circles) [51, 70]. This equation is valid for other space filling packing models where there is a very

wide polydispersity in the disc radii ($r_{\text{large}} \gg r_{\text{small}}$) and a power law in the size distribution as described below.

The AP model has been generalised by Manna [69] to consider the case where the centres of the discs are chosen randomly (RAP). New discs are added sequentially by choosing a random location in the packing's pore space and placing the largest possible non-overlapping disc. This model has been further extended by Andrienko, Brilliantov and Krapivsky (the ABK model) to allow multiple discs to nucleate simultaneously with a linear growth rate [17, 1, 2]. (The RAP model corresponds to the ABK model with an infinite growth rate.)

Dodds and Weitz [31] have shown some of the universal features of these models, considering them to belong to a broad class which they term "packing-limited growth" (PLG) models. In PLG models, objects are seeded randomly, grow according to a given rule and stop growing when they collide with another object. They highlight the fact that the RAP and ABK models converge as the number of objects placed increases. This is due to the pore spaces increasing in number and decreasing in size. Thus for the ABK model, collisions of growing objects will increasingly be with already placed objects forming part of the pore space walls (the sole mechanism of packing in the RAP model) and not with other growing objects.

In PLG models, the limiting distribution of the radii, $N(r)$ is described by

$$N(r) \propto r^{-\alpha} \quad (4.2)$$

for small r . The decay of the pore space volume $\rho = 1 - \phi$ with the number of packed elements n is also described by a power-law for large n with

$$\rho(n) \propto n^{-\beta}. \quad (4.3)$$

Dodds and Weitz obtain numerical estimates of α for the RAP model, and the ABK model for the cases of discs growing heterogeneously, exponentially and linearly. They find that a universal exponent $\alpha \simeq 2.56$ exists, independent of the

growth dynamics. In a further study Dodds and Weitz consider the role of shape, by considering a PLG model consisting of objects composed of rectangles [32]. They consider packings of squares, rectangles and objects formed from combining sets of rectangles: a cross, a six spoked star and an eight pointed star. They find that the α exponent characterising the size distribution of the objects is highly shape dependent, taking values in the range of $2.564 \leq \alpha \leq 3$.

In this work we consider a PLG model in which objects can have arbitrary shape. We examine the detailed role that shape plays in how PLG models behave and the effect of shape on the properties of the packings that are formed. We achieve this by generating packings of arbitrarily shaped objects in the same manner described by the RAP model. However, the RAP model is not sufficient to fully study the properties of PLG models of arbitrarily shaped objects. They in particular ignore the additional degree of freedom that non-circular objects have in two dimensions. In the RAP model studied by Dodds and Weitz, an object would stop growing on collision with an object forming part of the pore walls. However, a larger non-overlapping object can be placed, if a non-circular object is allowed to take advantage of its additional degree of freedom and to rotate by an angle that allows it to increase its size and still not overlap with any other objects (See Figure 4.1). We will term this new model Rotational Random Apollonian Growth (RRAP).

4.2 Theory

Here we will outline the PLG theory due to Dodds and Weitz [31], which demonstrates that PLG models in which objects nucleate simultaneously with a specified growth rate converge for large n to the case where objects are placed sequentially. We first consider a sphere growing in d -dimensions in a periodic box of volume V . Spheres are nucleated randomly in the unoccupied pore space at a rate κ per unit

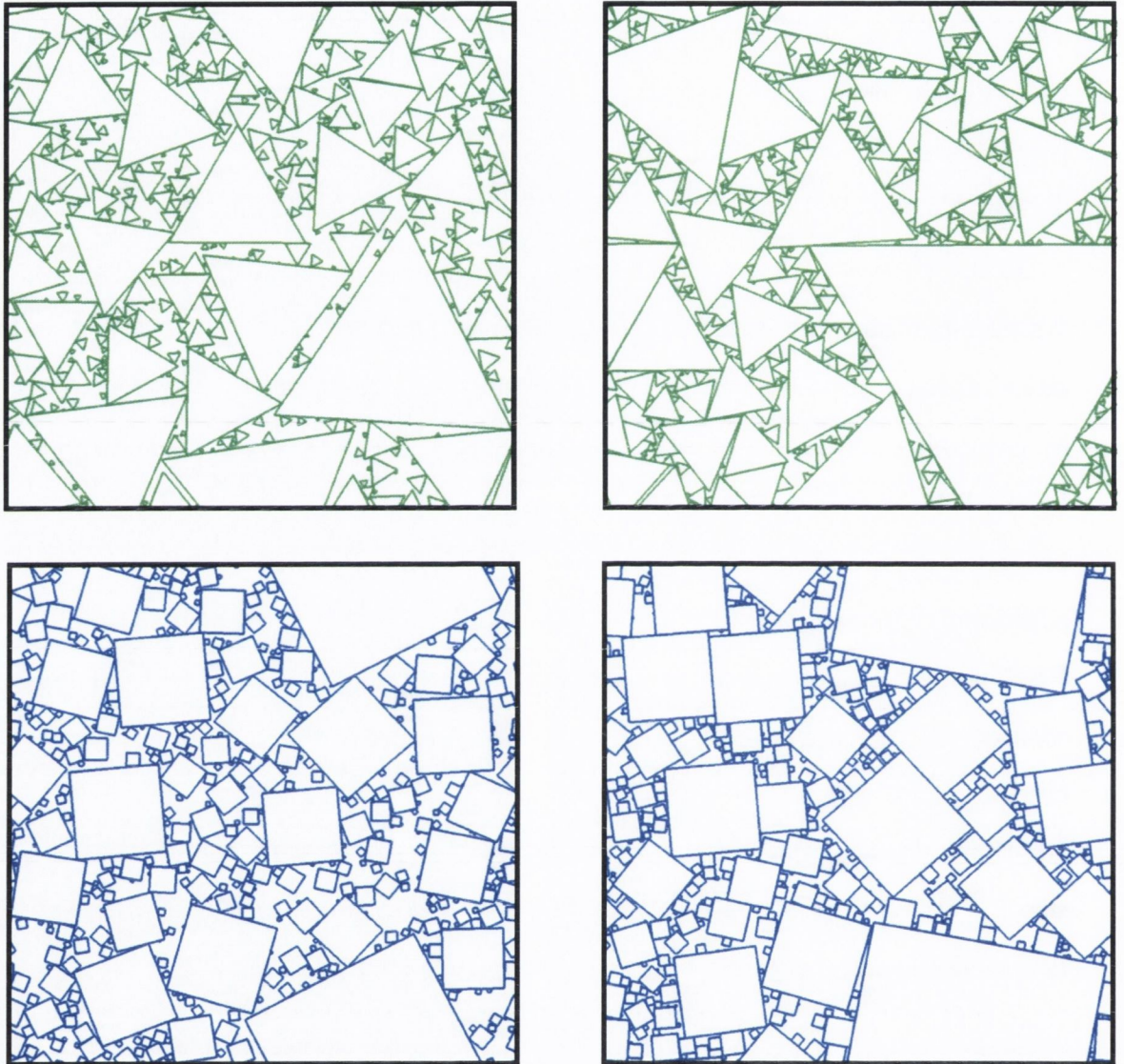


Figure 4.1: RAP packing of 500 triangles with no rotations (top left) and with rotations (RRAP) (top right). RAP packing of 500 squares with no rotations (bottom left) and with rotations (RRAP) (bottom right). The objects pack more densely in the RRAP model as a result of being able to rotate during the packing process.

volume and grow until they contact a neighbouring sphere. The i th sphere, which is injected at t_i , grows at a rate $G_i(t - t_i)$ giving the radius $r_i(t)$ as

$$r_i(t) = \int_0^{t-t_i} G_i(u) du \quad (4.4)$$

for $t \geq t_i$. It is assumed that the spheres grow in a strict monotonic fashion, *i.e.*, for each i , $G_i(t - t_i) \geq \epsilon > 0$. Neglecting growth, spheres nucleate in an individual pore Γ at a rate μ given by

$$\mu \simeq \kappa V_d \lambda^d \quad (4.5)$$

where λ is the length of the longest line that can be drawn between the edges of the boundary spheres and be contained entirely within the pore space, and V_d is the volume of a d -dimensional sphere of unit radius. The typical time τ between nucleations in Γ is, therefore,

$$\tau = 1/\mu \simeq \kappa^{-1} V_d^{-1} \lambda^{-d}. \quad (4.6)$$

If sphere i nucleates in Γ , it will reach its maximum size and jam in a time τ_{jam} that can not exceed the time it takes for its radius to reach its maximum possible value of $\lambda/2$. Using this, together with the stated assumption that $G_i(t - t_i) \geq \epsilon > 0$, we find

$$\tau_{\text{jam}} \lesssim \lambda/2\epsilon. \quad (4.7)$$

Thus when $\tau_{\text{jam}} \ll \tau$, *i.e.*, when

$$V_d \lambda^{d+1} \kappa / 2\epsilon \ll 1 \quad (4.8)$$

the packing mechanism will reduce to that of the RAP model, where spheres will be stopped upon contacting already packed spheres and not other growing spheres.

Rearranging Eqn 4.8 we see that irrelevant of the growth dynamics, all models will converge to that of the RAP model when λ_{\max} satisfies

$$\lambda_{\max} \ll (2\epsilon/V_d\kappa)^{1/(d+1)} \quad (4.9)$$

This condition must of course always eventually be fulfilled as more spheres are placed and the space fills up.

4.3 Computational Implementation

We have implemented the PLG models we will consider here in our `ARBITRARY-PACKER` software. All simulations are performed with periodic boundary conditions. All shapes are described using a discretised surface, with the exception of the circular case, where the exact contact solution is used. Where we consider straight edged objects, the discretised surface gives the exact contact solution. For the case of elliptical shapes, an approximation to the surface is made using 100 surface points. A cell list is implemented to greatly improve the computational performance of the model and details of this implementation are given in Appendix C.

Random Apollonian Packing (RAP) simulations proceed in the standard way. Initially a small number of objects are placed at random locations and with random orientations in the periodic box. New objects are then placed individually in succession in the following way. A random position in the pore space is chosen. The object is then grown until it contacts with the objects making up the walls of the pore space it is located within. This is achieved by iteratively changing the area of the object in the following way:

At each iteration the current area of the object A_{current} is increased by ΔA :

$$A_{\text{new}} = A_{\text{current}} + \Delta A \quad (4.10)$$

ΔA is initially chosen to be the final area of the previous object that was packed. If increasing the area by ΔA causes no overlap with any other object then the increase in area is accepted and ΔA is doubled for the next iteration. If on the other hand increasing the area A_{current} by ΔA causes an overlap with another object, then A_{new} is reduced to its previous value and ΔA is divided in half for the next iteration. This method proceeds until $\Delta A < A_{\text{tol}}$. For standard RAP simulations the object is then considered to be packed.

A_{tol} is chosen to be sufficiently small that it does not impact the results of the simulation.

For our new Rotational Random Apollonian Packing (RRAP) simulations, when $\Delta A < A_{\text{tol}}$, it is tested if rotating the object by any angle (in increments of 1°) would allow a larger object to be packed. If this is the case, the object is rotated and the area increased again as before. Only when no possible rotation of the object will allow its area to be increased and a zero overlap configuration to be obtained, is the object considered to be packed.

4.4 Simulation Results

Here we will present results of PLG simulations using a variety of shapes. We have simulated packings of each shape using both the traditional Random Apollonian Packing (RAP) model and our new Rotational Random Apollonian Packing (RRAP) model. For both models a power law variation of the decay in the pore space volume ρ with the number of objects packed n is found as stated in Eqn. 4.3. For each shape, we have determined the exponents β (RAP) and β' (RRAP) by fitting the power law regions of the graphs of $\log \rho(n)$ vs. $\log n$. A clear power law behaviour is evident when $N > 1000$ objects have been packed (See Figure 4.2).

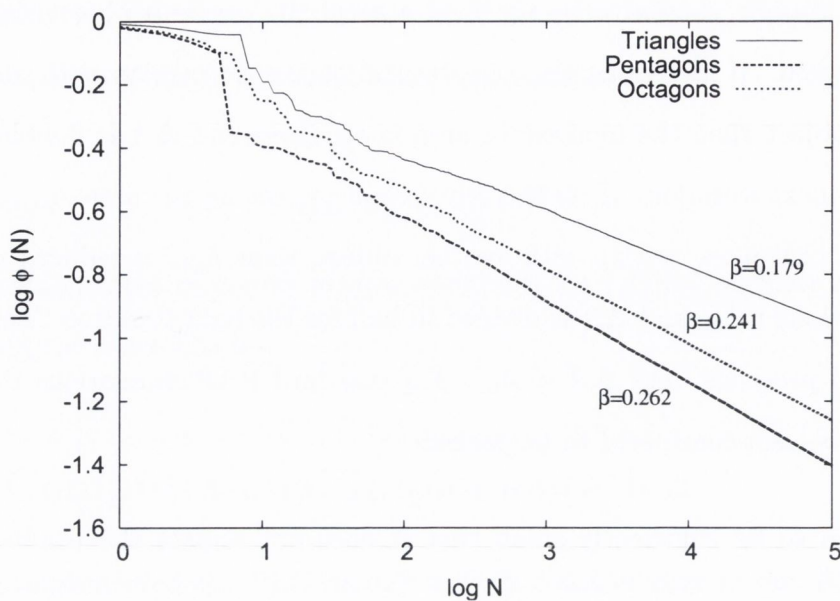


Figure 4.2: The decay of the pore space volume for triangles, pentagons and octagons. The clear power law regions can be seen by the straight lines on this log-log plot.

A power-law variation of the limiting distribution of the radii of the packed objects is also observed as in Eqn. 4.2 (See Figure 4.3). The direct measurement of β and β' is much more robust than measuring α and α' from fitting to the power-law in Eqn. 4.2. We thus determine α (RAP) and α' (RRAP) using the simple scaling relation between β and α that was demonstrated by Dodds and Weitz [31]:

$$\alpha = 1 + \frac{2}{1 + \beta} \quad (4.11)$$

Details of the derivation of this relationship are given in Appendix A.

Packings of $N = 100,000$ were generated for each shape considered using the RAP model. For the RRAP model packings of $N = 75,000$ (straight edge and concave objects) and $N = 32,000$ (ellipses) were considered. All data was averaged over five packings and the standard deviation of the estimate of α , α' , β and β' for each object was determined.

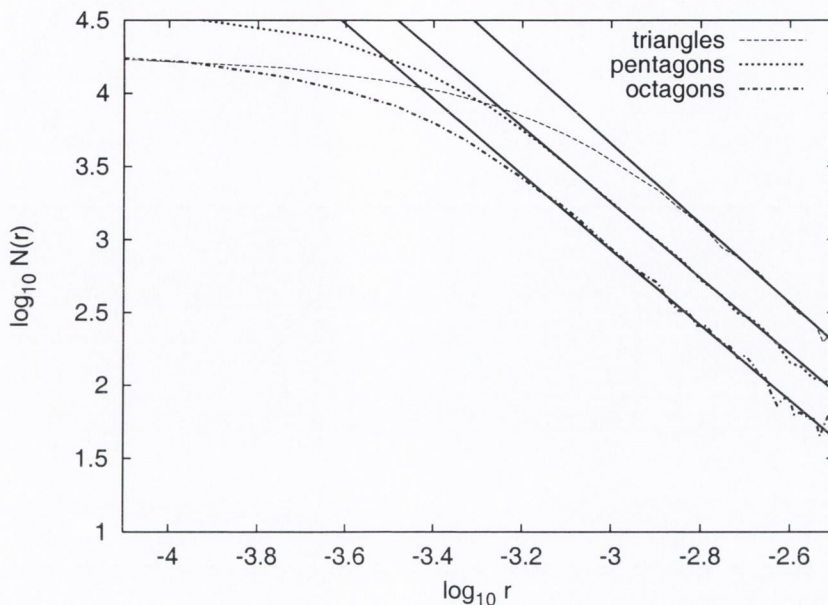


Figure 4.3: Plot of $N(r)$, the frequency of objects of size r , for triangles, pentagons and octagons. Solid lines are fits to the power law regions of the data with slopes $\alpha = 2.72 \pm 0.06$ (Triangles), $\alpha = 2.59 \pm 0.05$ (Pentagons) and $\alpha = 2.57 \pm 0.05$ (Octagons).

As an initial verification of our simulation we determined β from RAP simulations of circles and of squares, finding $\beta = 0.277(2)$ (circles) and $\beta = 0.224(2)$ (square). These are consistent with the values of $\beta = 0.278(1)$ (circles) and $\beta = 0.223(2)$ (squares) found by Dodds and Weitz [31, 32].

Estimates of α from fitting to the power-law in the limiting distribution of the radii (See Figure 4.3) have been verified to be consistent with those found from Eqn. 4.11. We find from Figure 4.3: $\alpha = 2.72 \pm 0.06$ (Triangles), $\alpha = 2.59 \pm 0.05$ (Pentagons) and $\alpha = 2.57 \pm 0.05$ (Octagons). The estimates using Eqn. 4.11 are however much more accurate as there is a much smaller error associated with determining β from fitting to the power law regions of the graphs of $\log \rho(n)$ vs. $\log n$, and hence determining α using Eqn. 4.11. From Eqn. 4.11 we find $\alpha = 2.696(1)$ (Triangles), $\alpha = 2.612(1)$ (Pentagons) and $\alpha = 2.585(2)$ (Octagons).

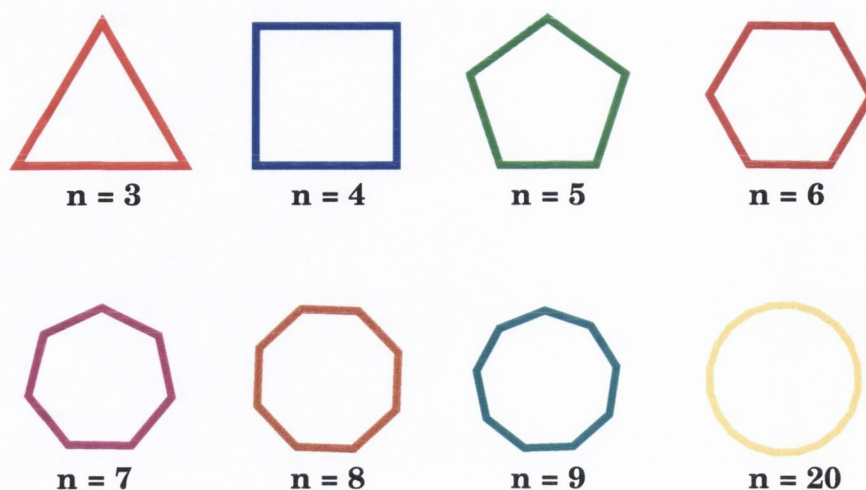


Figure 4.4: The transition from straight edged to circular objects, as the number of sides n_{edges} is increased. From left to right: triangle, square, pentagon, hexagon, septagon, octagon, nonagon and a 20 sided object.

In the discussions that follow we will focus our analysis on the variation of β and β' . As is shown from Equation 4.11, these are simply inversely related to α and α' , but the advantage of considering β and β' is that these exponents represent a measure of how well a particular object packs. Larger values of these exponents tell us that an object is filling in space faster than other objects that have smaller values. This allows us to explicitly consider the packing properties of each of the shapes considered and in the case of ellipses compare our results to those obtained for the variation of packing fraction with ellipticity in Chapter 3. Tables of values for α , α' , β and β' are given in Appendix B, along with graphs of the variation of α and α' for each of the shapes considered in this chapter.

4.4.1 The transition from straight edged to circular objects

Here we will consider the packing properties of the sequence of objects defined by the best representation of a circle that can be obtained using an object with a finite number of straight edges (See Figure 4.4). For a large number of edges, the object

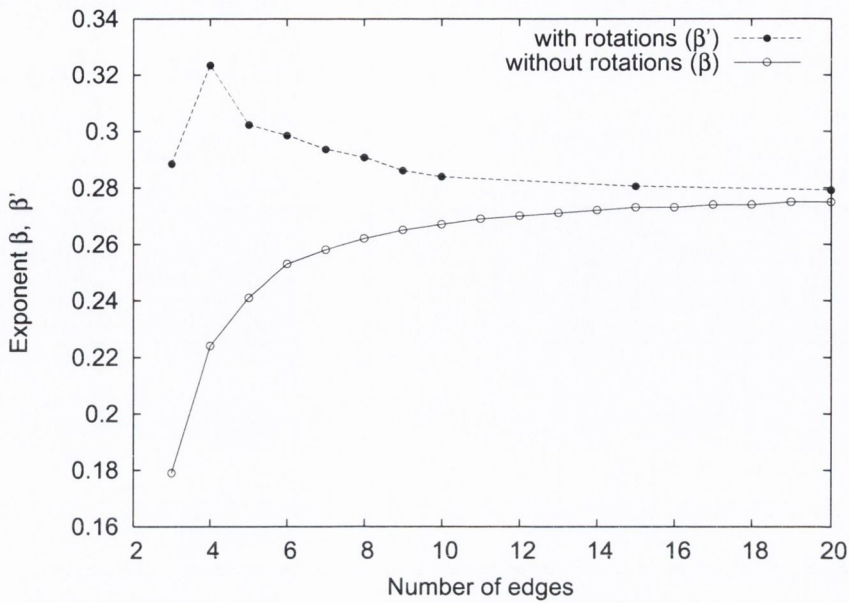


Figure 4.5: Variation of exponents β and β' as the number of edges of the packed objects increases and the objects transition for a straight edged to a circular shape.

will tend towards and exact representation of a circle. However for smaller numbers of edges we will have a progression of shapes from $n_{\text{sides}} = 3$ (equilateral triangle), $n_{\text{sides}} = 4$ (square), $n_{\text{sides}} = 5$ (pentagon) and so on.

Figure 4.2 shows the decay in pore space volume for RAP simulations of triangles, pentagons and octagons. The variation of the exponents β and β' are shown in Figure 4.5. They show a very interesting variation as the number of edges n_{edges} is increased. For the RAP case, the exponent β shows a quite smooth increase from a low value of $\beta = 0.179(1)$ for $n_{\text{edges}} = 3$ (equilateral triangle) to a value of $\beta = 0.275(2)$ for $n_{\text{edges}} = 20$.

A very different behaviour is found for our new RRAP model. The maximum $\beta' = 0.323(2)$ value is found for square objects, with objects that have either one more (pentagons) or one fewer sides (triangles) both having lower β' values. This peak is followed by a slow decrease in β' towards the value for circles, with $\beta =$

0.279(2) found for $n_{\text{edges}} = 20$. The RAP and RRAP models clearly show they converge as expected when the objects become more circular and their additional rotational degree of freedom begins to disappear.

The variation of α and α' show the inverse to the trends seen for β and β' as already noted. They vary from $\alpha = 2.696(1)$ and $\alpha' = 2.552(2)$ (Triangles) to $\alpha = 2.567(2)$ and $\alpha' = 2.564(2)$ (20-sided shape). A graph of the variation of α and α' is given in Appendix B.

4.4.2 The role of ellipticity

In chapter 3, we presented detailed results for the variation in packing fraction in random packings of ellipses when the aspect ratio of the ellipses is varied. Here we will again consider ellipses represented by a discretised surface composed of 100 edges. This gives us an extremely accurate representation of an ellipse as shown in chapter 3.

Here again we simulate packings of ellipses using both the RAP and RRAP models. The variation of β and β' with the aspect ratio (λ) of the ellipses is shown in Figure 4.7. For the RAP case, we observe an initial flat region, where the ellipses have a β value close to that of circles. For larger ellipticities, we see a very rapid drop off in β , with a value of $\beta = 0.124(1)$ found for $\lambda = 0.1$. This behaviour is very similar to what we found for the variation of packing fraction with ellipticity in random packings of ellipses where rotations of the ellipses were not allowed during the packing process (See Figure 3.3).

Simulations using the RRAP model again show a very different variation for β' . There is an initial rapid increase in β' with ellipticity, with a maximum value of $\beta' = 0.359(3)$ found for $\lambda = 0.5$. Above this value there is a slow drop off in β' , with $\beta' = 0.341(2)$ found for $\lambda = 0.1$. This behaviour is quite similar to what we found for the variation of packing fraction ϕ for random packings of ellipses (See Figure

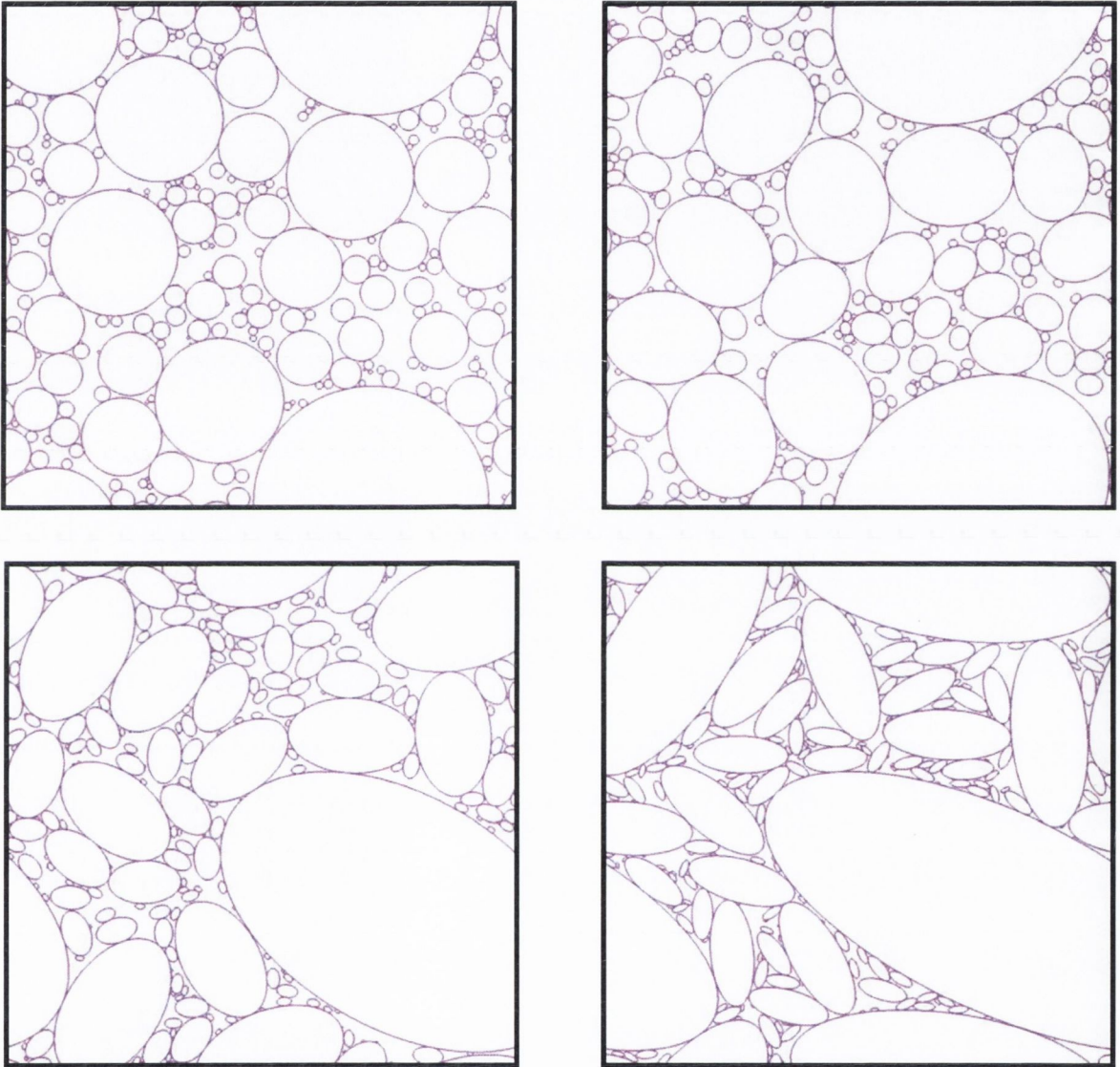


Figure 4.6: RRAP packings of ellipses with aspect ratio $\lambda = 1$ (top left), $\lambda = 0.8$ (top right), $\lambda = 0.6$ (Bottom Left) and $\lambda = 0.4$ (Bottom Right)

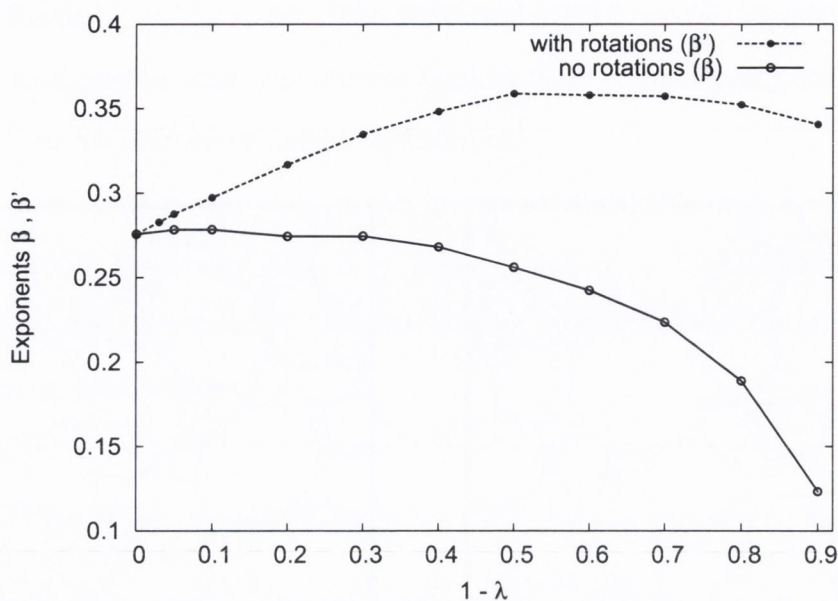


Figure 4.7: Variation of exponents β and β' with ellipticity.

3.2), although interestingly the maximum value β' is found for $\lambda = 0.5$, whereas the maximum packing fraction in random packings of ellipses is found at $\lambda = 0.7$.

The variation of α and α' again show the inverse to the trends seen for β and β' . They vary from $\alpha = 2.568(1)$ and $\alpha' = 2.568(3)$ (Circles) to $\alpha = 2.780(1)$ and $\alpha' = 2.492(2)$ ($\lambda = 0.1$). A graph of the variation of α and α' with ellipticity is given in Appendix B.

4.4.3 Concave objects considered

A shape is concave if a line segment exists connecting any two interior points that is not totally contained within the shape. Concaveness will clearly have a large effect on the packing characteristics of a shape. To enable the examination of the role of concaveness in a controlled manner, we will consider a square with a second smaller square cut out of its side to create a concave shape (See Figure 4.8). We will quantify the degree of concaveness γ as the ratio of the area of the outer large

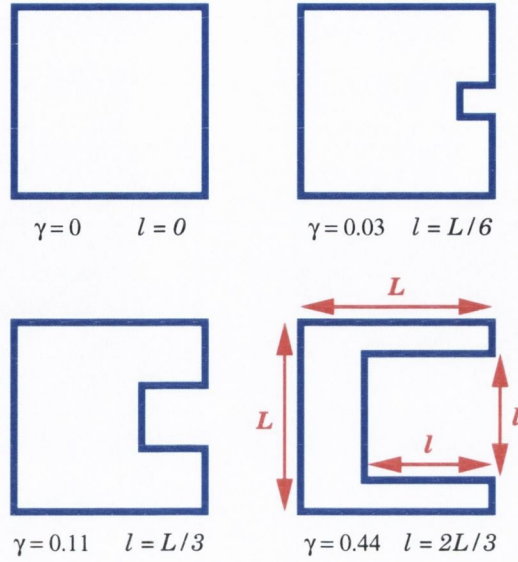


Figure 4.8: The role of concaveness is investigated by considering a large outer square with edge length L , with a second smaller inner square of edge length l cut out of its side. γ is the ratio of the area of the outer large square to the inner smaller square.

square to the inner smaller square

$$\gamma = A_{\text{inner}}/A_{\text{outer}}. \tag{4.12}$$

A γ value of zero corresponds to a perfect square, 0.5 to removing a square half the size of the outer square.

The variation of β and β' with concaveness γ is shown in Figure 4.10. We clearly see that increasing concaveness causes the objects to pack less well. Both the cases with and without rotations show the same downward trend for increasing γ . For $\gamma = 0$, we have simply a square shape, with $\beta = 0.224(2)$ and $\beta' = 0.323(2)$. β' shows a quite sharp initial decrease with increasing concaveness γ , followed by a near linear decrease for larger values of γ up to $\gamma = 0.81$. β shows less of an initial sharp decrease with γ and appears to decrease at a close to linear rate up to $\gamma = 0.81$. Both β and β' appear to tend toward zero for $\gamma \rightarrow 1$ as expected, since at $\gamma = 1$ the

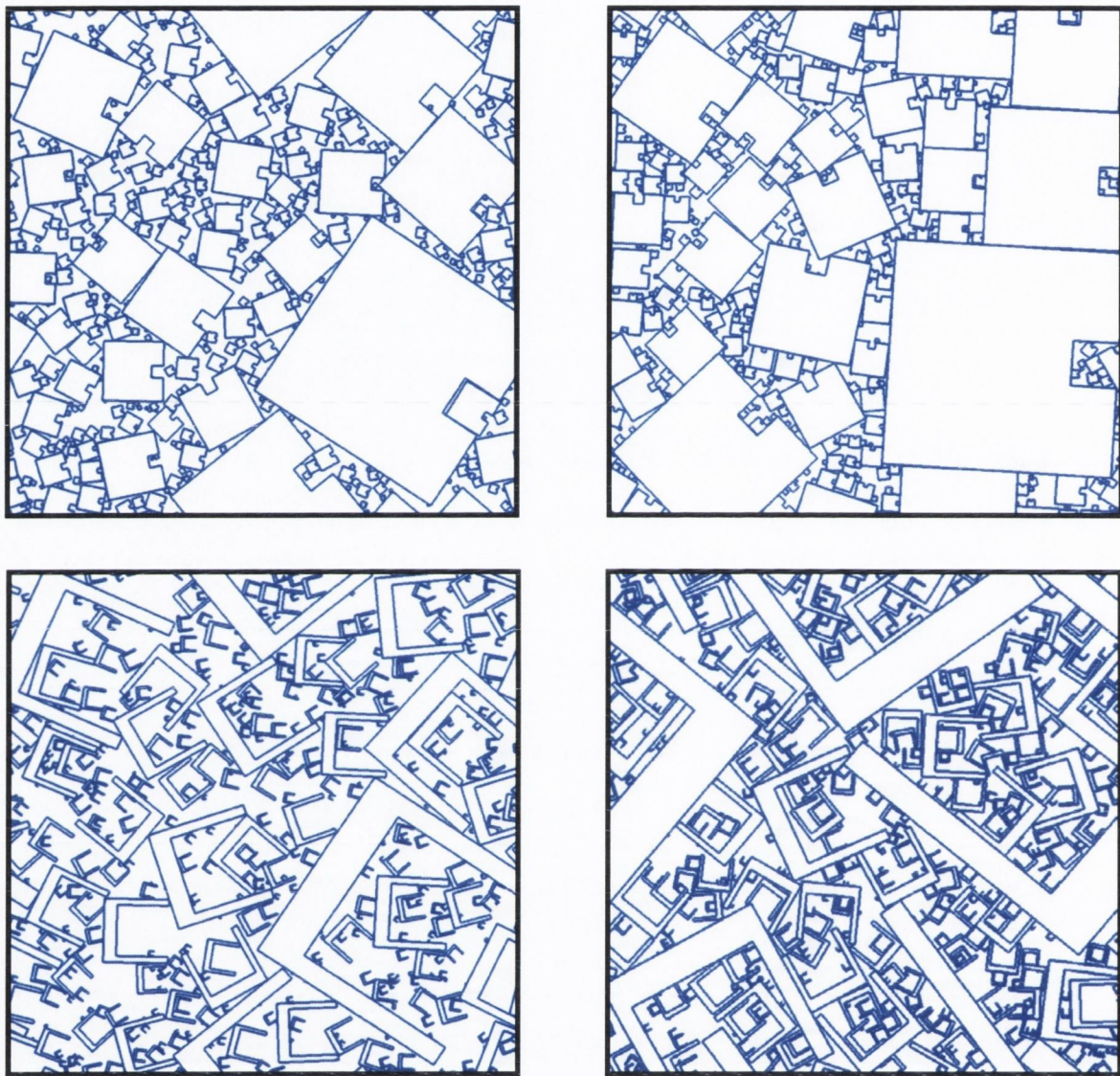


Figure 4.9: RAP packing of 500 concave objects with $\gamma = 0.04$ with no rotations (top left) and with rotations (RRAP) (top right). Packing of 500 concave objects with $\gamma = 0.64$ with no rotations (bottom left) and with rotations (RRAP) (bottom right).

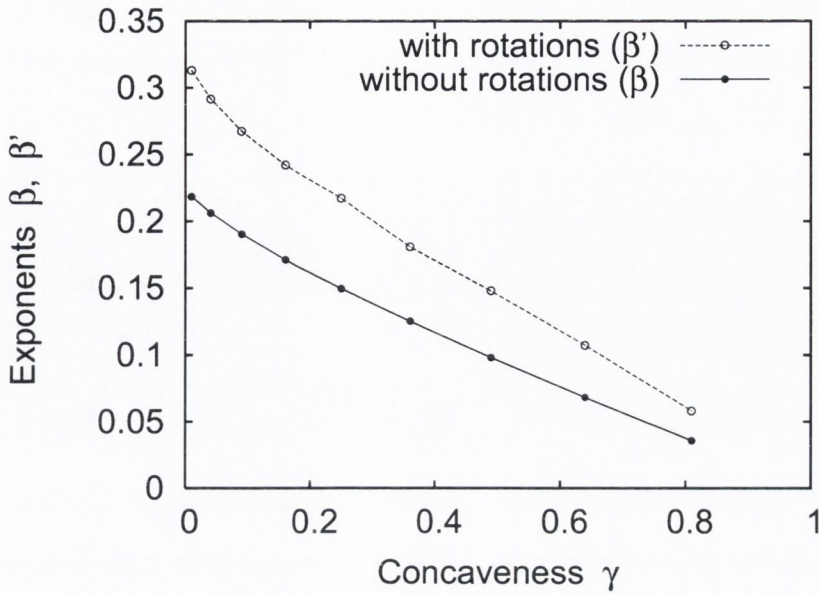


Figure 4.10: Variation of exponents β and β' with the concaveness γ of the object.

shape would have zero area. β shows less of an initial sharp decrease with γ and appears to decrease at a close to linear rate up to $\gamma = 0.81$.

α and α' do of course again show the opposite trend to β and β' . They vary from $\alpha = 2.634(2)$ and $\alpha' = 2.511(2)$ ($\gamma = 0$) to $\alpha = 2.931(1)$ and $\alpha' = 2.890(2)$ ($\gamma = 0.81$), converging toward their maximum value of 3. A graph of the variation of α and α' with γ is given in Appendix B.

4.5 Conclusion and Outlook

We have quantified the role that shape plays in RAP simulations of objects of arbitrary shape. We have also considered a new variation on the traditional theme of Random Apollonian Packing, by introducing our new RRAP model, which considers the additional degree of freedom which an asymmetric object has. Allowing such objects to rotate during the packing process allows them to increase their size and

thus the density of the packing. We have seen that this additional degree of freedom has a very pronounced effect for asymmetric objects. Large differences are found for the power-law exponents that govern the decay in pore space area (β and β') and the size distribution of the radii (α and α').

We have defined and examined an interesting progression from straight edged to circular objects. This shows the convergence of the new RRAP model and the RAP model as the shape of the object transitions to circular and the additional degree of freedom disappears. Interestingly square shapes show the largest value of $\beta' = 0.323$, with both objects with one few edges (equilateral triangles) and one greater edge (pentagons) showing lower values. The exact reason for this is unclear, but it is particularly unusual given that the β value for a square shape in the RAP model follows the overall smooth trend observed from the triangular to the circular shape (See Figure 4.5).

Our simulations of ellipse packings in the RAP and RRAP model show a very similar behaviour for the variation of β and β' to the observed variation in the packing fractions obtained in random packings of ellipses in Chapter 3. For RAP simulations we see that the introduction of ellipticity has little impact on the β values obtained at low ellipticities, but that there is a rapid drop off in β at high ellipticities. β' shows a rapid increase as we transition from a circular object, reaching a maximum at $\lambda \approx 0.5$. This maximum value is at a larger ellipticity than the ellipticity for which the maximum packing fraction was obtained in Chapter 3 and there also is only a slight decrease in β' as we transition to highly elliptical objects at $\lambda = 0.1$, compared to the rapid drop off in packing fraction seen in Chapter 3.

We have also demonstrated the contribution that concaveness can make to the packing behaviour in both the RAP and RRAP models. By considering a square shape with a second square cut out of one of its edges, we are able to quantify how the degree of concaveness of an asymmetric object effects its behaviour. We see a

rapid drop off in the value of both β and β' as the shape becomes more concave.

PLG type models of the kind considered here have an applicability to a wide variety of physical and biological problems. Aste has highlighted the similarities between such models and the distribution of tin drops generated by vapour depositions onto a substrate [3]. It has been suggested by Dodds and Weitz that PLG type models could be extended to provide accurate descriptions of biological systems, by imposing a notion of aggregation, competition and death into simulations [32]. This could then be used for example to consider how geometry impacts the structure of plant communities.

A key challenge that remains is the reliable theoretical estimation of the power-law exponents observed in PLG type simulations. Previous attempts at such estimations have had limited success. Dodds and Weitz have been able to predict values for α and β that do appear to be accurate upper and lower bounds, however they are only a good estimate of the values of the exponents for spheres in $d = 4$ where they estimate a value of $\hat{\beta} = 0.04348$ compared to the value found from simulations of $\beta = 0.0434(2)$. In $d = 2$, even estimations for the simplest case of circular packings are not accurate, with their estimate $\hat{\beta} = 0.1429$ quite far from the value of $\beta = 0.278(1)$ found from simulation.

This work has also highlighted the importance of the additional degree of freedom of asymmetric shapes in PLG type packings. Future theories which aim to provide accurate descriptions of the behaviour of such PLG type systems, will need to carefully consider this contribution.

Chapter 5

Packing-driven shape evolution of grains.

5.1 Introduction

In this chapter we will consider a model in which the shape of randomly packed two-dimensional grains are allowed to evolve based on how the grains themselves pack together. It was originally inspired as a simple model that could yield insights into how the structure of the random packing of pebbles/stones influences their resulting shapes. In considering the model in this context, it was desired to separate and highlight the contribution to the shape of the grains from the loss of matter due to the abrasion that occurs where the grains contact when they are randomly packed together. If we consider this to be the sole driving force for the shape-evolution of the grains, what is the resulting shape? It also represents an interesting model in its own right, providing a variation on traditional random packing studies in which the shape of the individual elements in the packing is fixed.

In nature there are numerous examples of packings of objects with *variable* shapes, from the pebbles on a beach, to snow flakes, to the various elements that

make up the soil [8]. All natural granular materials show a tendency for their shape to change over time. This is due both to the interactions of the grains with one another and interactions with their surroundings. If we consider the example of packings of pebbles on a beach [38], no two pebbles will have an identical shape. However we can say a lot about the general shape of the pebbles. In many cases the pebbles are well described as ellipsoidal, however a variety of shapes are observed. These shapes can be largely influenced by the shape of the stone fragment that initially broke off from a large stone deposit. The shapes of these fragments can depend heavily on the type of rock. Granites tend to break into fragments with roughly equal axes, sandstone and limestones into tabular slabs, and shales and slates, which have a finer parallel texture, shatter into thin sheets [10].

There are in general many potential dynamic effects that will influence the shape evolution of pebbles on a beach or other objects that are subject to abrasive forces, including weathering effects from the wind and sea, and abrasive forces from the pebbles themselves as they rub and knock against one another [38]. As the erosion processes that cause the shape evolution of pebbles on a beach occur over such long time scales it is impossible to obtain definite information on the shapes which preceded the shape that we observe for each pebble. This may be overcome by considering appropriate experimental and computational systems [77, 60]. Rayleigh considered chalk pebbles, initially shaped as prolate or oblate spheroids, abraded by rotating a single pebble in a container with either steel nuts, nails or small shot [67]. He found that the axes tended to approach equality, however the pebbles disappeared before the spherical form was obtained. He also observed flint pebbles taken from a beach and found that they were well approximated as ellipsoidal, with the pebbles observed sometimes being somewhat flattened at the poles and even in some cases slightly concave. Experiments performed by Rayleigh using steatite pebbles in the shape of flat disks, found that when the abrasive masses were of the

comparable size to the pebble itself a definite concavity developed on the initially flat faces, while the edges of the pebble became more rounded.

When limestone particles, that are initially jagged and irregular in shape undergo erosion by rotating a number of them in a tumbling barrel, the particles become smaller and rounder with increasing time [60]. They also appear to initially show a tendency to an elliptical type shape.

There have been many approaches used in the computational modelling of erosion processes. Pellegrin has simulated individual abrasive particles using randomly generated polyhedrons [28]. The resulting shapes of the polyhedra are generated by cutting the particles with planes possessing random orientation and penetration-depth. The results are compared to silicon carbide abrasive particles which exhibit a random polyhedral shape.

Other dynamic models have considered particles that are discretised on a lattice, with each lattice site representing a small volume of the particle joined by a bond to its neighbours [22]. If the force on that bond exceeds a certain value due to externally applied force, the bond is broken. A site or cluster of sites is worn away when all bonds connecting the site or the cluster are broken.

These models in general consider the abrasive forces that occur when the individual grains collide or rub against each other [27]. They focus on the effect of single impacts between the grains, considering for example the effects of the impact angle and the surface properties of the materials. They do not consider the effect that the structure of a packing of the grains could have on the abrasion that grains would experience when randomly packed together. When a large number of grains are densely packed together, they will only contact each other at certain points on their surfaces. If they just experience abrasive forces at these points what will be their shape evolution? The novel packing model which we will now present can give us some insight into this question.

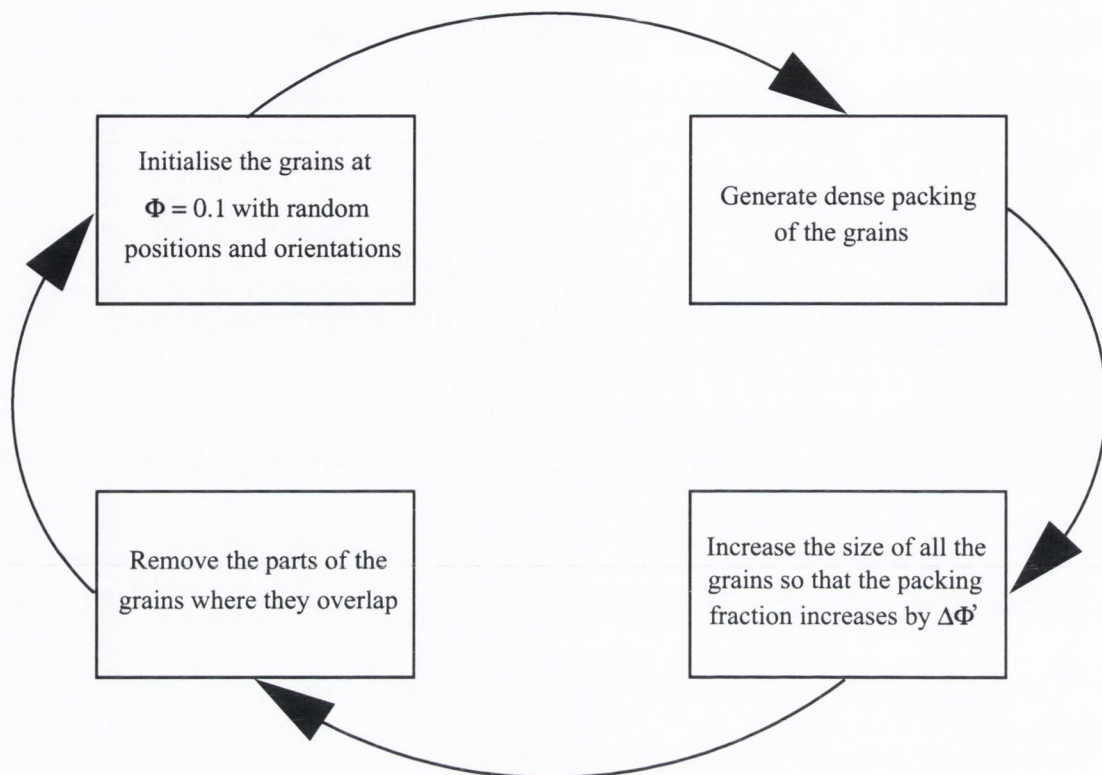


Figure 5.1: Flow diagram showing the order of events in the simulation of our erosion model. We refer to one complete cycle as one iteration i .

5.2 Description of the Model

The packing-driven shape evolution of grains model that we consider here is implemented in our `ARBITRARYPACKER` software. The order of events in the simulation is shown in Figure 5.1. We initialise the grains in a periodic box, with random positions and orientations, at a very low packing fraction ($\Phi = 0.1$). We then generate a random packing using the same algorithm that was used for the ellipse packings in chapter 3, again representing the grains as polygons with one hundred surface points. The packing algorithm consists of increasing the packing fraction in increments of $\Delta\Phi$, and reducing the overlap of the grains to zero by randomly varying the positions and orientations of the grains. This is iterated until a dense packing is achieved (see Section 3.2 for a detailed description). We assume that the ero-

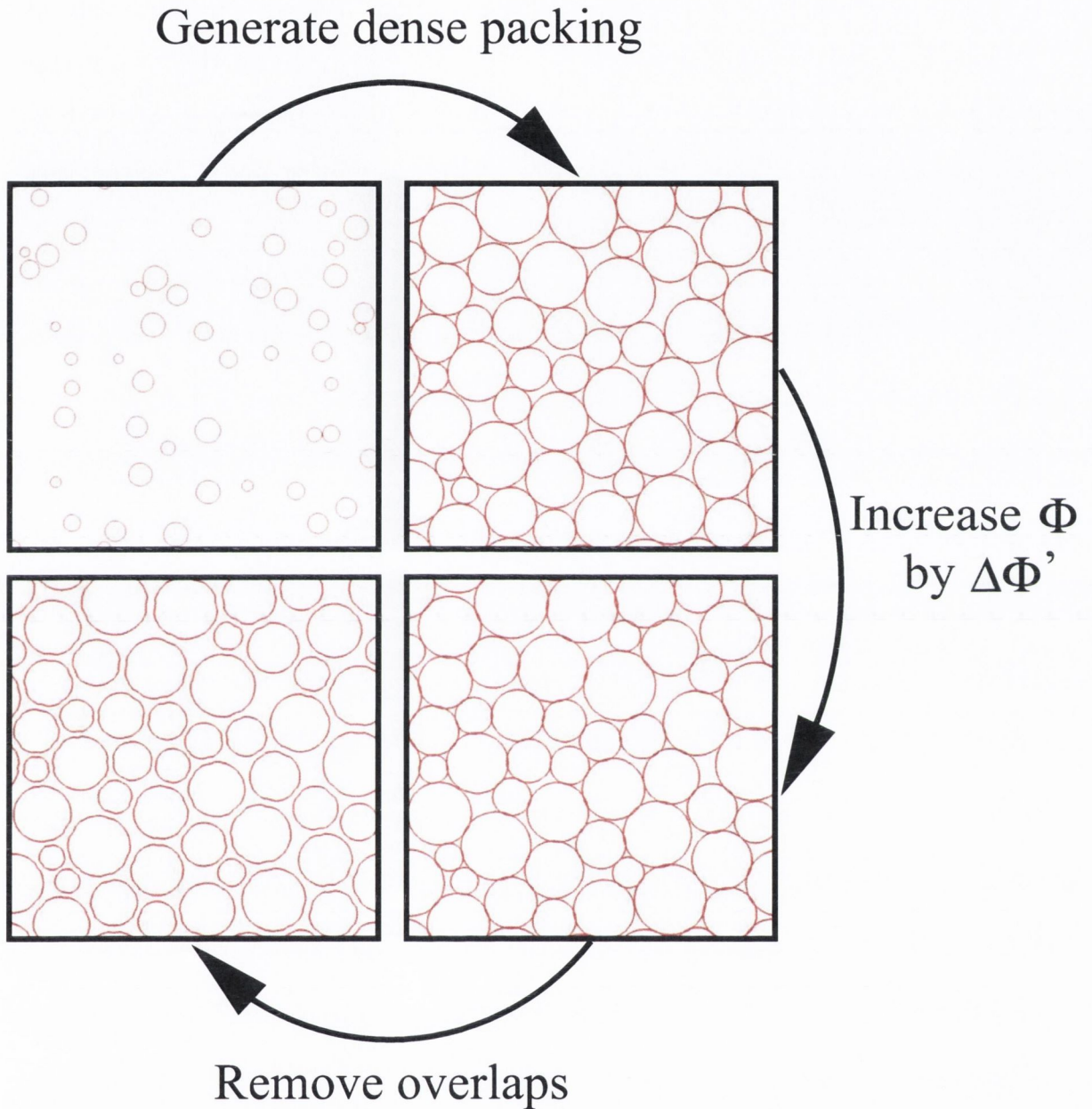


Figure 5.2: A dense packing of the grains is generated. The packing fraction Φ is increased by $\Delta\Phi'$ ($\Delta\Phi' = 0.04$ in the example shown) by uniformly increasing the size of all of the grains so that they overlap. The parts of the grains that overlap are then removed.

sion that takes place between grains occurs where they contact each other in the packing. We thus remove a small amount of each grain where it contacts with its neighboring grains. This is achieved by increasing the packing fraction by $\Delta\Phi'$ (the erosion parameter) by increasing the size of each grain so that it overlaps with its neighboring grains. The parts of each grain that overlap with other grains are then removed (See Figure 5.2). The simulation is then reinitialised at $\Phi = 0.1$ and the process is repeated to generate a new packing. The simulation proceeds by successive generation of random packings and removal of a small amount of each grain as described.

5.3 Measures of Shape

To quantify the variation of the shape of the grains and the system state as the simulation proceeds we measured the packing fraction Φ , the area-perimeter ratio f_{AP} , the convexity ratio f_C and the standard deviation of the areas of the grains σ_{area} [60, 48]. For a 2D particle, the area-perimeter ratio is defined as:

$$f_{AP}(X) = \frac{4\pi A(X)}{(P(X))^2} \quad (5.1)$$

where $A(X)$ is the area of the particle X and $P(X)$ is the perimeter. This ratio gives a measure of the roughness and the deviation from a circle. For a circle $f_{AP}(X) = 1$ and for anything else $f_{AP}(X) < 1$.

The convexity ratio is defined as:

$$f_C(X) = \frac{A(X)}{A(C(X))} \quad (5.2)$$

where $A(C(X))$ is the area of the convex hull of X . This ratio shows deviations from convexity. For a convex shape $f_C(X) = 1$ and for any concave shape $f_C(X) < 1$.

The standard deviation of the areas of the N grains is defined as:

$$\sigma_{\text{area}} = \sqrt{\frac{1}{N-1} \sum_{k=1}^N (A_k - \bar{A})^2} \quad (5.3)$$

where \bar{A} is the average area of the grains.

5.4 Simulation Results

We have extensively examined the effect of varying the system parameters in the simulation. We will present results showing the effects of varying the:

- the number of grains in the simulation
- the initial shape of the grains
- the initial range of sizes of the grains
- the rate of packing $\Delta\Phi$ (inversely related to average packing density)
- the amount of each grain removed during the erosion step (proportional to $\Delta\Phi'$).

The computational demands of considering grains that have an arbitrary shape are extremely large. In the results presented here where we have performed simulations exploring a broad range of parameter values, approximately 10,000 CPU hours were used on a cluster composed of AMD Opteron CPUs running at 2.4 GHz.

From considering the results of varying the system parameters, a clear picture emerges of the behaviour of the model. We will first present results where the system has been packed using the same $\Delta\Phi = 0.0001$ as in chapter 3. We will then consider simulations where $\Delta\Phi = 0.001$. For these simulations the packing fractions obtained are slightly lower, but the running-time of the simulations is substantially reduced, allowing us to better examine the long term behaviour of the system. (In the following sections we will refer to simulations performed with $\Delta\Phi = 0.0001$ as our short term simulations and those with $\Delta\Phi = 0.001$ as our long term simulations). Finally we will outline the effects of varying the number of grains in the simulation, the initial shape of the grains and the initial range of sizes of the grains.

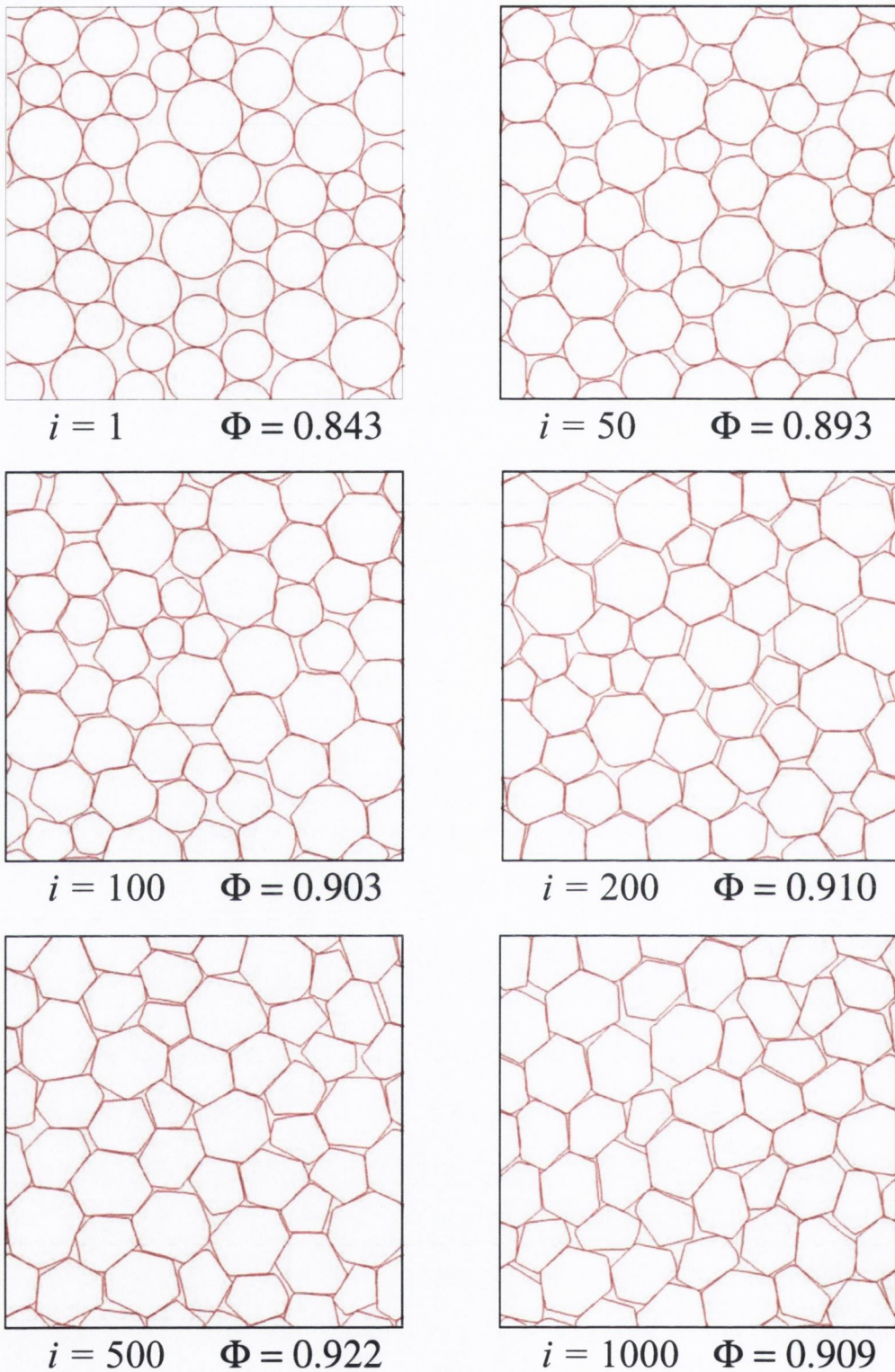


Figure 5.3: Images showing the evolution of the shapes of the grains for a short term simulation with $\Delta\Phi' = 0.01$. The simulations use periodic boundary conditions. i indicates the number of iteration steps where one step corresponds to a full cycle in the flow diagram of Figure 5.1. By iteration $i = 1000$ the grains have taken on the shape of irregular pentagons and hexagons.

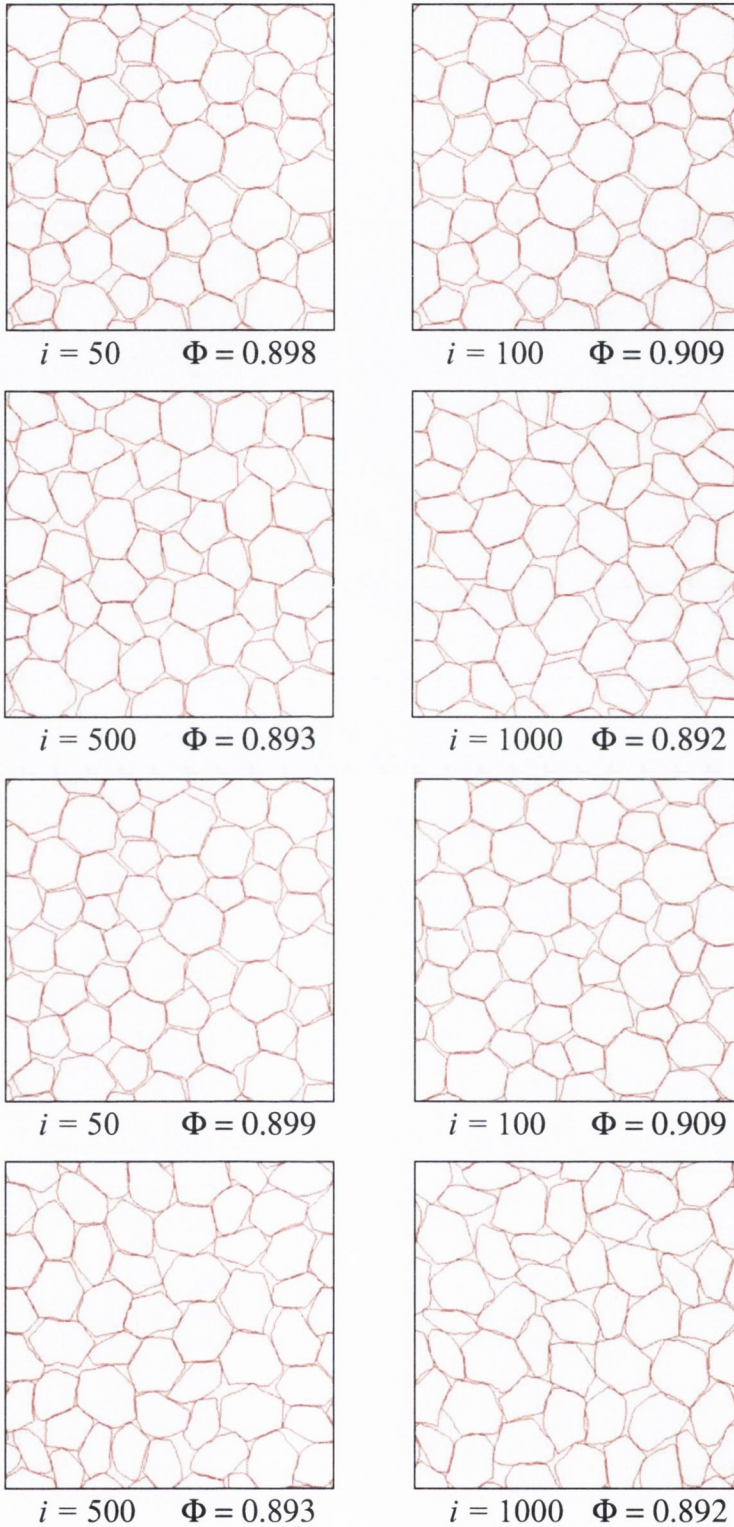


Figure 5.4: The top 4 images show the evolution of the shapes of the grains for a short term simulation with $\Delta\Phi' = 0.02$. The bottom 4 images are for the simulation with $\Delta\Phi' = 0.03$. Both simulations show the grains again forming irregular pentagonal and hexagonal shapes. The simulations with $\Delta\Phi' = 0.03$ produce grains that are visibly more jagged.

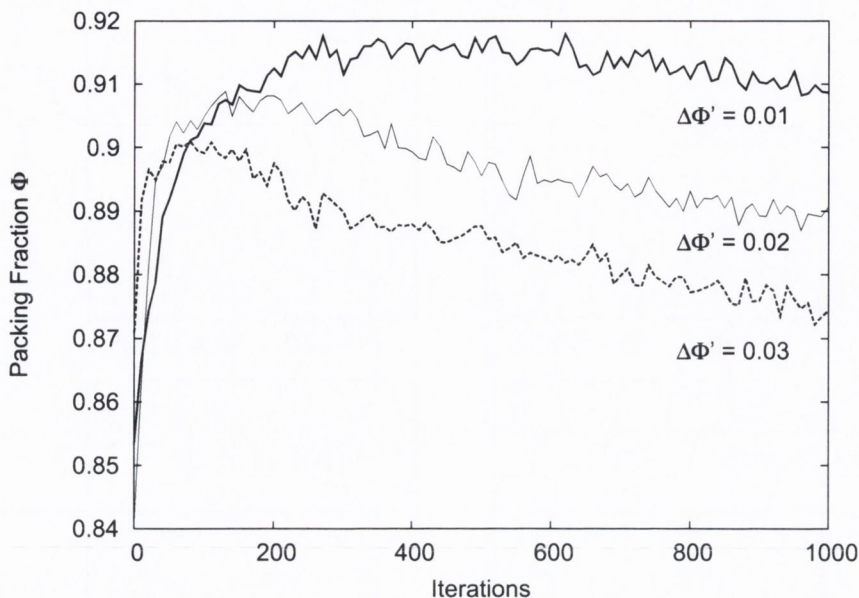


Figure 5.5: Moving average (taken over 10 iterations) of the packing fraction with number of iterations for $\Delta\Phi' = 0.01$, $\Delta\Phi' = 0.02$ and $\Delta\Phi' = 0.03$.

5.4.1 Short Term Simulations

In the short term simulations considered in this section, the grains were initialised with a circular shape. The radii of the circles were randomly distributed uniformly in the range $r_{\min} = 1 \rightarrow r_{\max} = 2$. We will consider three different simulation runs, with the erosion parameter set to $\Delta\Phi' = 0.01$, $\Delta\Phi' = 0.02$ and $\Delta\Phi' = 0.03$. For these simulations with $\Delta\Phi = 0.0001$ we were able to obtain data for runs lasting up to 1000 iterations of the simulation.

When we initialise the system using circular grains, there is an initial rapid increase in packing fraction during the first iterations. Over the first few hundred iterations, the shapes of the grains begin to deviate from their original circular shape. They clearly form straight edges, and then begin to take on the shape of irregular pentagons and hexagons (see Figure 5.3).

Variation of the moving average of the packing fraction (each measurement being the average of the packing fraction over ten iterations) is shown in Figure 5.5. After

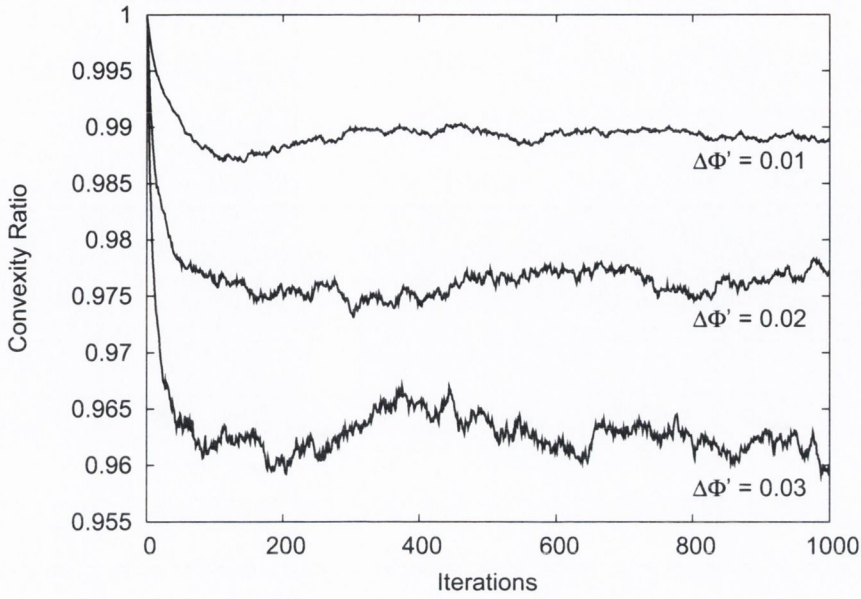


Figure 5.6: Variation of convexity ratio with number of iterations for $\Delta\Phi' = 0.01$, $\Delta\Phi' = 0.02$ and $\Delta\Phi' = 0.03$.

the initial rapid increase in packing fraction Φ during the early iterations, the system reaches a maximum packing fraction of $\Phi \approx 0.915$ after 300 iterations for the system with $\Delta\Phi' = 0.01$. For larger values of $\Delta\Phi'$ the maximum packing fraction is reached slightly earlier and has a lower value as can be seen from Figure 5.5. After this there is an overall slow decrease in the packing fraction Φ as the simulations proceed. The packing fraction Φ is generally higher for systems where a smaller amount of each grain is removed during the erosion process (lower $\Delta\Phi'$ value). For large values of $\Delta\Phi'$, the grains become more jagged, as can clearly be seen from the behaviour of the convexity ratio (Figure 5.6). The convexity ratio falls rapidly from its initial value of 1 (circular grains) to stabilise around $f_C = 0.990 \pm 0.001$ for $\Delta\Phi' = 0.01$, $f_C = 0.977 \pm 0.002$ for $\Delta\Phi' = 0.02$ and $f_C = 0.964 \pm 0.003$ for $\Delta\Phi' = 0.03$.

The variation of the standard deviation of the normalised areas of the grains with the number of iterations is shown in Figure 5.7. For the simulations with $\Delta\Phi' = 0.01$ and $\Delta\Phi' = 0.02$, σ_{area} shows a consistent decrease as the simulation proceeds. For

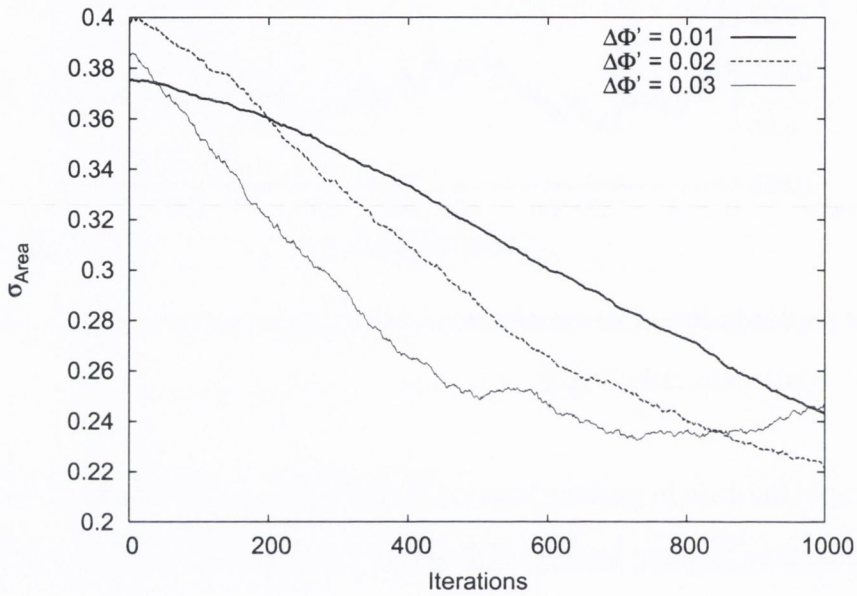


Figure 5.7: Variation of the standard deviation σ_{area} of the areas of the grains with number of iterations for $\Delta\Phi' = 0.01$, $\Delta\Phi' = 0.02$ and $\Delta\Phi' = 0.03$. Simulations using $\Delta\Phi' = 0.01$ and $\Delta\Phi' = 0.02$ show the same slow convergence in the areas of the grains, while the simulation with $\Delta\Phi' = 0.03$ shows a different behaviour, with σ_{area} appearing to stabilise somewhat after approximately 600 iterations.

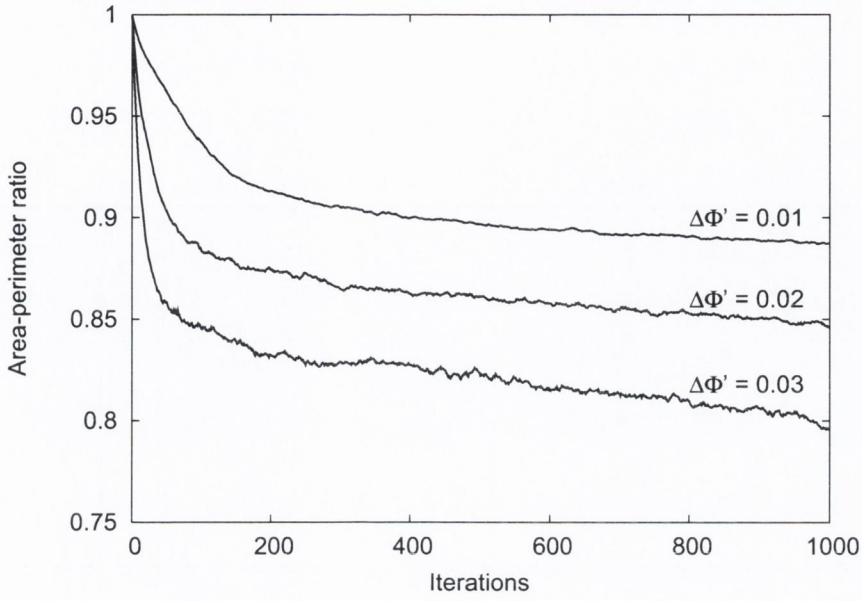


Figure 5.8: Variation of the average area-perimeter ratio f_{AP} of the grains with number of iterations for $\Delta\Phi' = 0.01$, $\Delta\Phi' = 0.02$ and $\Delta\Phi' = 0.03$.

the simulations with $\Delta\Phi' = 0.03$, σ_{area} shows an initial decrease, but then appears to stabilise somewhat and fluctuate around a value of $\sigma_{\text{area}} = 0.24$. This change in behavior of the model indicates that $\Delta\Phi' = 0.03$ may be too large a value to use. At larger values of $\Delta\Phi'$ increasingly unusual effects are possible. For very large values of $\Delta\Phi'$ it is for example possible to entirely remove a grain from the simulation by it having a complete overlap with neighboring grains.

Figure 5.8 shows the variation in the area-perimeter ratio f_{AP} of the grains. After an initial rapid decrease in f_{AP} the values appear to stabilise, with larger values found for larger values of $\Delta\Phi'$. We will consider this further in the next section when we look at longer simulation runs.

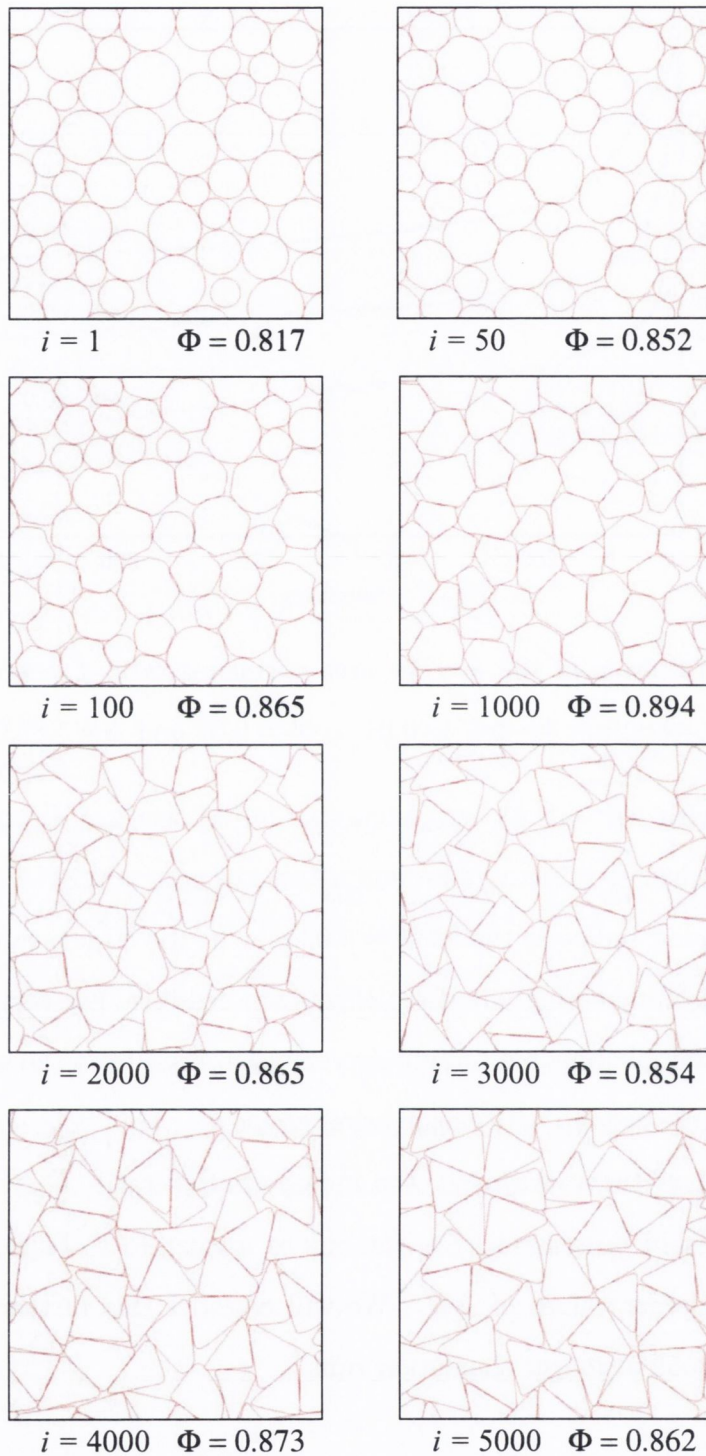


Figure 5.9: Images showing the evolution of the shapes of the grains for a long term simulation ($\Delta\Phi = 0.001$) with $\Delta\Phi' = 0.01$. By iteration $i = 5000$ the grains have clearly become triangular in shape.

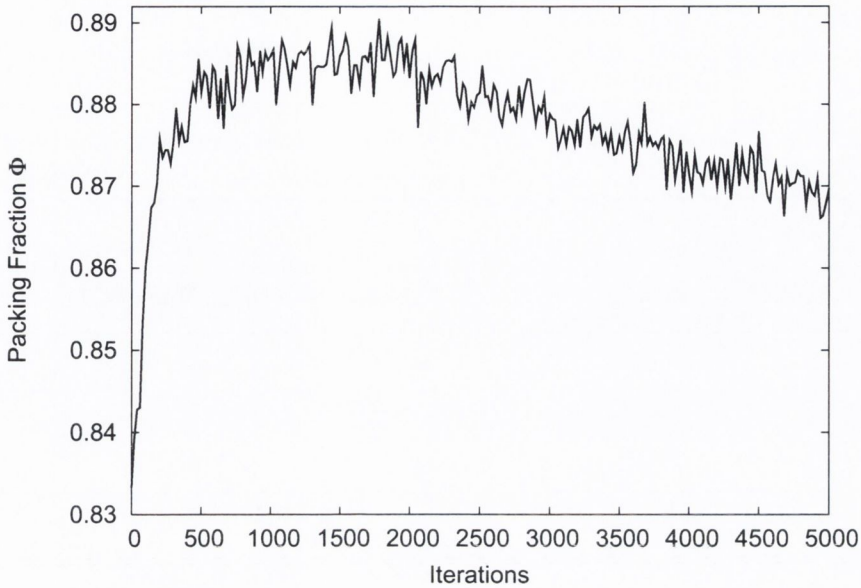


Figure 5.10: Moving average of the packing fraction Φ (each measurement taken over 10 iterations) for the long term simulation ($\Delta\Phi = 0.001$).

5.4.2 Long Term Simulations

In simulations considered in this section, the grains were again initialised with a circular shape, with the radii of the circles randomly distributed uniformly in the range $r_{\min} = 1 \rightarrow r_{\max} = 2$. We use a value of $\Delta\Phi = 0.001$ to generate packings with slightly lower average packing fraction than those considered in the previous section, with the added advantage that the runtime of the simulations is greatly reduced. We also use a value of $\Delta\Phi' = 0.01$ in all simulations considered in this section.

As a result of the reduced runtime of the simulations with $\Delta\Phi = 0.001$, we are able to consider simulations run over 5000 iterations compared to those run over only 1000 iterations in the previous section. In Figure 5.9 we show the variation of the shapes of the grains as the simulation proceeds. Over the first 1000 iterations, the shapes of the grains behave in a very similar manner to the simulations presented in the previous section with $\Delta\Phi = 0.0001$ and $\Delta\Phi' = 0.01$ (see Figure 5.3). We again see an initial deviation of the grains from their original circular shape. They

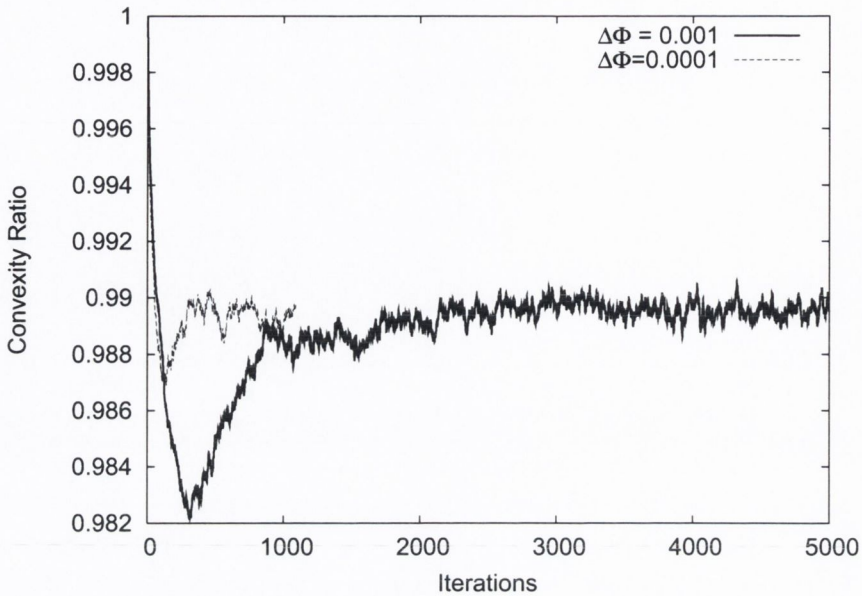


Figure 5.11: Variation of the convexity ratio f_C with number of iterations for the long term simulation ($\Delta\Phi = 0.001$). The data for the equivalent short term simulation ($\Delta\Phi = 0.0001$) is shown for comparison.

again clearly form straight edges, and have clearly taken on the shape of irregular pentagons and hexagons by iteration $i = 1000$. As the simulation proceeds the grains begin to take on a triangular shape, and by iteration $i = 3000$ the majority of grains are best described as triangular, with three straight edges meeting at rounded corners. By iteration $i = 4000$ all the grains are best described as triangular and this is still the case at iteration $i = 5000$.

The variation of the moving average of the packing fraction Φ is shown in Figure 5.10. This behaves very similarly to that observed in the previous section for the simulation with $\Delta\Phi = 0.0001$ and $\Delta\Phi' = 0.01$ (see Figure 5.5). We again see an initial rapid increase in packing fraction as the shape of the grains changes from circular to that of irregular pentagons and hexagons. The maximum packing fraction reached in this case is $\Phi \approx 0.885$, which is as expected lower than the maximum of $\Phi \approx 0.915$ obtained for the simulation with $\Delta\Phi = 0.0001$. This is followed by a slow

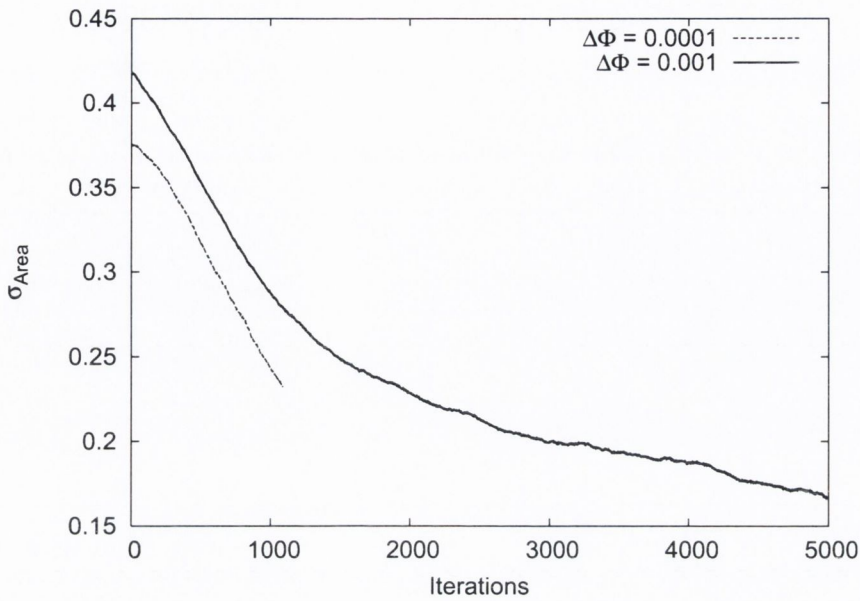


Figure 5.12: Variation of the standard deviation σ_{area} of the area of the grains with number of iterations for long term simulations ($\Delta\Phi = 0.001$). The data for the equivalent short term simulation ($\Delta\Phi = 0.0001$) is shown for comparison.

decrease in Φ as the simulation proceeds and the grains become triangular in shape. The slow decrease appears to continue or somewhat stabilise as we reach iteration $i = 5000$ where $\Phi \approx 0.86$.

In Figure 5.11 we show the variation of the convexity ratio. Initially there is a decrease, followed by a small increase in the convexity ratio, as the grains develop straight edges and take on the shape of irregular pentagons and hexagons. The convexity ratio then stabilises at a value of around $f_C \approx 0.99$, the same as in the simulation with $\Delta\Phi = 0.0001$ as shown in Figure 5.6.

The variation of the standard deviation of the normalised areas of the grains σ_{area} with the number of iterations is shown in Figure 5.12. This shows a consistent decrease as the simulation proceeds, as was the case for the simulation with $\Delta\Phi = 0.0001$ (See Figure 5.12). The rate of decreases appears to slow as the simulation proceeds and the grains take on a triangular shape.

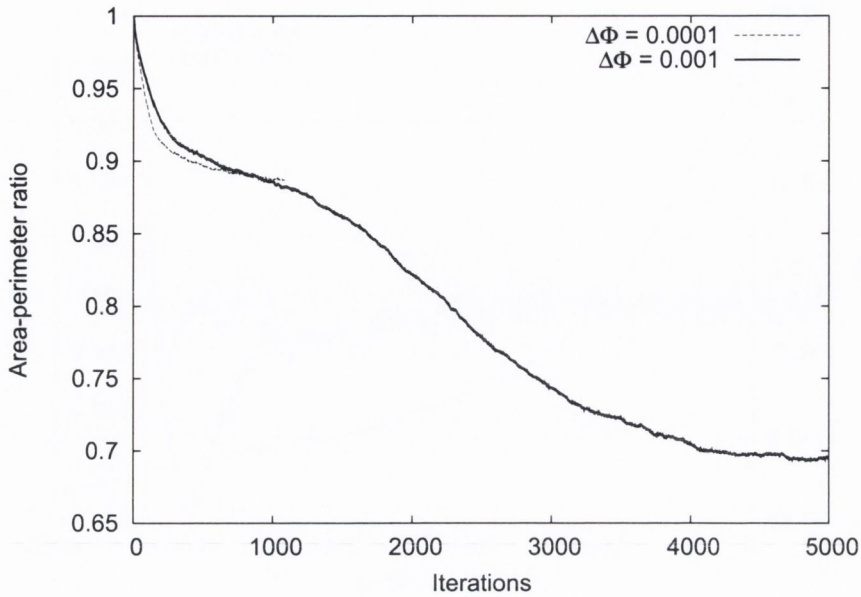


Figure 5.13: Variation of the average area-perimeter ratio f_{AP} of the grains with number of iterations for long term simulations ($\Delta\Phi = 0.001$). The data for the equivalent short term simulation ($\Delta\Phi = 0.0001$) is shown for comparison.

The variation of the area-perimeter ratio f_{AP} is shown in Figure 5.13. This shows an initial rapid decrease as the grains initially develop straight edges and deviate from their circular shape. The rate of decrease slows as the grains become irregular pentagons and hexagons. This behaviour is very similar to what was observed in the short term simulations considered in the previous section (See Figure 5.8). f_{AP} then begins to decrease faster again as the shape of the grains transitions to triangular and appears to have stabilised around a value of $f_{AP} \approx 0.69$ by iteration $i = 5000$. The maximum value of f_{AP} for a perfect triangle composed of exactly straight edges that meet exactly at points at the corners is that of an equilateral triangle with $f_{AP} \approx 0.605$. The value for our triangular shapes is higher than this as the corners are rounded and any such rounding of the shape of an object will increase its area-perimeter ratio toward 1 (the area-perimeter ratio of a circle).

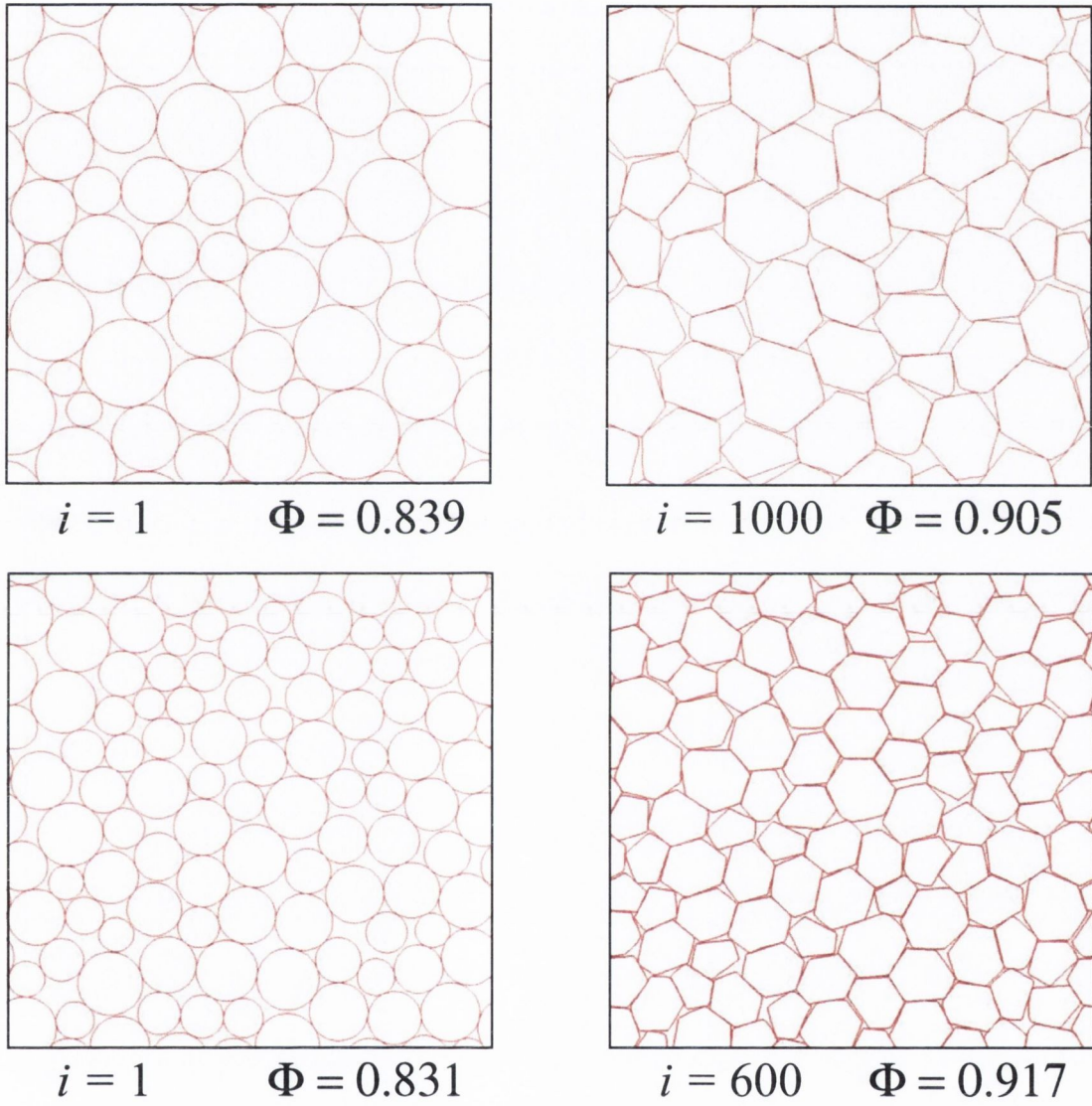
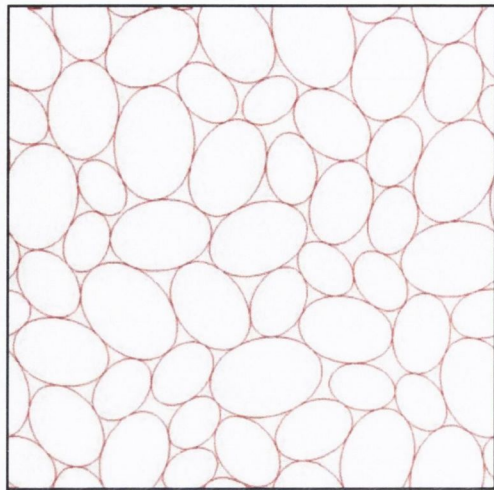
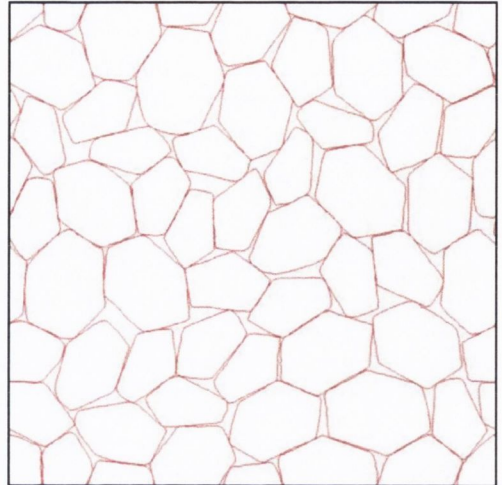


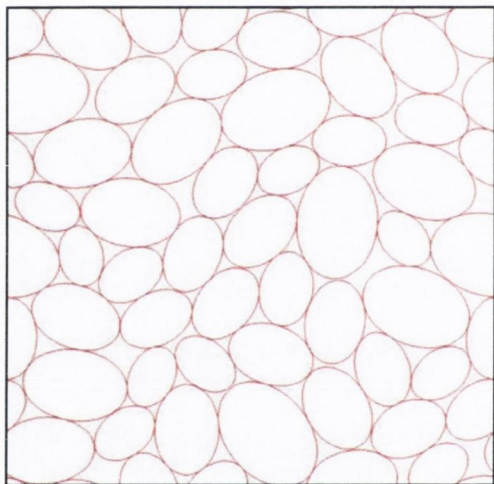
Figure 5.14: Top two images show simulation at $i = 1$ and $i = 1000$ for a system with $n = 50$ initially circular grains with radii in the range $r_{\min} = 1 \rightarrow r_{\max} = 5$. Bottom two images show simulation at $i = 1$ and $i = 600$ for a system with $n = 100$ initially circular grains with radii in the range $r_{\min} = 1 \rightarrow r_{\max} = 2$.



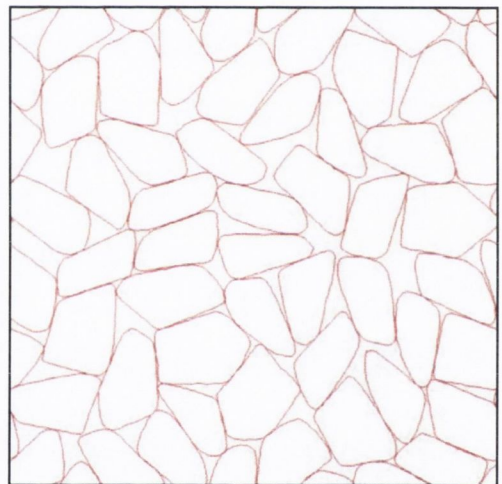
$i = 1$ $\Phi = 0.888$



$i = 1000$ $\Phi = 0.908$



$i = 1$ $\Phi = 0.874$



$i = 5000$ $\Phi = 0.848$

Figure 5.15: Short term (top two images) and long term (bottom two images) simulations with $\Delta\Phi' = 0.01$ using initially elliptical grains with aspect ratio 0.7. We see the same general behaviour as the systems initialised with circular grains. By iteration $i = 1000$ in the short term simulation the grains are shaped like irregular pentagons and hexagons. By iteration $i = 5000$ in the long term simulation the grains appear to be transitioning to a triangular shape, with the majority best described as four sided.

5.4.3 Sundry parameter variations

Here we will briefly outline the effects of varying the initial shape of the grains, the initial range of sizes of the grains and the number of grains used in the simulation. The system behaves in a very similar manner when a larger range of initial sizes of the grains is used. Simulations using initially circular grains with a range of radii $r_{\min} = 1 \rightarrow r_{\max} = 3$ (twice the range considered in the previous sections), show an identical behaviour to those considered in the previous section. Figure 5.14 shows simulation results using a range of radii for the initial circular grains of $r_{\min} = 1 \rightarrow r_{\max} = 5$ (five times the range considered in the previous sections). The grains have again by iteration $i = 1000$ largely taken on the shape of irregular pentagons and hexagons. The range of sizes of the grains also decreases as the simulation proceeds, with the standard deviation of the area decreasing from $\sigma_{area} = 0.675$ at iteration $i = 1$ to $\sigma = 0.518$ by iteration $i = 1000$.

Varying the the size of the system was found to have no effect on the qualitative results of the simulation. In Figure 5.14 the simulation performed using $N = 100$ grains has by iteration $i = 600$ reached the same state that was observed for the system with $N = 50$ in Section 5.4.1, with the grains shaped as irregular pentagons and hexagons.

To investigate the effect of varying the initial shape of the grains, a short term and a long term simulation were performed using grains that were initially elliptical in shape. The ratio of the major to the minor axes was set to 0.7, which was the ratio shown in chapter 3 to be the aspect ratio that generated the densest packings. Figure 5.15 shows the shapes of the grains for $i = 1$ and $i = 1000$ for the short term simulation ($\Delta\Phi = 0.0001$) and for $i = 1$ and $i = 5000$ for the long term simulation ($\Delta\Phi = 0.001$). The short term simulation behaves in a similar manner to the case with initially circular grains. The grains take the shape of irregular pentagons and hexagons, although at iteration $i = 1000$ they still appear somewhat elongated

due to their initial elliptical shape. The long term simulations also behave in a similar manner to those with initially circular grains. They initially form irregular pentagons and hexagons in the same manner seen for the short term simulations and by iteration $i = 5000$ the grains have clearly begun to transition to a triangular shape. However by $i = 5000$ the grains have not yet fully reached the triangular shape, in contrast to the simulation with initially circular grains where they have. The grains still do clearly appear to be transitioning in the same manner, as several of the grains have taken on a triangular shape, with the majority being best described as four sided.

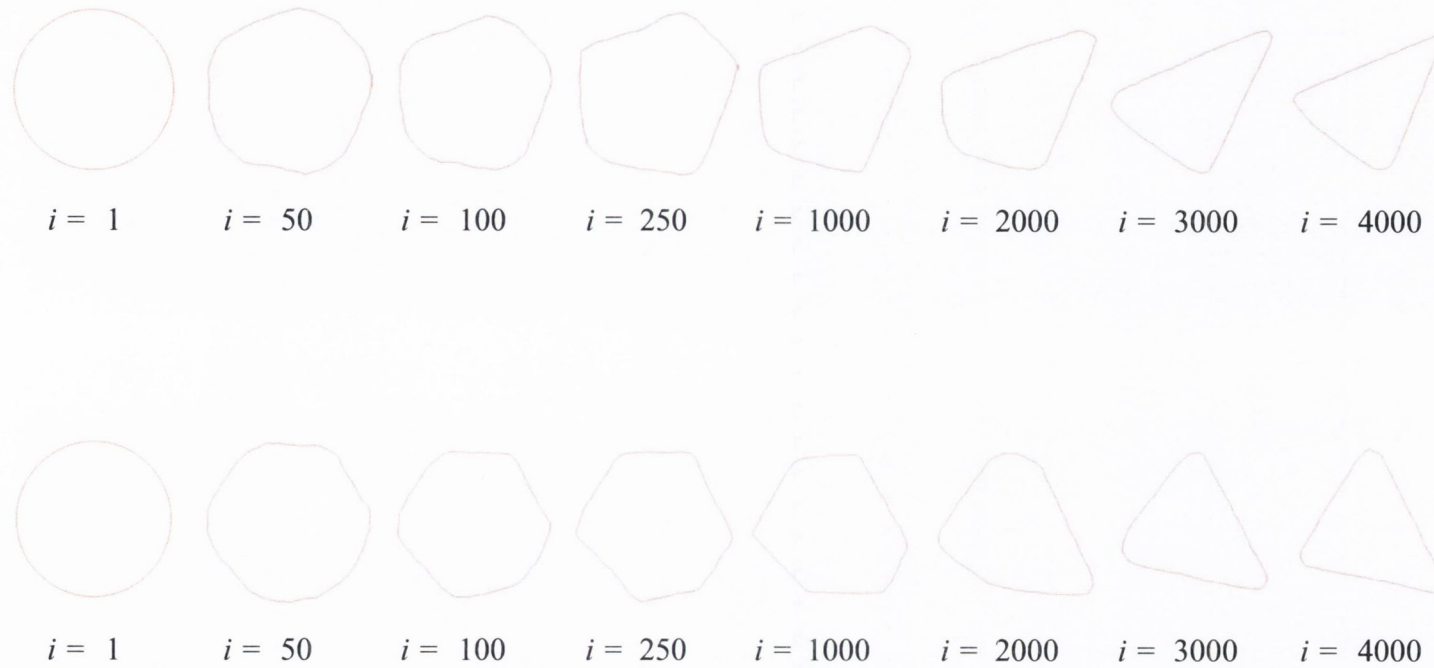


Figure 5.16: Shape evolution of two grains during the long term simulation. (Top) The grain goes through a clear pentagonal shape, before becoming triangular by iteration $i = 4000$. (Bottom) The grain goes through a clear hexagonal shape before becoming triangular by iteration $i = 4000$.

5.5 Discussion and Conclusion

Our simulation results show several key properties of the behaviour of the model:

- the areas of the grains begin to converge to a mono-disperse distribution as the simulation proceeds
- the convexity and area-perimeter ratios of the grains appear to stabilise at constant values during long term simulations
- the grains have a tendency toward angularity, forming shapes composed of irregular pentagons and hexagons during short term runs
- the grains becoming triangular in shape over long term runs

The process by which the grains form triangular shapes can be understood by considering the progression of the shape of individual grains in the long term simulation. Figure 5.16 shows how the shape of two grains vary as the simulation proceeds and the shape transitions from its initial circular shape at $i = 1$ to the triangular shape by $i = 4000$.

The pentagonal and hexagonal shapes that the grains form during the early iterations of the simulation are quite irregular and thus the internal angles that the edges form are not all equal. The more acute angles formed by the edges of the grain tend to survive as the simulation proceeds, while the obtuse angles tend to increase in value toward 180° , when the two edges forming the angle become one. This is caused by the way in which the grains tend to pack together. They generally attempt to align themselves edge against edge in an attempt to maximise the packing fraction. When an obtuse angle is formed by one longer and one shorter edge, the longer edge is more often aligned with the edge of another grain in the packing when the erosion step takes place, causing it to move inward toward the center of the grain and thus reducing the length of the shorter edge and increasing the angle between the edges.

(This can be seen happening for the top grain at iteration $i = 1000$ in Figure 5.16. By iteration $i = 2000$, the small edge and the obtuse angle have been removed from the grain.) When an angle begins to approach 180° , the grain begins to pack as if the two edges were one, slowly removing the angle until the edges are one. (This can also clearly be seen for the top grain in Figure 5.16. From iteration $i = 2000$ to $i = 3000$ the last obtuse angle is removed to give the final triangular form). The acute angles may also have a tendency to stick into the interstices between the grains in the packing, causing less of the grain to be removed at the angle during the erosion step.

The model presented here is a novel twist on traditional packing models, where the individual elements in the packing have a fixed shape. By allowing the packing itself to determine the shape evolution of the grains, we gain insights into how nonuniform abrasive forces in granular packings can effect the long-term evolution of the shape of the grains. Our simulations show a clear tendency for our grains to form straight edges, initially in the form of irregular pentagons and hexagons, transitioning to a triangular form as the simulation proceeds. This result is somewhat surprising. One could have to a first approximation envisaged a circular shape being the final result, due to the grains contacting randomly, leading to a uniform loss of the surface of the grains.

Since each iteration of the simulation may be viewed as removing a small amount of each grain so as to increase the overall packing fraction, one might have also predicted that an elliptical shape would be the result. This is the shape that is often seen for beach pebbles and has been shown to pack with a higher density for low aspect ratios in chapter 3. Indeed the model does behave in such a way as to increase the packing fraction of the grains during the early iterations, but it does this by generating pentagonal and hexagonal shapes and not elliptical ones. We see from our simulation results that acute internal angles that form in the grains are

very stable and survive as the shape of the grains evolve.

Before undertaking these simulations we had envisaged an elliptical shape as a possible outcome for the final shape of the grains, our reasoning being that each grain would be abraded less where it is most “pointed” as a result of how the grains packed together and that this would lead to an elliptical type shape, with two rounded acute angles joined by two curved lines. Indeed as already noted, objects subject to erosion in nature, such as beach pebbles, often do show a tendency toward an elliptical shape. We do find that the grains tend to become “pointed”, but form triangular shapes. This is of course the only possible 2-dimensional shape that can combine straight edges and all internally acute angles.

If we consider the shape evolution of the grains in our simulation in the context of the shapes of grains generally seen in nature, a tendency toward angularity is not generally observed in the shapes seen in nature. In three-dimensions when packings of grains are compressed within a vessel they do show a tendency to angularity, forming polyhedral shapes as they adjust their shape to fill the vessel [100]. Indeed our short term simulations do show a tendency toward space filling shapes with a large number of hexagonal grains being observed as the packing fraction rapidly increases during the early iterations. In considering the behaviour of the model, one should keep in mind the analogy between its behaviour and the behaviour of compressed packings of grains.

Returning to our example of pebbles on the beach, our results may suggest that the main forces that determine the shape evolution of the grains are not the abrasive forces that they experience when they are randomly packed together on the beach. However we must be cautious in applying the results in this way. The lowest value of our erosion parameter $\Delta\Phi' = 0.01$ that we considered is still a substantial amount of each grain to remove during the erosion step. The results for $\Delta\Phi' = 0.01$ were seen to be consistent with those using $\Delta\Phi' = 0.02$. However, further examination

of the low $\Delta\Phi'$ limit, something which was not possible for us to do in this work due to the increasing computational requirements of considering a slower erosion process, would be desirable. Given the very interesting results we have obtained, an implementation of a 3D version of this model should also be considered.

Chapter 6

The inverse packing problem - Onset of rigidity for stretched string networks

6.1 Introduction

We have defined and analysed an elementary model which has a close affinity to existing models that represent the compression of randomly packed soft spheres [42] and randomly cut elastic strings. It appears to be distinct from either of its antecedents, and not trivially related to them. It was originally conceived as a variation on the theme of soft disk and sphere packings [65, 80, 81] which we will consider in Chapter 7. That work is mainly founded on Hooke's Law interactions which act under compression only (like those considered by us in our treatment of the interaction between the spheres in a Newton's Cradle in Chapter 2) [53]. It has proved to be extremely rich in subtle phenomena, such as non-integer indices that relate contact number variations with compression. It occurred to us to simply turn this problem "inside-out", by defining Hooke's Law interactions under extension only, and hence

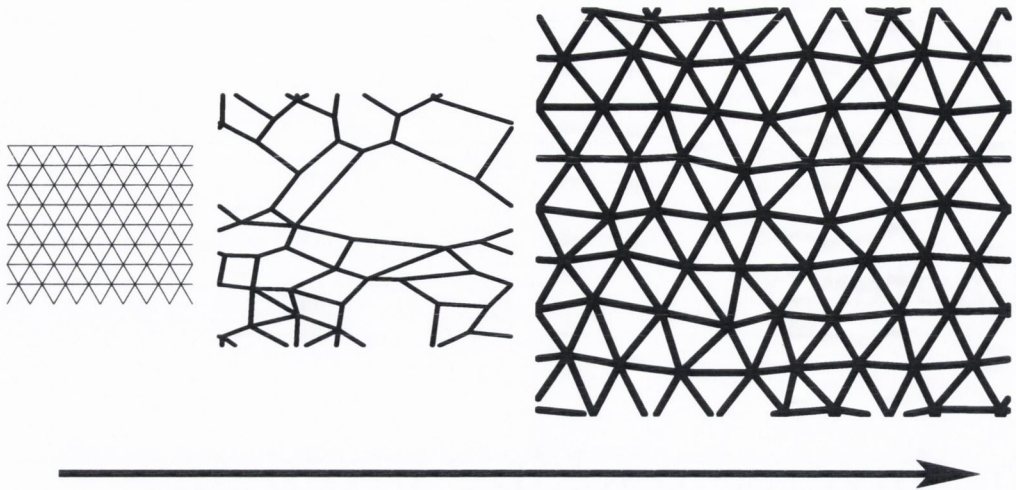


Figure 6.1: (a) Expansion of a triangular lattice with 192 strings and range $w = 2$ for the natural length of the strings. In the initial configuration of strings (left) all strings are slack and represented by thin lines between vertices. As the system is expanded, a fraction of the strings become taut. Only these taut strings are shown as thick black lines, close to the threshold expansion (middle) and for the expansion where the last spring becomes taut (right).

a model of elastic strings that are loose under compression. The strings initially connect nearest-neighbour vertices of a regular lattice and are given natural lengths l_i that are random variables. Here we will use a uniform distribution for l_i . We may ask: when and how does the resulting network become taut as its boundaries are expanded? This is analogous to the “jamming” problem of compressed hard spheres, but simpler in some respects, as we shall see.

We have simulated the above system for large numbers of vertices in two dimensions, using periodic boundary conditions. Results for different lattices are quite distinct, depending on their coordination number. Here we will consider the cases of the hexagonal, square and triangular networks, with each vertex having three, four and six neighbours respectively.

6.2 Simulation Technique

We have used the Surface Evolver software [15] to define our string network system with periodic boundary conditions and to minimise the energy of the structure with a highly optimised conjugate gradient routine. We have modified the source code to redefine the Hookean spring energy as one-sided:

$$E_i = \begin{cases} 0 & \text{if } L_i \leq l_i \\ k(L_i - l_i)^2 & \text{if } L_i > l_i \end{cases} \quad (6.1)$$

where L_i is the separation of the two vertices at the ends of the string i and l_i is the natural length of each of the N strings. For $L_i < l_i$ a string is slack.

We define a string network, consisting of strings and vertices (a string is formed by joining two vertices) in a two-dimensional box with periodic boundary conditions. The lattice is initially defined with all nearest neighbour separations equal to unity. The natural lengths l_i of the corresponding N elastic strings are uniformly distributed in the range

$$1 \leq l_i \leq l_{max}. \quad (6.2)$$

The width of the distribution of random numbers is thus given by $w = l_{max} - 1$. The system is uniformly expanded by a small amount using an affine transformation. The structure is then relaxed to minimise the total energy. This procedure of small expansion followed by relaxation is continued until all strings have become taut (Figure 6.2). A fraction of the strings first become taut at some previous point, which we may call the threshold of rigidity.

In considering the basic properties of the model, we recognise some of its simplifying features. In contrast to the soft-sphere problem, this stretched string model has the property of *convexity*, as does the line minimisation problem [41]. Convexity is defined (in this case) as follows. At every point in the space of vertex coordinates,

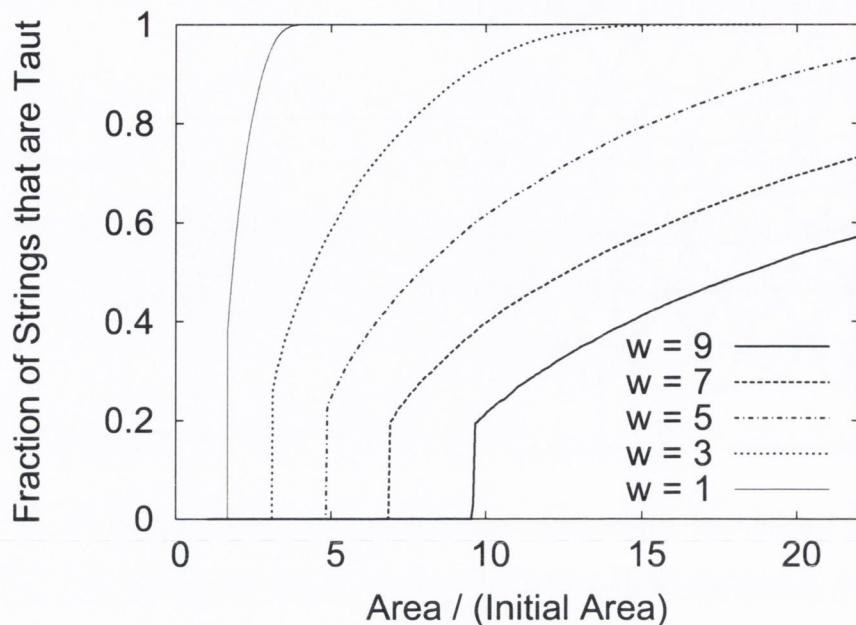


Figure 6.2: Increase in the number of taut strings as the periodic box is expanded, for a triangular lattice with 49152 strings. Data is shown for five different ranges of random natural lengths of the strings $w = 1$, $w = 3$, $w = 5$, $w = 7$ and $w = 9$.

the second derivative of energy with respect to displacement is non-negative for all directions. This follows easily from the same statement applied to the energy term associated with each string.

Convexity implies that there cannot be more than one disjoint minimum of energy at and above the threshold expansion. (A sketch of a simple curve with two minima makes this obvious.) Unlike many of its disordered cousins, the model has a unique global minimum of energy. Thus any stable state reached in our minimisation of the system is the *unique* solution for the string network. This reinforces the point made earlier, to the effect that turning the soft-sphere model inside-out entails quite different properties, since the soft-sphere model has a multiplicity of alternative minima.

We will now present results for very large systems with $N = 32178$ for the square

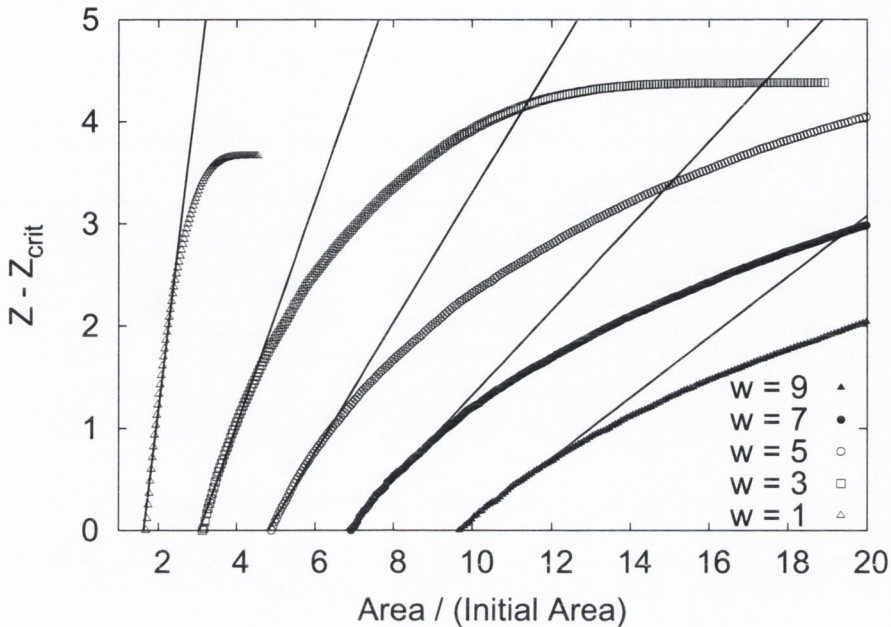


Figure 6.3: Triangular lattice (49152 strings) above the threshold of rigidity. As the network is expanded, the average coordination number Z increases linearly close to its threshold value, Z_{crit} (the data shown is for five different ranges w of random natural lengths of strings, the lines are linear least squares fits to the data close to the threshold).

case and $N = 49152$ for the triangular and hexagonal case. We find the same system behaviour when we consider systems with smaller numbers of strings.

6.3 Simulation results for the triangular lattice

For the ordered case ($w = 0$), it is obvious that expanding the boundaries simply results in an affine expansion of the lattice, all strings becoming equally taut immediately. However, even quite small values of w produce radically different initial behaviour upon expansion. In such a case, at a certain critical expansion the system becomes taut, with an average coordination number Z_{crit} (average number of taut strings connected to a vertex), which we shall examine.

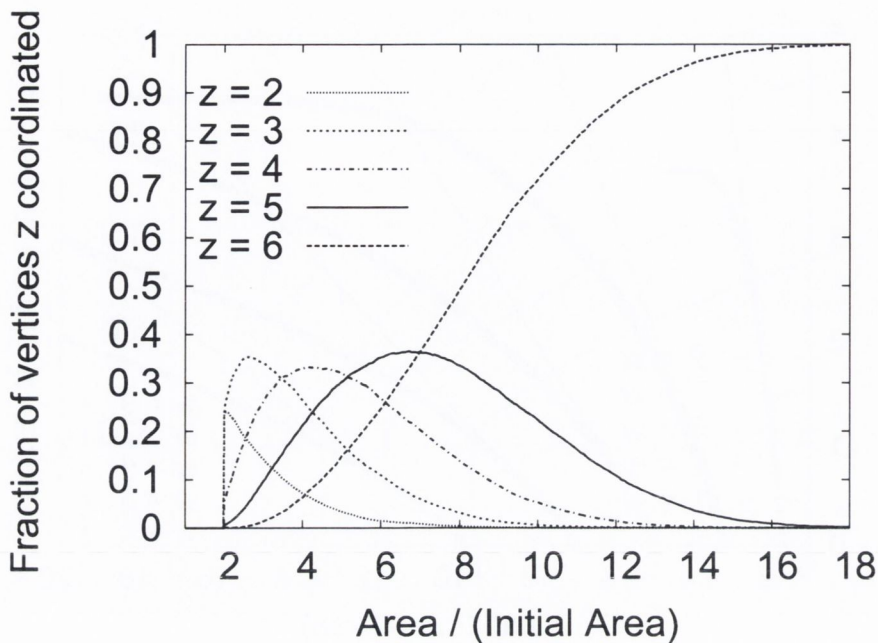


Figure 6.4: Variation in the fraction of vertices with coordination numbers $z = 2$ to $z = 6$ as the network is expanded (here $w = 4$).

As the boundaries are further expanded beyond this point, the average coordination number Z increases. It is obvious that for a finite-width distribution of l_i , Z should tend to *six* (all strings taut) as the expansion tends to infinity; indeed it is clear that this should occur at some finite expansion. Its initial variation beyond the critical expansion is less obvious; at what rate do the loose strings become taut? We find this variation to be linear for the triangular case (Figure 6.3). This is a very different behaviour from the strong nonlinear effects for disk and sphere packings under compression, as represented by compressed springs. In that case a power law variation with exponent 0.5 is found for the variation of the excess contacts with packing fraction above the jamming threshold [81].

An individual vertex can have a coordination number z of taut connections between $z = 2$ and $z = 6$. Figure 6.4 shows the variation in the fraction of vertices with each coordination number as the system is expanded. At the threshold expansion the coordination number of some of the vertices jumps up from zero. Initially there

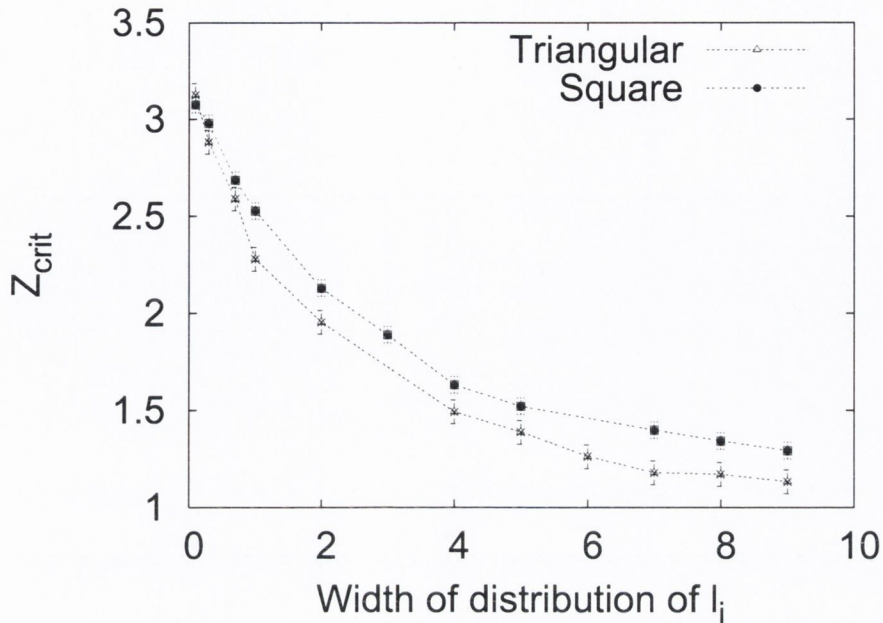


Figure 6.5: Variation of the average coordination number Z_{crit} at the threshold of rigidity as a function of the width w of the distribution of random natural lengths l_i .

is a large number of vertices with coordination $z = 2$ (24.3% for the case with $w = 4$ shown in Figure 6.4). This decreases steadily as the system is expanded and more strings become a part of the taut network. We see a similar decrease for $z = 3$. Coordination numbers $z = 4$ and $z = 5$ show an initial increase and then decrease for larger expansions as the system approaches the fully taut state where all vertices have $z = 6$.

Figure 6.5 shows the variation of the average coordination number (Z_{crit}) at the threshold expansion with the range of the natural string lengths w . The steep initial descent of Z_{crit} makes it difficult to extrapolate reliably for $w \rightarrow 0$. It is consistent with a finite value less than 6. There also appears to be a monotonic decrease of Z_{crit} as w tends to infinity.

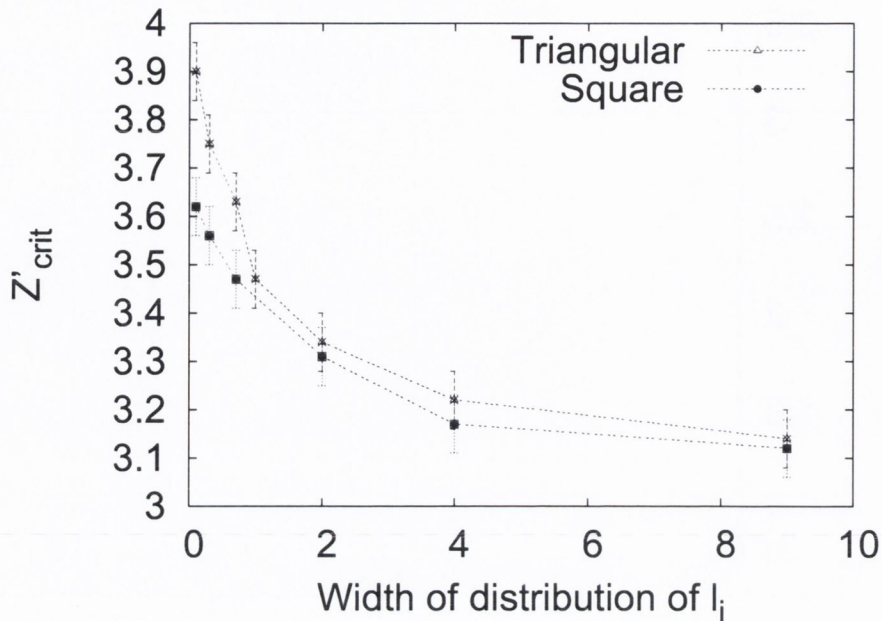


Figure 6.6: Disregarding vertices with coordination $z \leq 2$ leads to a value of Z'_{crit} which in the limit of $w \rightarrow 0$ is much closer to four, which is the prediction of constraint theory. (The data shown is for a square lattice with 32768 strings and a triangular lattice with 49152 strings.)

6.4 Interpretation

The first key to understanding these results is surely constraint theory, a venerable mathematical technique with important modern applications in areas such as protein flexibility [94] and the random packing of particles [29]. It seeks to identify constraints and degrees of freedom, and equates these to make estimates of the statistics of critical points of the general kind that we have encountered here. In the triangular case, each vertex has the two degrees of freedom of translation and each taut string, maintained at its natural length l_i , will contribute one constraint which is $L = l_i$. The expectation is therefore that, in the absence of any symmetry (such as that which one obtains when $l_{max} = 1$), the degrees of freedom are exhausted when the average coordination $Z = 4$, since each string joins two vertices. However

we see that the estimate from constraint theory appears not to be at all accurate even for small values of w (the range of natural lengths). For $w = 0.1$, the average coordination at the threshold is $Z_{crit} = 3.12 \pm 0.06$. For larger values of w there is a strong decrease of Z_{crit} , which appears to level off for large values of w .

We see that even for $w \rightarrow 0$, the naive estimate from constraint theory ($Z_{crit} = 4$) is not found, and the discrepancy grows rapidly with w . The reason for this lies largely in the symmetry of the initial state. It can happen that a vertex is connected to only two taut strings, in which case it should be considered redundant in any constraint arguments, and the two strings considered as one. (This is obvious as taut strings that join vertices with coordination $z = 2$ must lie collinear and in effect behave as a single string.) We can also disregard all vertices that are only connected to slack strings ($z = 0$), as these do not contribute to the taut network. With these refinements and thus a definition of an average coordination number Z' which does not take into account vertices with $z \leq 2$, the constraints argument does succeed in the low w limit, as Figure 6.6 shows. We find that $Z'_{crit} = 3.9 \pm 0.06$ for $w = 0.1$. This correction however does not suffice to explain the additional decrease of Z_{crit} at high w .

6.5 Results for the square lattice

A square lattice is set up with each vertex connected to its four nearest neighbours. An example of a simulation using a square lattice is shown in Figure 6.7. This is an interesting lattice configuration, as it has the same number of nearest neighbour connections as the number of constraints predicted to be required for the system to become taut. Nevertheless the system behaves in a somewhat similar manner to the triangular case. As the system is expanded, a threshold expansion is reached where a fraction of the strings become taut. As the system is further expanded there is an

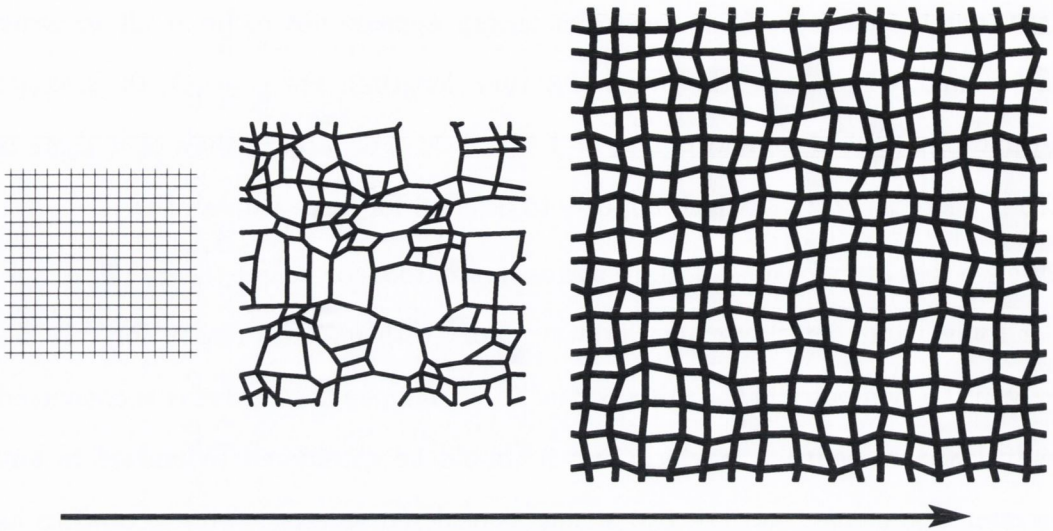


Figure 6.7: Expansion of a square lattice. Simulation output for 512 strings and $w = 2$, displayed as in Figure 6.1.

initial linear increase in the fraction of strings that are taut.

For a square lattice, a constrained vertex can have a coordination number between $z = 2$ and $z = 4$. Figure 6.8 shows the variation in the fraction of vertices with each coordination number as the system is expanded. At the threshold expansion, the first strings become taut and so the coordination of some of the vertices jumps up from zero. We see again that a large fraction of vertices have coordination $z = 2$ (28.5% for the case with $w = 4$ shown in Figure 6.8). This decreases steadily as the system is expanded and more strings become part of the taut network. The fraction of vertices with $z = 3$ shows an initial increase and then decrease for larger expansions, a similar behaviour as for $z = 4$ and $z = 5$ for the triangular lattice. Finally as the system approaches the fully taut state all vertices tend to $z = 4$.

The variation of coordination number (Z_{crit}) at the threshold expansion with the distribution of natural lengths w is shown in Figure 6.5. Here again we see a steep initial descent of Z_{crit} which makes it difficult to extrapolate reliably the limit $w \rightarrow 0$. It is consistent with a finite value less than 4. There also appears again to

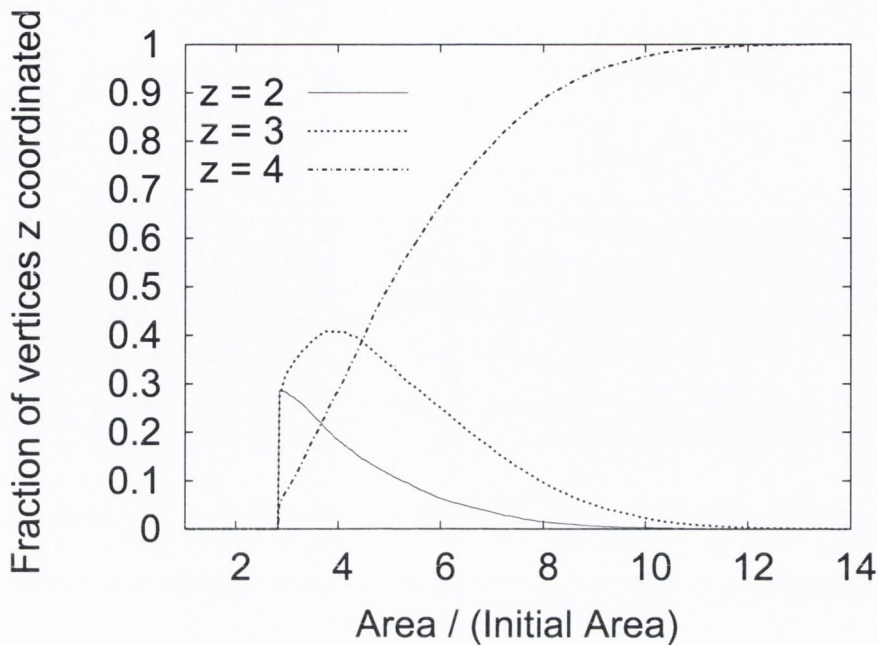


Figure 6.8: Expansion of a square lattice. Variation in the fraction of vertices with coordination numbers $z = 2$ to $z = 6$ as the system is expanded (data shown is for a square lattice composed of 32768 strings and $w = 4$).

be a monotonic decrease of Z_{crit} as w tends to infinity, similar to what is seen in the triangular case.

It is clear from Figure 6.7 (and from the large number of vertices with coordination $z = 2$ in 6.8) that even at the threshold expansion we again have substantial pockets of loose strings. When we calculate the coordination number of the taut network (Z'_{crit}) as for the triangular case, we again find that in the low w limit results are brought towards the predictions of constraint theory with $Z'_{crit} = 3.62 \pm 0.04$ for $w = 0.1$, but not as closely as in the triangular case.

6.6 Results for the hexagonal lattice

A hexagonal lattice is set up with each vertex connected to its three nearest neighbours. An example of a simulation using a hexagonal lattice is shown in Figure 6.9.

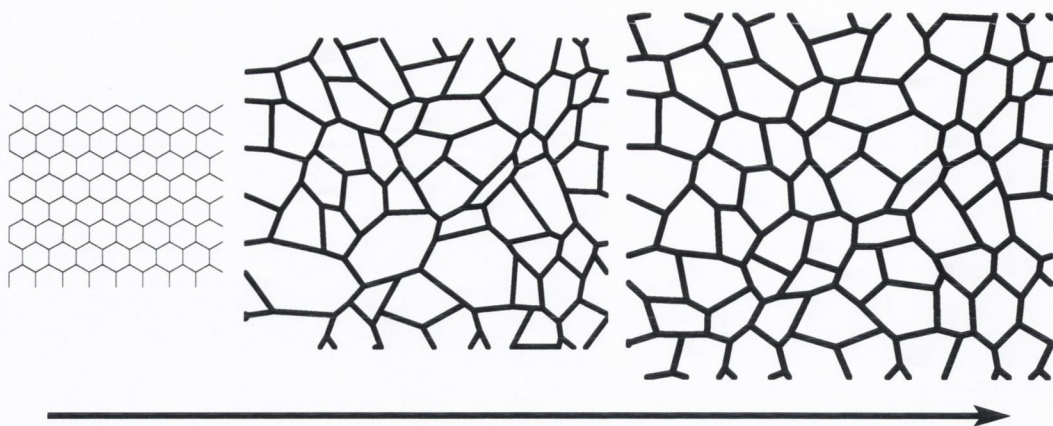


Figure 6.9: Expansion of a hexagonal lattice. Simulation output for 192 strings and $w = 2$, displayed as in Figure 6.1.

This lattice configuration has one fewer nearest neighbour connections than the predicted number of constraints required for the system to become taut. We would thus expect that as the system is expanded, a threshold will be reached where all strings would become taut simultaneously and that this behaviour would be independent of the width of the distribution of random lengths w .

We see in Figure 6.10 that the system behaves in the expected manner only in the low w limit. As w is increased, the average coordination Z_{crit} at the threshold decreases as for the triangular and square lattices. The coordination number of the taut network (Z'_{crit}) formed at the threshold is indicated by the dashed line on Figure 6.10. This must always be $Z'_{crit} = 3$ as by definition disregarding vertices with $z \leq 2$ in a system where the maximum coordination number is 3, must only leave the vertices with coordination $z = 3$.

6.7 Conclusion

A network of elastic strings of random lengths under tension has been seen here to behave in a very different way to the case of elastic disk and sphere packings under compression. In particular there is a global minimum of energy above threshold.

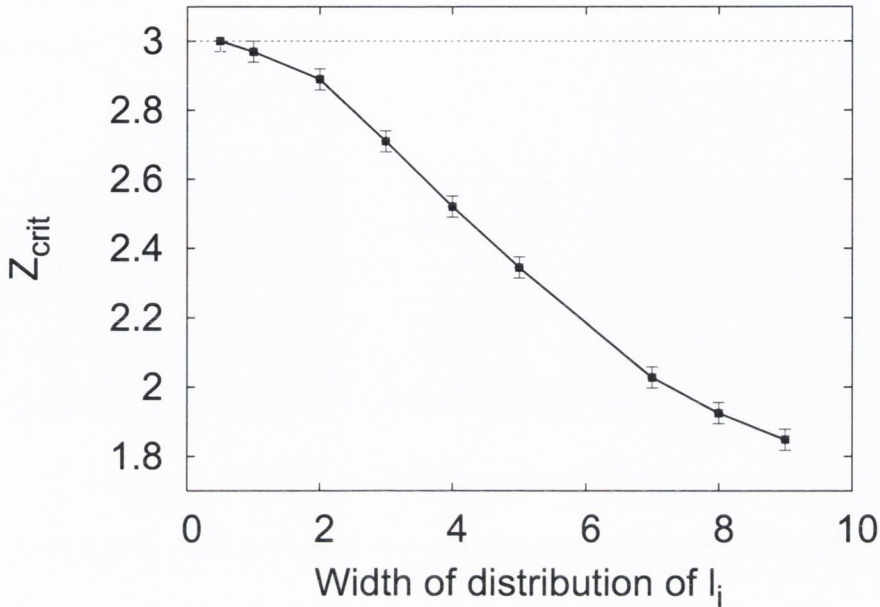


Figure 6.10: Expansion of a hexagonal lattice. Variation of the average coordination number Z_{crit} at the threshold of rigidity as a function of the width w of the distribution of random natural lengths l_i (data shown is for a hexagonal lattice with 49152 strings). As the maximum coordination is 3, disregarding all vertices with coordination $z \leq 2$ gives a constant value of $Z'_{crit} = 3$, indicated by the dashed line.

There is a strong dependence of the behaviour of the system, and in particular the critical average coordination number, on the polydispersity (represented by the distribution of natural lengths of the strings). The naive application of constraint theory requires various corrections to explain these results.

There are also instances of the failure of constraint theory for packings of objects in two and three dimensions. Packings may for example contain “rattlers”, objects that can move freely in the interstices of a rigid system of larger scale. A naive application of constraint theory also runs into difficulty in the case of objects that have an asymmetric shape [29, 33] and was have seen in Chapter 3 where we considered packings of elliptical grains.

In future extensions to this work further insights into the behaviour of the system could be got from dealing with other lattices and other significant variables that characterise their behaviour. Of particular interest are the elastic properties of the network [111] and a statistical analysis of the pockets of loose strings. A project student with our group (Edmond Daly), has used our implementation of the model to perform a preliminary examination of these properties of the system and they will be the subject of future investigations. Since the model corresponds closely to an experimental system that can be directly realised, the construction of an experimental system could also be considered.

Chapter 7

3D sphere packings and bubbles in the wet foam limit

7.1 Introduction

As was discussed in Chapter 1, theoretical and computational models based on interacting spheres in 3D (and interacting circles in 2D) have been widely used to study the packing properties of granular materials [80]. When bubbles are packed together in a very wet foam, their shapes are very close to spherical and it can indeed be useful to consider their interactions in terms of interacting spheres. Durian has applied this technique to the study of 2D wet foams [42, 43].

Here we will consider three-dimensional sphere packings generated using an adaptation of the technique we used to model Newton's Cradle in Chapter 2. This work was inspired as a means of generating simulated sphere packings which could be compared to experimentally produced wet bubble packings which our research group have recently investigated. We have observed a surprising degree of ordering in a wet foam composed of small bubbles of diameter $200\mu\text{m}$ [99]. Similar observations were made by Bragg and Nye in 1947, but their work on three-dimensional wet bubble

packings appear to have never been followed up [61].

While it is extremely difficult to make an ordered dry foam composed of polyhedral cells [104], these bubble packings in the wet foam limit have been found to readily order as shown in Figures 7.1 and 7.2. Examination of the top three surface layers and the terraces formed by the bubbles at the bottom of the foam appear to suggest the order propagates through the entire sample which can be up to 15 layers deep. Random sampling of the structures seen in the top 3 layers suggest a ratio of 2:1 fcc (ABC) over hcp (ABA) occurring in the packings. Examination of up to 6 layers in the terraces formed by the packing of the bubbles at the bottom of the foam also shows a preference for fcc with random sampling finding 58% fcc, 15% hcp and 27% rhcp [98]. Large regions of square packed layers corresponding to fcc (100) have also been observed in both the surface of the foam and the terraces underneath (See Figure 7.1). Various crystal defect structures have also been observed, similar to those found in opals [64, 87].

In this work we have carried out simple simulations utilising soft sphere molecular dynamics (like those used in Chapter 2 to model Newton's Cradle). We have also implemented a 3D version of our random packing algorithm (used in Chapters 3 and 5) and used it to generate random sphere packings. In performing these simulations we wished to identify what similarities existed between the behaviour of a simple model based on interacting spheres and the behavior of the wet foam system. As the bubbles that make up the surface layer of the wet foam can order easily into a triangular packed arrangement, we wished to investigate the contribution that this order in the top layer could make to the ordering of layers of bubbles that would form underneath it. Also, as large regions of surface bubbles packed in a square fcc (100) arrangement have been observed, we have also investigated the contribution that a square packed surface layer would have.

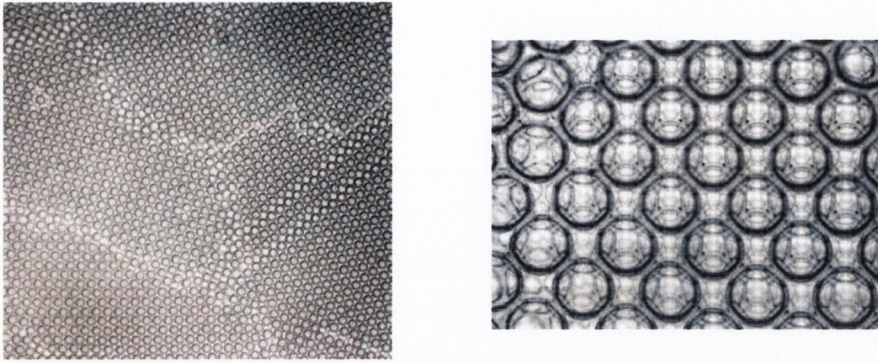


Figure 7.1: (Left) Large surface triangular packing of bubbles. (Right) Close up of a section of bubbles arranged in an fcc packing in the direction (100). It can be determined from optical effects in the surface bubbles that the packings are ordered at least 3 layers deep (Left) and 5 layers deep (Right) [99]. *Pictures courtesy of Antje van der Net.*



Figure 7.2: Ordered terraces at the bottom of the packing of bubbles. This seems to suggest that the order propagates throughout the sample [99]. *Picture courtesy of Antje van der Net.*

7.2 Bubbles in the Wet Foam Limit

In general when a foam is created, the water contained within it drains out under the force of gravity, leaving a relatively dry foam [104]. However, it is possible to make very wet foams, by reducing the size of the bubbles used. A foam consisting of very small bubbles does not expel liquid to the same extent as one composed of larger bubbles. It remains very wet and composed of spherical bubbles up to a height h above the underlying liquid surface given by

$$h \simeq \frac{l_o^2}{d}. \quad (7.1)$$

Here l_o is the capillary length,

$$l_o^2 = \frac{\gamma}{\rho g}, \quad (7.2)$$

d is the bubble diameter, γ is the surface tension, ρ is the density of the liquid and g is the acceleration due to gravity [104]. An estimate of the number of layers N_{layers} of bubbles that can be contained in this wet section of foam of width d can be made from Eqn. 7.1 and Eqn. 7.2:

$$N \simeq \left(\frac{l_o}{d} \right)^2 \quad (7.3)$$

We can therefore make a large sample of wet foam, composed of spherical bubbles, provided $d \ll l_o$. For the surfactants generally used in foam generation l_o is of the order of 1mm, requiring bubbles with diameter of only a fraction of millimeter to be used to generate a large foam of sufficient wetness.

Members of our research group have used microfluidic flow focusing to produce a rapid stream of small bubbles of equal size [99]. Using this method it is possible to create bubbles with diameters from 100 to 500 μm , and use them to create very wet foams containing over 25 layers of bubbles (See Figures 7.1 and 7.2).

We will now present simulation results of sphere packings using both a 3D version of our random packing algorithm used in Chapters 3 and 5 and a full dynamical soft sphere model like that used in Chapter 2. We will then compare and contrast these with the order seen in the experimentally generated wet bubble packings. Both the 3D monte-carlo type sphere packing model and the dynamic 3D sphere packing models we will now present have been implemented in a 3D extension to our `ARBITRARYPACKER` software.

7.3 Random Sphere Packing

We have implemented a 3D spheres version of our monte-carlo type random packing algorithm used in Chapters 3 and 5. Figure 1.2 in Chapter 1 shows a random packing of 500 spheres generated using this algorithm with periodic boundary conditions in all three directions. This packing was generated in the same manner as the random packings in Chapters 3 and 5. Small spheres were initially placed at random positions in the periodic box. At each iteration of the simulation the packing fraction was increased by $\Delta\Phi = 0.0001$ by increasing the size of all of the spheres. The energy (total overlap) of the spheres was then minimised to zero in the same way as for the 2D simulations, with every sphere which has a non-zero energy attempting to make a random movement to a new position where it has a lower energy, while every sphere that already has a zero energy attempts to make a random movement to a new location where it also has zero energy. This algorithm creates random packings with packing fraction $\Phi = 0.63 \pm 0.01$, which is consistent with the random closed packed density of spheres ($\Phi \approx 0.64$) [12, 13].

This is the packing fraction that one might expect to see for our packings of small bubbles in the wet foam limit. However those packings appear to order and

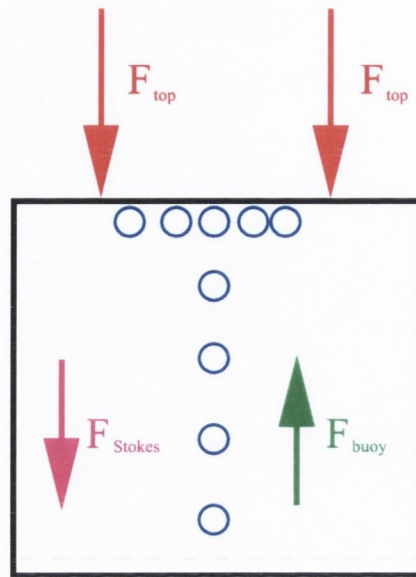


Figure 7.3: Forces on spheres in the dynamics simulation. The spheres rise up due to F_{buoy} until they reach the top of the simulation cell where they are stopped by F_{top} . The velocity of the spheres is constantly reduced by F_{Stokes} .

thus achieve a much higher packing fraction. One key difference between the bubble packings and the random packing shown in Figures 7.1 and 7.2 is the behaviour of the surface layer of bubbles. When a 2D monodisperse packing of bubbles is generated, it readily forms an ordered triangular packing. Thus if we are generating bubbles underneath the liquid and allowing them to rise up, the top surface layer will readily order in a triangular packing. This may act to assist the ordering of the subsequent layers of bubbles that form underneath it. As our random packing algorithm is solely designed to generate random packings, we will examine these potential ordering effects using our dynamic sphere packing model.

7.4 Dynamic sphere packing model

The forces governing the interaction of the spheres in the model considered here are the same as those we considered for our simulation of Newton's cradle in Chapter

2. The force between two overlapping spheres each with radius r and positioned a distance d apart is given by:

$$F = k(2r - d)_+^\alpha. \quad (7.4)$$

The notation $()_+$ specifies that the value of the bracket is zero if the expression inside is negative, as required for the representation of contact forces that cannot be in tension. The exponent α is $3/2$ for spheres (Hertzian Law).

A schematic drawing of the forces on the spheres in the simulation box is given in Figure 7.3. We consider the spheres moving in a viscous liquid and again utilise a simple linear Stoke's Law to model the velocity-dependent viscous force

$$F_{\text{Stokes}} = -\eta v. \quad (7.5)$$

As in the simulations of Newton's Cradle we also again implemented a viscoelastic dissipation force in the collisions of the spheres of the form

$$F_{\text{diss}} = -\gamma \frac{d}{dt}(\xi^\beta), \quad (7.6)$$

where $\xi = 2r - d$ is the overlap between two spheres and $\beta = 3/2$ (Hertz-Kuwabara-Konomodel) [110].

We model the spheres rising due to a buoyancy force F_{buoy} , which is a constant force that acts upwards in the z direction. To stop the spheres from leaving the top of the simulation box, the spheres experience a strong spring force $F_{\text{top}} = (k_{\text{top}}\Delta z)_+$, where Δz is the vertical distance the sphere has traveled above the top of the box.

The dynamic model has been implemented using both the velocity Verlet algorithm and the Euler-Richardson method (Details of these algorithms are given in Section 2 2.2 and 2.5). As we will consider dissipation forces which are velocity dependent, it is most appropriate to use the Euler-Richardson method in the results presented here. It is possible to use the velocity Verlet algorithm for systems with velocity dependent forces, so long as one recognises that an additional numerical

error will be introduced from determining the viscous force using the velocity from the previous time step. This method has also been used to test our simulation and seen to give identical results to our implementation using the Euler-Richardson algorithm.

7.5 Simulation Results

In the simulations presented here we have fixed the following simulation parameters $k = 10000$, $F_{\text{buoy}} = 1$, $k_{\text{top}} = 10000$, $m = 1$ (mass of the spheres) and $R = 0.1$ (radius of the spheres). A value of $k = 10000$ is sufficient to ensure that there is very small sphere overlaps during the course of the simulation and we have tested using a value ten times larger and found the system to demonstrate the same general behaviour. $k_{\text{top}} = 10000$ is sufficiently large to hold the surface spheres in place and using a larger value also does not change the system behaviour. All simulation results presented here use periodic boundary conditions in the x and y directions.

7.5.1 Formation of a surface layer

Figure 7.4 shows how a surface layer forms when we release new spheres into an empty simulation box at the center of the x-y plane at the bottom of the simulation box. The necessary boundary conditions are used to fit a fully triangular packed layer of 192 spheres. In this simulation we have set $\gamma = 0$ and $\eta = 10$. This puts us in the limit of spheres colliding elastically in a highly viscous liquid. Most of the top layer of spheres orders into a triangular packing, but there is some disorder as the layer of spheres is unable to make the final global rearrangements necessary to fit a fully ordered triangular layer. This disorder on the top layer will vary greatly from one simulation run to another. It is possible that by chance the top layer will order into a perfect triangular layer, but in general there will be some disorder. This

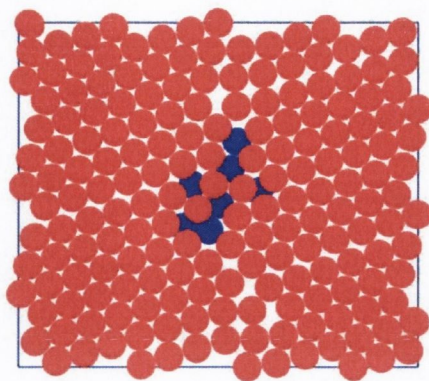


Figure 7.4: Formation of the surface layer. Surface spheres are shown in red. The first seven spheres forming the second layer are shown in blue. The boundary conditions are such that an arrangement of the spheres in a fully ordered triangular layer is possible. The majority of the surface layer packs in a triangular arrangement but a fully triangular layer does not form.

disorder will greatly affect the layers that form underneath the top layer. Thus to study how an ordered hexagonal top layer will affect the subsequent layers, we will begin our simulation with a fixed hexagonal top layer. We will return to this issue of the formation of the surface layer in Section 7.5.4.

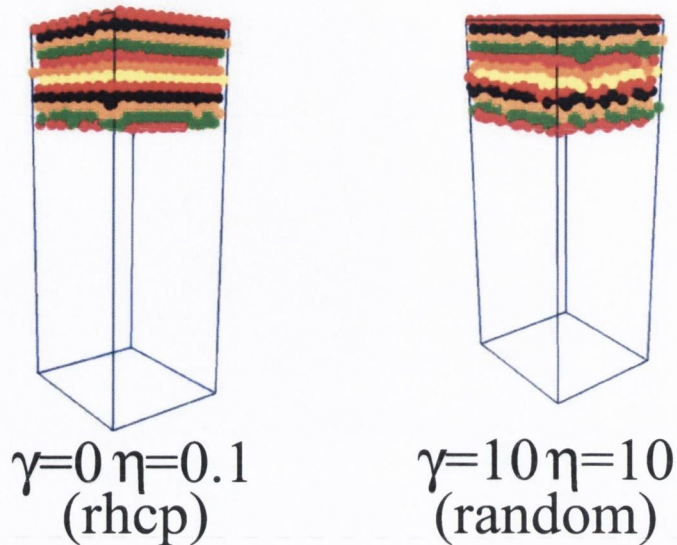


Figure 7.5: Packings generated by initially creating 2000 spheres at random locations in the simulations box and allowing them to settle on a fixed triangular packed top layer. (Left) Simulation with low dissipation. The spheres are allowed to slowly come to rest in a random hexagonal close packed (rhcp) configuration. (Right) Simulation with high dissipation. The spheres rapidly come to rest in a random packing.

7.5.2 Deposition of spheres onto a triangular packing

Firstly we will consider packings generated by initially creating 2000 spheres at random locations in the simulations box and allowing them to settle on a fixed triangular packed top layer composed of 192 spheres. We have simulated this in both a high dissipation regime with $\gamma = 10$ and $\eta = 10$ and a very low dissipation regime with elastic collisions ($\gamma = 0$) and $\eta = 0.1$. Figure 7.5 shows the resulting packings generated. We see that for the packing generated in the high dissipation regime the system rapidly comes to rest with the spheres in a highly disordered configuration. However the system in the very low dissipation regime forms an rhcp packing with very few defects. This is due to the spheres velocities slowly being

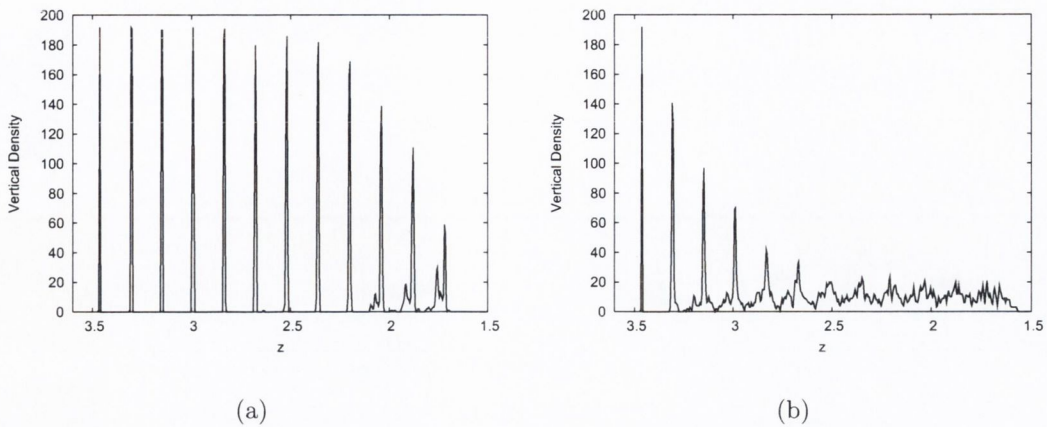


Figure 7.6: Vertical density variation for sphere packings onto a triangular packed layer shown in Figure 7.5. (a) Low dissipation $\gamma = 0$ and $\eta = 0.1$. (b) High dissipation $\gamma = 10$ and $\eta = 10$. Note the sharp high peaks in (a) indicating the high degree of vertical order in this rhcp packing. The rapid reduction in the height and sharpness of the peaks in (b) indicates the loss of vertical order in the packing.

reduced by the viscous dissipation, allowing the system to slowly order in a similar manner to a slow cooling or annealing of the system. The clear difference in the order between the two packings can be seen if we examine the variation in the vertical density of the packings. Figures 7.6(a) and 7.6(b) have been calculated by counting the number of sphere centers in vertical sections of the simulation box $\Delta h = 0.1R$ wide. Sharpe peaks in the graph indicate ordered layers. We can see that Figure 7.6(a) contains more than seven ordered layers, while there is little vertical order in the packing in Figure 7.6(b).

We will now consider packings generated by releasing spheres one at a time from the center of the bottom of the simulation box. Figure 7.7 shows packings generated in this way. The first packing was generated using parameter values of $\eta = 1$ and $\gamma = 1$. Here we see that there is a high degree of order in the packing. We observe an overall rhcp type packing, with a large number of dislocations between regions

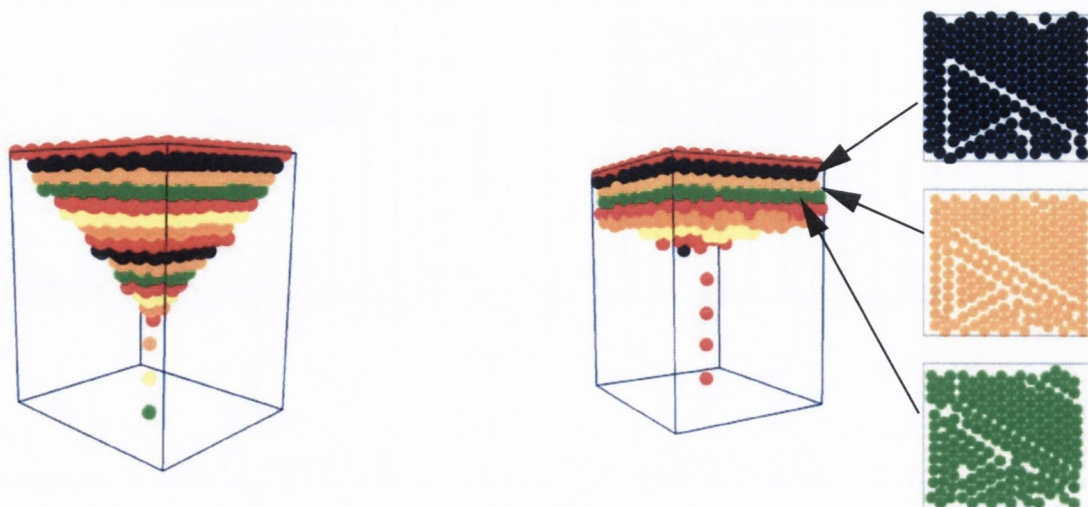


Figure 7.7: Packing onto a fixed triangular packed surface layer, with spheres released one at a time from the bottom of the simulation box. (Left) fcc packing generated with $\eta = 10$ and $\gamma = 10$. (Right) an ordered packing generated with $\eta = 1$.

of spheres in the packing. The second packing was generated in the limit of very high dissipation with $\eta = 10$ and $\gamma = 10$. We see a high degree of ordering in this limit and providing the initial spheres arrange themselves correctly, the system can generate a large number of perfect fcc layers as shown in Figure 7.7.

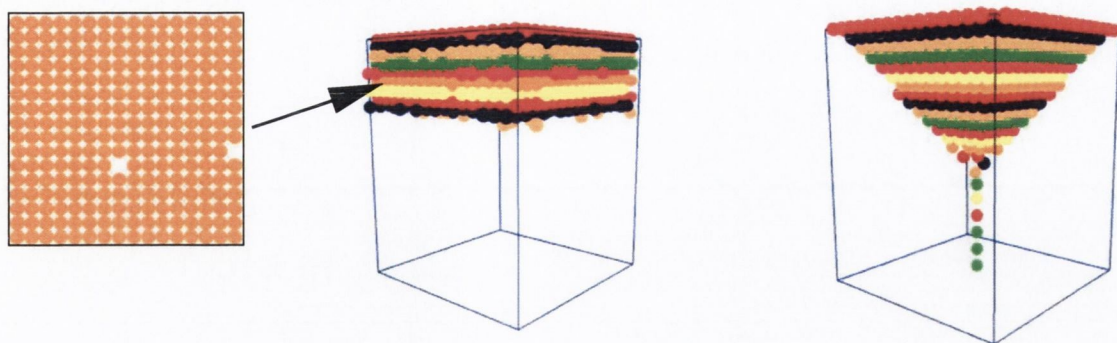


Figure 7.8: Packings generated by allowing spheres to settle on a fixed square packed layer with $\gamma = 10$ and $\eta = 10$. (Left) 2000 spheres are released simultaneously at random locations in the simulation box and allowed to settle. Despite being in a high dissipation regime, ordered square packed layers form giving an fcc packing. We observe a small number of point dislocations in the ordered layers of sphere as shown. (Right) An fcc packing is formed by releasing spheres one at a time from the middle of the bottom of the simulation box.

7.5.3 Deposition of spheres onto a square packing

In the experimental wet foam system a large amount of ordered fcc (100) crystal structure is observed (See Figure 7.1). To investigate how the square packed layers of this structure influence the packing of layers of spheres that form underneath it, we simulated the deposition of spheres onto a square packed layer. Figure 7.8 shows packings generated by allowing spheres to settle on a fixed square packed layer with $\gamma = 10$ and $\eta = 10$. The first packing was generated by initially creating 2000 spheres at random locations in the simulation box and allowing them to settle. Despite being in a high dissipation regime, ordered square packed layers formed giving an fcc packing. We observe a small number of point dislocations in the ordered layers of spheres as shown in Figure 7.8. This behaviour is very different to the same simulation run with a triangular surface packed layer as shown in Figure 7.5. There we observed very little order in the resulting packing in comparison to an

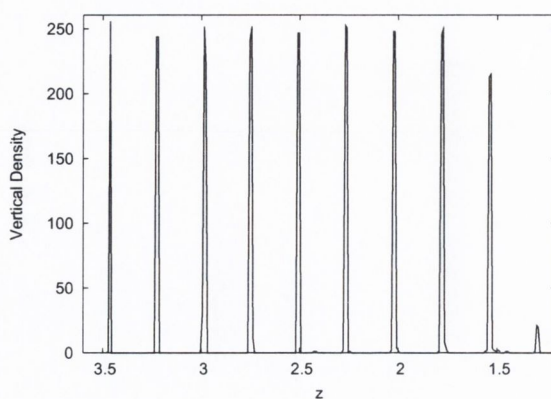


Figure 7.9: Vertical density variation for the sphere packing (shown in Figure 7.8) generated with $\gamma = 10$ and $\eta = 10$ for 2000 spheres allowed to settle on a fixed square surface layer. The sharp high peaks show the square layers packed in an fcc arrangement.

fcc crystal packing in this case. Figure 7.9 shows the vertical density variation for the sphere packing. We observe sharp high peaks from the square layers packed in an fcc arrangement. This tendency for spheres to order more readily when packed onto a square layer compared to a triangular layer is easy to understand if we consider that there is only one way to pack another square layer under the surface square layer, in contrast to the two (B and C) possibilities for packing onto a triangular packed layer.

Figure 7.8 also shows an fcc packing formed by releasing spheres one at a time from the middle of the bottom of the simulation box and allowing them to settle on the fixed square packed surface layer. This simulation was performed with $\eta = 10$ and $\gamma = 10$. The system is seen to form a perfect fcc packing. It does this more readily than the case with a triangular packed top layer, again due to there being only one type of site for the incident spheres to pack in.

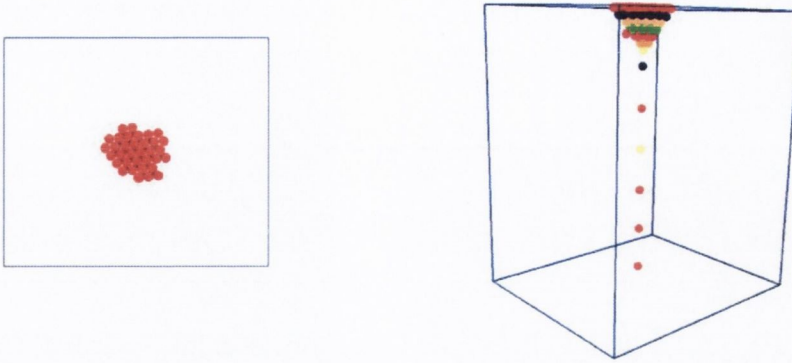


Figure 7.10: Figures shows the formation of an ordered surface layer using an attractive force between the surface spheres (Left) and the subsequent formation of an ordered packing underneath (Right).

7.5.4 Formation of an ordered surface layer

As already noted, a surface layer of mono-dispersed bubbles in a liquid readily forms an ordered triangular packed arrangement. This is both due to the ready ordering of 2D-monodispersed circles (or 3D spheres confined to a plane) and also due to the bubbles attracting one another due to surface tension forces.

We have performed simulations where instead of fixing the surface layer in a triangular packed arrangement, we have added an attractive force between the spheres that lie at the top of the simulation box. The attractive force between two surface spheres is given by

$$F_{\text{attract}} = K_{\text{attract}} d'. \quad (7.7)$$

where d' is the distance between the centres of the spheres.

In this way we can release a stream of spheres into the empty simulation box, have them rise to the top of the box where they readily order into a triangular arrangement. Further triangular packed layers of spheres form in a similar manner

as that observed in our simulations of deposition of spheres onto a fixed triangular surface layer shown in the previous section. Figure 7.10 shows a packing generated in this way with $\eta = 10$, $\gamma = 10$ and $K_{\text{attract}} = 10$.

7.6 Discussion

Simulations of random packings of spheres using our random packing algorithm have been shown to produce dense random packings at densities consistent with the random close packing of spheres (RCP) [12]. Dynamic simulations of the deposition of spheres onto a triangular packed layer show greatly differing behaviour depending on the system parameters. We have considered the case of releasing a large number of spheres simultaneously into the simulation box and determined the resulting order of the the packing. We find that in the limit of a highly dissipative system, the spheres pack randomly. However in the case of a weakly dissipative system, we find that the system behaviour mimics a slow cooling or annealing and a rhcp packing of spheres forms.

When we consider a packing of spheres generated by releasing spheres one at a time from the center of the bottom of the simulation box, we find that the system can exhibit a high degree of order. It is even possible for a perfect fcc packing to form in the limit of high dissipation, providing the initial spheres arrange themselves correctly.

Simulations of the deposition of spheres onto a square packed surface layer show an even greater tendency to order. An fcc crystal packing is obtained even when a large number of spheres are released simultaneously into the simulation box in a highly dissipative system. This is in contrast to the random packing that is obtained when the same simulation is run using a triangular packed layer. This greater tendency to order is attributable to the fact that simply filling all the sites

created by a square packed layer will generate a second ordered square layer. In contrast for a triangular packed layer there is two possible ways for a second layer to pack (into either the B or the C sites), and randomly filling both B and C sites will create disorder in the packing.

We have also shown that if an attractive force between the surface spheres is added to the simulation, then we are able to simulate the formation of an ordered triangular packing at the surface, and the subsequent packing of ordered layers of spheres. This was conceived as a toy-model that could be used to conceptualize a possible packing mechanism for the bubbles in the wet foam experiment; with bubbles rising up from the bottom of a container of water to settle in an ordered triangular packing at the surface, with ordered layers of bubbles packing underneath. However recent more detailed experimental results suggest that the ordered packing of the bubbles observed in the experiment is not sensitive to the exact method by which the sample is prepared. Experiments have been performed releasing the bubbles from a height above the sample, from bellow the surface in the liquid and even directly into the middle of the foam. In all cases the same high degree of ordering of the bubbles has been observed.

These simulations have highlighted the differences between systems composed of packed spheres and the bubble packings in the wet foam limit. The ready ordering of spheres deposited onto square packed layers is not sufficient to explain the ordering observed in the experiment as only approximately 5% – 10% of the structures observed at the surface in the experiment are fcc (100).

The ordering mechanisms demonstrated for depositing spheres on a triangular packed layer are also insufficient to offer an explanation of the order observed. The experiment is not performed sufficiently slowly enough to exhibit a packing mechanism similar to that observed in our simulations of packings generated by adding spheres one at a time to a packing in a a viscous liquid. The experiment also does

not exhibit anything resembling the slow annealing type process used in our simulations to generate rhcp packings of a large number of spheres simultaneously added to the system. While our simulations have demonstrated the degree to which an ordered surface layer can assist greatly in ordering layers of spheres (or bubbles) placed underneath it, the order observed in bubble packings in the wet foam limit still lacks a satisfactory explanation. The comparison of these simple simulations with experimental observations has helped us in better understanding the behaviour of the wet foam system and in particular highlighting the necessity for an additional, as of yet unknown, key ingredient to develop theoretical explanations of the order observed in the wet foam system. One direction which could be pursued would be to abandon simple sphere interactions and attempt to consider a more appropriate form for the interaction between the bubbles [62], and to then investigate under what circumstances crystallisation would occur. It is also unclear what role the liquid in the foam, and in particular liquid drainage, plays in the ordering process in the experiment. Simulations of the fluid dynamics of such flows of liquids through ordered bubble structures could yield interesting insights into the behaviour of these wet foam system [103].

There are other examples of the generation of ordered packings of spheres by various techniques. Pouliquen *et al.* has shown that beads poured at low flow rates into a horizontally shaken container order, with large areas of r.h.c.p. observed [85]. They have further shown that if the bottom layer is fixed in a square packing corresponding to the fcc (100) plane, then a perfect fcc crystal can form. These results are consistent with the behaviour of the sphere packings observed in our simulations. Carvente *et al.* has also shown that spheres subjected to large vibrations followed by a cooling procedure (annealing) can readily order [20]. Both body-centered-tetragonal and fcc arrangements are observed depending on the shape of the container. These order-

ing mechanisms mimic the ordering observed in Brownian hard spheres, where the spheres order due to thermal fluctuations and spontaneous crystallization can occur [112].

Chapter 8

Application of The Viscous Froth Model to the Flow of Ordered Arrays of Bubbles

8.1 Introduction

When a quasi 2-dimensional packing of monodisperse bubbles is made by trapping the bubbles between two glass plates the bubbles will readily order in a triangular packed arrangement [104]. If the liquid fraction is very low then we will have a dry foam in which the bubbles will form hexagonal shapes and the packing is then referred to as a honeycomb (This has the same appearance as the hexagonal lattice we considered in Chapter 6 and an image of it can be seen in Figure 6.9). However other ordered packings of bubbles can be made by confining the quasi 2-d bubbles to channels etched into the glass plates. Our group has developed novel methods for the manipulation of these packings of bubbles and it is currently being investigated if these methods could be applied to the systematic processing of small gas and liquid samples [39]. These methods (which we have termed *Discrete Microfluidics*, enable

the manipulation of ordered foam and emulsion structures in branched networks of channels and have been shown to be highly controllable and reproducible. Using this technology it is possible to perform “sample operations” on the bubbles such as sorting, replacing, adding and removing of bubbles. Further control of the system can be obtained using ferrofluids and appropriately designed magnetic fields. This research has clear applications in areas such as the pharmaceutical industry, where samples undergo systematic testing.

Here, we firstly outline some of the techniques and channel geometries used, and the success and failure of traditional simulation techniques in reproducing the behaviour of these systems. We will then outline the viscous froth model that we used to simulate a system whose behaviour cannot be replicated using traditional simulation techniques. Finally, detailed results of simulations will be given, including the first quantitative agreement between simulations and experiment.

8.2 Manipulation of ordered arrays of bubbles

The experimental system is a quasi-2D systems of typically 0.5 – 1.5 mm channel depth and up to 10 mm channel width. The channel geometries are computationally designed and then carved into a plane Plexiglas sheet. This is glued onto another plane Plexiglas sheet in order to close the channel system. In these types of channels all walls are Plexiglas, which provides constant surface properties throughout the system. Bubbles of equal volume are generated by injecting nitrogen gas into Fairy Liquid dish washing solution of 0.4 % concentration. The bubbles are then driven through the channel system by applying a constant gas (nitrogen) pressure at the inlet.

8.2.1 Adding/removing or replacing bubbles

By utilising T junctions or crossing of channels it is possible to add/remove bubbles from the packing (see Figure 8.1). This is done by controlling the flow/pressure in each of the channels. In the figure below, the yellow bubble in the main channel is replaced by the red one.

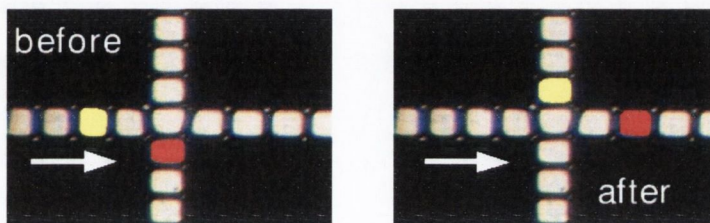


Figure 8.1: Replacement of bubbles by controlling flow/pressure in the channels [39]. *Pictures courtesy of Wiebke Drenckhan.*

8.2.2 Sorting of bubbles into different branches of a network

Branching channels can be used to sort bubbles from the packing into different parts of a network or to (re)combine them (see Figure 8.2) to create a new packing. By varying the relative distances the bubbles travel between separation and recombination it is possible to introduce shifts between the rows of bubbles in the packing.

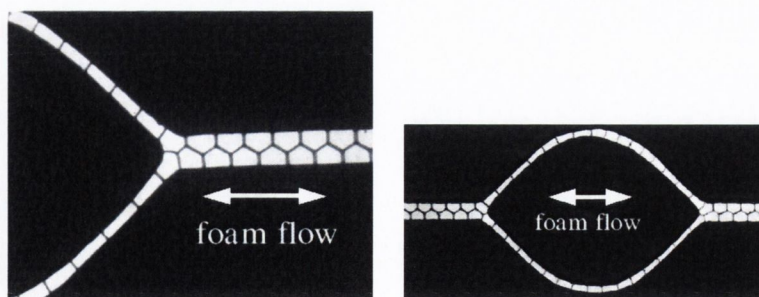


Figure 8.2: Two rows of bubbles are sorted into two narrow channels [39]. The process is reversible. *Pictures courtesy of Wiebke Drenckhan.*

Rearrangement of bubbles in the packing can be achieved by utilising appropriate necks or bulges in the channel (see Figure 8.3).

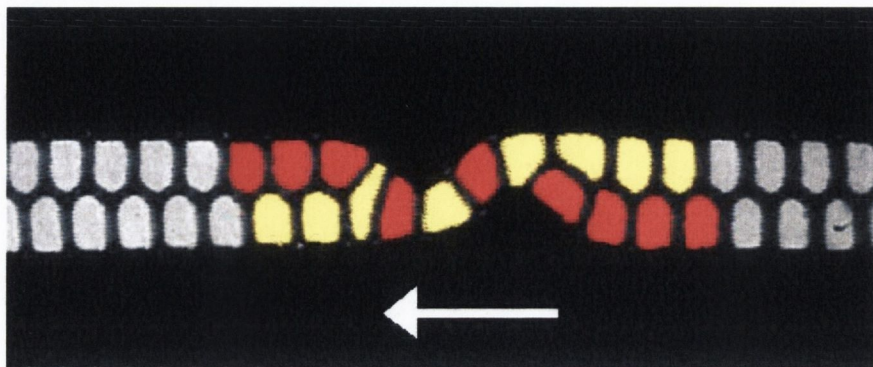


Figure 8.3: An asymmetric neck is used to rearrange the bubbles to cause an interchange of the top and bottom rows in the packing [39]. *Picture courtesy of Wiebke Drenckhan.*

8.2.3 Controlled neighbour switching in a U-bend

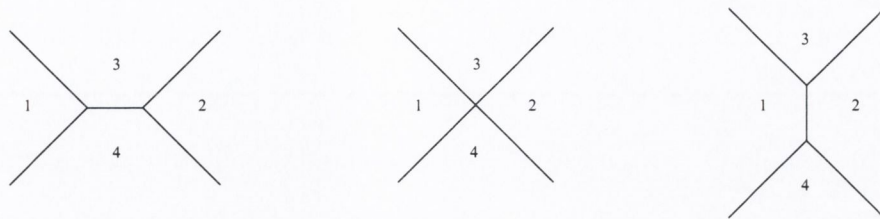


Figure 8.4: Diagram showing a neighbour switching T1 process. Initially bubbles 3 and 4 are neighbours. The length of the small edge in the middle reduces to zero and an unstable four fold vertex is formed. The vertex dissociates into two new three fold vertices resulting in bubbles 1 and 2 becoming neighbours.

A T1 process is a neighbour switching process between the bubbles in a foam. It occurs when an unstable four fold vertex (a point where 4 bubbles meet) dissociates into two stable threefold vertices (See Figure 8.4). When the foam structure is passed (sufficiently fast) around a U-bend it causes a shear on the structure which induces a series of T1 processes, which cause neighbour switching in the structure (see Figure 8.5). This causes an effective phase shift in the order of the two trains of bubbles.

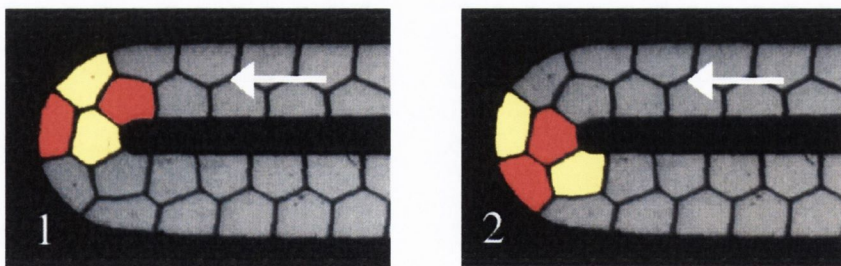


Figure 8.5: A phase shift in order of the bubbles caused by passing around a U-bend [39]. *Pictures courtesy of Wiebke Drenckhan.*

8.2.4 Success of traditional simulation techniques

Quasi-static simulations are the traditional method of simulation for these types of rheological systems [104]. These simulations proceed by a sequence of small movements of the structure, followed by minimisation of the energy. The aim is to keep the structure in equilibrium and at an energy minimum. Quasi-static simulations of all of the systems described here replicate the behaviour observed experimentally, with the exception of the T1 process observed in the U-bend experiment [39]. Quasi-static simulations of this experiment do *not* show the neighbour switching, in keeping with the low-velocity experimental results. So clearly the neighbour switching process is a dynamic effect that cannot be described by considering the system simply moving through a sequence of well-defined energy minima. This was one of the motivations in developing new tools to simulate these systems with the inclusion of external dissipation, by modelling the viscous drag of the bubbles against the glass plates which confine them, as described in section 8.3.3. To simulate this system we employ a computational simulation of the Viscous Froth Model, a dynamic model which includes the effects of viscosity.

We will now outline the theory and computational implementation of the Viscous Froth Model we have utilised to model this system.

8.3 Viscous Froth Model

The viscous froth model is a dynamical model describing the evolution of 2d foams. It was introduced over a decade ago in the context of domain growth [44, 105]. The model goes beyond other attempts to incorporate viscosity into simulation, which considered interfaces between bubbles as straight lines, with the viscous dissipation being concentrated at the vertices [57, 83]. The viscous froth model has been used to simulate the dynamics of isolated topological events such as the relaxation of a foam following a film rupture and the T1 process that occurs when the array of bubbles is passed around the U-bend [58]. Here we will outline the details of the viscous froth model, firstly describing its two commonly considered limiting cases and then its application to the simulation of the behaviour of controlled flow of ordered arrays of bubbles and in particular the case of the U-bend.

The viscous froth model describes the forces per unit length (See Figure 8.6) on a point on a film where two bubbles meet by:

$$p_i - p_j = \gamma c - \lambda v_{\perp}^n \quad (8.1)$$

where p_i and p_j are the gas pressures in adjacent cells i and j , γ is the surface tension, c is the local curvature of the boundary and v_{\perp} is its normal velocity. The coefficient of viscous drag is denoted by λ . The exponent n has been established to be $\frac{2}{3}$ [19].

Two limiting cases of the model exist: The ideal soap froth model and grain growth.

8.3.1 Quasi-static Soap Froth

In the case where the viscosity is negligible ($\lambda \rightarrow 0$), equation 8.1 reduces to that of the ideal soap froth:

$$\Delta P = \gamma c \quad (8.2)$$

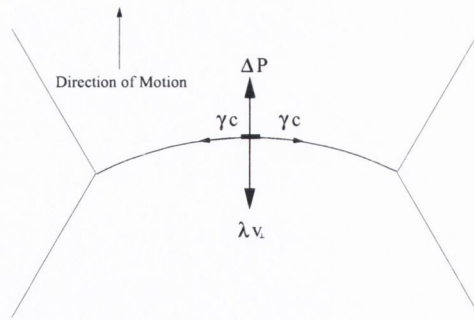


Figure 8.6: Forces acting on a film segment of length l .

This is Laplace's Law. It states that the films of a bubble are arcs of circles. Neglecting gas diffusion, the system will be in a constant state of equilibrium between the pressure and surface tension forces. The structure obeys Plateau's rules, which state that for a dry foam: films intersect only three at a time, where they must do so at 120° [104].

Gas diffusion across films due to pressure differences will result in the growth of some bubbles and the shrinkage and disappearance of others. This is known as coarsening and results in the growth of the average bubble area. Fick's law is used to describe the diffusion of gas between two bubbles i and j :

$$\frac{dA_{ij}}{dt} = \kappa \Delta P_{ij} l_{ij} \quad (8.3)$$

where κ is a permeability constant, and ΔP_{ij} and l_{ij} are the pressure difference and interface lengths of bubbles i and j . If we follow each edge in an anticlockwise manner, the tangent will turn through:

$$\Theta_i = \frac{l_i}{r_i} \quad (8.4)$$

for each film i of length l_i with curvature r_i^{-1} . As stated in Plateau's rules, there is a turning angle of $\pi/3$ at each of the n_i vertices, thus we may write:

$$\sum_i \frac{l_i}{r_i} = \frac{\pi}{3} \left(1 - \frac{n_i}{6}\right). \quad (8.5)$$

This is known as the curvature sum rule. Combining Eqns. 8.2 and 8.3 we obtain:

$$\frac{dA_{ij}}{dt} = \kappa\gamma \frac{l_i}{l_j} \quad (8.6)$$

If we now sum over the films of bubble i using Eqn. 8.5, we obtain:

$$\frac{dA_i}{dt} = \frac{\pi}{3} \kappa\gamma (n_i - 6) \quad (8.7)$$

This is Von Neumann's law [76]. It states that bubbles with less than six sides will shrink, those with six will stay the same size and those with more than six sides will grow.

8.3.2 Grain growth

The other limiting case of the viscous froth model is that of grain growth. This occurs when pressure differences between bubbles are negligible ($\Delta P_{ij} \rightarrow 0$). The motion of the films is then driven by curvature, as is the case in domain growth in metals [14]. The interface motion is determined by the balance between the 2nd and 3rd terms in Eqn. 8.1:

$$v_{\perp} = \frac{\gamma}{\lambda} c \quad (8.8)$$

This leads to the same type coarsening law as in the case of the ideal soap froth model:

$$\frac{dA_{ij}}{dt} = \frac{\pi}{3} \frac{\gamma}{\lambda} (n_i - 6) \quad (8.9)$$

known as Mullins law for grain growth [73].

We will employ the full viscous froth model as described in Eqn 8.1, but neglect the contribution of coarsening since it is negligible on the time scale of the foam passing around the U-bend.

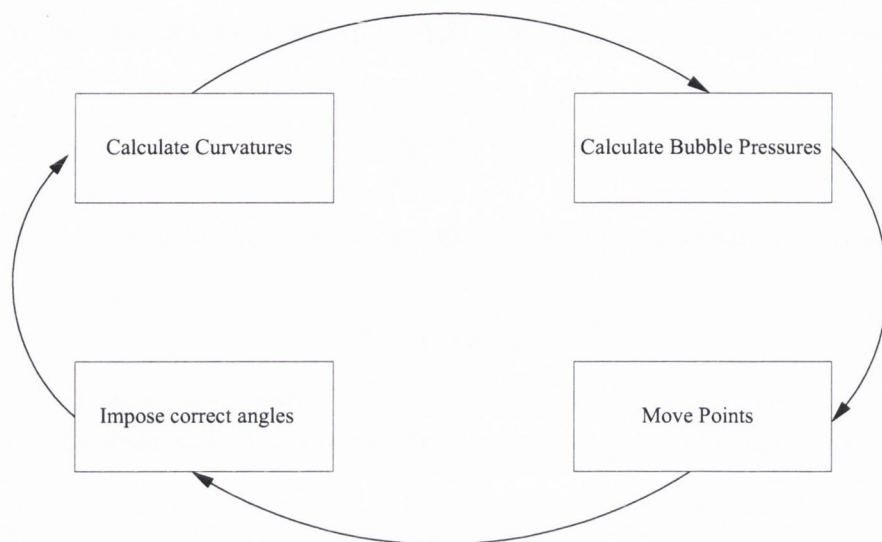


Figure 8.7: Flow diagram showing order of events in Surface Evolver simulation using the viscous froth extension.

8.3.3 Computational Implementation

We employ a software program called Surface Evolver to model the flow of the ordered arrays of bubbles. Surface Evolver is an interactive program for the modelling of liquid surfaces shaped by various forces and constraints [15]. This software can be used to simulate foam systems and foam flow through channels. In modelling foams, one sets up a Surface Evolver calculation by defining the vertices, edges, faces, surface tensions and any constraints on the system. Surface Evolver then evolves the system toward minimal energy by a gradient descent method. Quasi-static simulations of foam flow proceed by repeated steps of moving the foam structure a small amount and then minimising the energy. Such simulations using the Surface Evolver, replicate the behaviour of the flow of the bubbles in the channels described in section 8.2, except for the case of the U-bend.

Simon Cox, a then member of our research group, created an extension to Surface Evolver that allows simulations using the viscous froth model [58]. It relies on Surface Evolver for all the necessary topological “book-keeping” and adherence to

boundaries (e.g. solid walls), while implementing the numerical scheme described here in Evolver's command language. Initially an external C program was used in determining the bubble pressures, but Ken Brakke, the software's developer added matrix manipulation functionality to Surface Evolver, which allowed the entire implementation to be done in Surface Evolver's own command language.

We will now describe the numerical implementation of the viscous froth model (see Figure 8.7).

8.3.4 The Dimensionless Viscous Froth Equation

Here we write the defining equations in terms of dimensionless variables: the typical energy scale is γR , and the (2d) pressure scale is γ/R , where R is the mean bubble radius. Thus we may write Eqn. 8.1 as:

$$\Delta \hat{p} - \hat{K} = \hat{v} \tag{8.10}$$

where the dimensionless variables are

$$\hat{p} = \frac{p}{\gamma/R}, \quad \hat{K} = KR \quad \text{and} \quad \hat{v} = \frac{v}{\gamma/(\lambda R)}.$$

8.3.5 Curvature

We resolve all the films of the bubbles in the system into a sequence of points, connected by straight line segments of finite length (edges). The calculation of the surface tension requires the curvature of the film at a point. Figure 8.8 shows the curvature pointing outward from the surface at the point where edges e_1 and e_2 meet. This is defined to be the direction of the normal, as is required by Laplace's Law which requires the surface tension to be normal to the surface. The curvature is then calculated by:

$$K = \sqrt{K_x^2 + K_y^2} \quad (8.11)$$

$$= \sqrt{\left(\frac{\hat{t}_{2x} - \hat{t}_{1x}}{l}\right)^2 + \left(\frac{\hat{t}_{2y} - \hat{t}_{1y}}{l}\right)^2} \quad (8.12)$$

where $l = (l_1 + l_2)/2$, \hat{t}_{1x} , \hat{t}_{1y} , \hat{t}_{2x} and \hat{t}_{2y} are the unit x and y tangent vectors to e_1 and e_2 , respectively. This is a first order approximation to the more usual definition of curvature $K = \frac{\theta}{l}$.

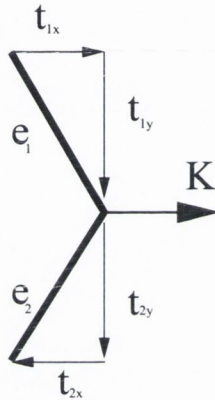


Figure 8.8: The curvature K , at the point where edges e_1 and e_2 meet. The x and y tangents to the edges are given by t_{1x} , t_{1y} , t_{2x} and t_{2y} .

8.3.6 Determination of Bubble Pressures

After calculation of the local geometry and calculation of the resulting surface tension forces, it is necessary to calculate the bubble pressures. In the general case (arbitrary exponent ν in Eqn. 8.1) this might be done using an iterative procedure, introducing a penalty function to keep the bubble areas fixed [58]. Currently we use a simplification to the general viscous froth model by considering the case of linear dissipation ($\nu = 1$). This leads to a more computationally efficient implementation of the model.

If we integrate the equation of motion (Eqn. 8.1) around the boundary ∂b of an arbitrary bubble b , the change in the area of the bubble is equal to the integral of the normal velocity field v on the surrounding film:

$$\frac{dA_b}{dt} = \oint_{\partial b} v dl = \oint_{\partial b} (\Delta P - K) dl. \quad (8.13)$$

Using the same arguments outlined in section 8.3.1, the curvature must integrate around a bubble to 2π , deducting $\frac{\pi}{3}$ at each of the n_b vertices:

$$\frac{dA_b}{dt} = \frac{\pi}{3}(n_b - 6) + \sum_{b'} (P_b - P_{b'}) l_{bb'} \quad (8.14)$$

where $l_{bb'}$ is the length of the film shared by bubbles b and b' and the summation is over all bubbles b' adjacent to b . (From this definition for $l_{bb'}$, it is clear that $l_{bb'} = 0$ if b and b' are not neighbours or if $b = b'$). Eqn. 8.14 represents a matrix equation for the N bubble pressures,

$$L_{bb'} P_{b'} = \dot{\alpha}_b \quad (8.15)$$

The matrix $L_{bb'}$ is given by:

$$L_{bb'} = \begin{cases} \sum_{b''} l_{bb''} = l_b^{tot} & \text{if } b = b' \\ -l_{bb'} & \text{otherwise} \end{cases}$$

where l_b^{tot} is the total length of the perimeter of bubble b . The b^{th} entry of the matrix $\dot{\alpha}_b$ is given by:

$$\dot{\alpha}_b = \frac{dA_b}{dt} - \frac{\pi}{3}(n_b - 6) \quad (8.16)$$

The evolution of the network can now be predicted a time step δt ahead as we will explain in the next section.

8.3.7 Velocities and Displacement

If we consider the velocity of a point on a film, this is determined by the local geometry and the pressures of adjacent cells, according to the viscous froth equation:

$$v[\Delta P, K] = \Delta P - K \quad (8.17)$$

The velocity v is in the normal direction, its sign being chosen consistent with the signs of the pressure drop ΔP and curvature K . In a time step δt , the resulting displacement is made in the normal direction associated with this point.

After each point of the discretisation has been displaced, all the 3-fold vertices are moved in order to maintain angles of 120° . This is accomplished using an analytic solution to the Fermat-Steiner problem, which is only correct to lowest order, since no curvature of the line segments is considered when determining their point of intersection [46].

8.4 Simulation Results

Simulations that had previously been performed using the viscous froth model showed that the model replicated the behaviour seen in the experiment [58]. For low velocities no T1 occurred in the U-bend, while for velocities above a critical velocity v_{crit} a T1 would occur in the bend. In this work we examine the detailed dependence of the critical T1 velocity v_{crit} on the system parameters. We consider the effect of varying the area of the bubbles A_b , the radius of the bend R and the width of the tube d . We also perform the first quantitative measurements using the viscous froth model, making an estimate of the value of the viscous drag parameter λ .

As already stated, simulations using the quasi-static model show no neighbour switching process taking place in the U-bend, which is consistent with the low veloc-

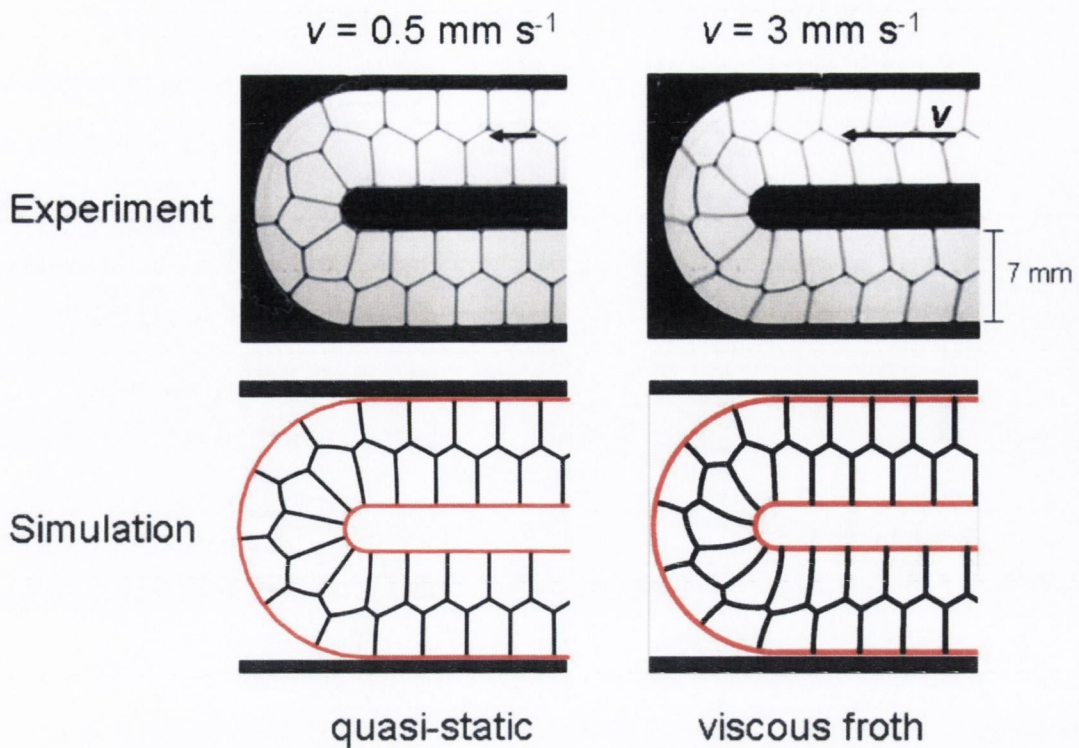


Figure 8.9: Comparison of the distortion of a foam structure going around a bend without neighbour switching (T1) of bubbles.

ity experimental result. In this limit, the foam structure looks as shown on the left in Fig. 8.9, flowing around the bend without undergoing any topological changes. Upon increase of the velocity v , the viscous forces of the films being dragged along the top and bottom plate become of the order of magnitude of the surface tension force. Since the local velocity - and hence the viscous force - increases towards the outer boundary of the bend, an additional shear stress is imposed on the foam structure within the bend. For sufficiently high flow velocities this leads to a clearly visible distortion of the structure, as can be seen on the right in Fig. 8.9.

A key thing to note at the outset is that there are three possible ways to pass this structure around the U-bend.

- **Case 1: The leading outer three-sided bubble**

The first case, which we will refer to as the case of the “leading outer three-sided bubble”, is illustrated in Figure 8.10. For a finite train of bubbles in the foam structure shown, all bubbles have four sides (discounting the side that each bubble makes with edges of the channel), except for a three-sided bubble at either end required to make the structure stable. In the first case, this three-sided bubble is on the outside as the bubbles enter the bend.

- **Case 2: The leading inner three-sided bubble**

The second case, which we will refer to as the case of the “leading inner three-sided bubble”, is illustrated in Figure 8.11. In this case the three-sided bubble is on the inside as the structure enters the U-bend.

- **Case 3: Tube fully filled**

The third possibility is that the tube will be fully filled with bubbles before we begin pushing the structure. This is illustrated in Figure 8.12. This is the initial setup that was used in the lab experiment.

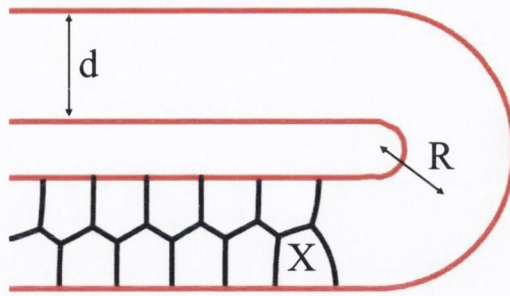


Figure 8.10: Case 1: The leading 3 sided bubble is on the outside as the bubbles enter the bend.

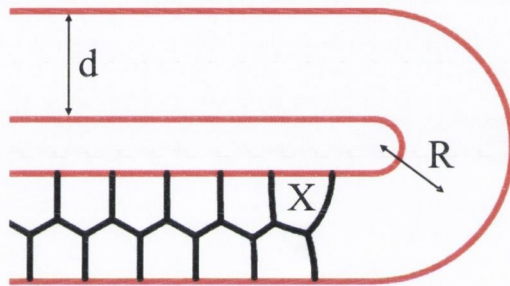


Figure 8.11: Case 2: The leading 3 sided bubble is on the inside as the bubbles enter the bend.

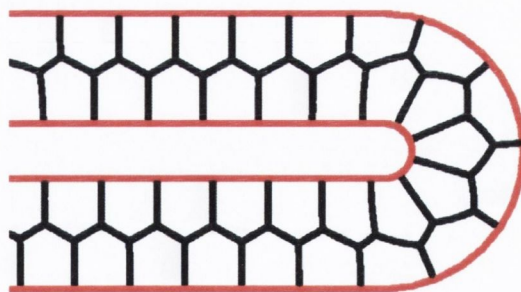


Figure 8.12: Case 3: The third possibility is that the tube is already filled with bubbles, before the bubbles start to be pushed.

The first simulations of the U-bend using the viscous froth model considered case

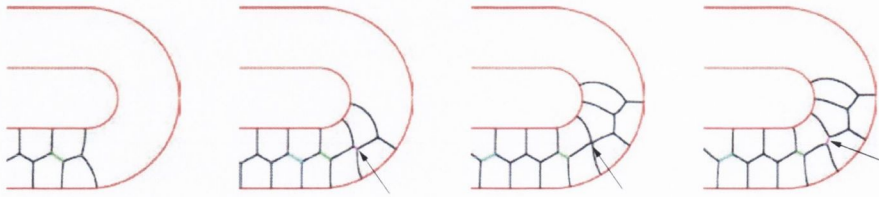


Figure 8.13: Case 1: The leading 3-sided bubble is on the outside as the bubbles enter the bend. The structure is pushed at a velocity just above v_{crit} . We see that the T1 process takes place as the bubbles enter the bend in contrast to Case 2 where the bubbles fill the bend before the T1 process takes place. v_{crit} is lower for case 1 than for case 2 or case 3 due to the end effects as the structure enters the bend.

1, that of a leading outer three-sided bubble [58]. These simulations looked at the variation of v_{crit} with bubble area and found that v_{crit} was inversely proportional to the area of the bubbles. It was thought at that time that there would be little difference between cases 1 and 2, just that the critical T1 velocity v_{crit} would be a factor of 2 higher. It also was not considered if either case 1 or case 2 represented the experimental setup of case 3, that of the tube being initially full of bubbles.

In simulations involving case 1, the T1 process occurs as the structure enters the bend. However in case 2, the structure will first fill the bend before any T1 process take place. This is due to the finite end-effect in case 1 tending to decrease the length of the edges that will shrink to a zero length and undergo a T1 process as the structure enters the bend (See Figure 8.13). However for case 2 the finite end-effect tends to increase the length of these edges, so that the structure fills the whole bend before any T1 processes takes place (See Figure 8.14). Thus Case 2 effectively recreates Case 3 (that of a fully filled tube) before any T1 takes place. To verify that this was the case we performed simulations of Case 3, that of the bend filled with a relaxed foam structure, and verified that the critical T1 velocity for case 2 is the same as that of the experimental setup of case 3. The results presented here will

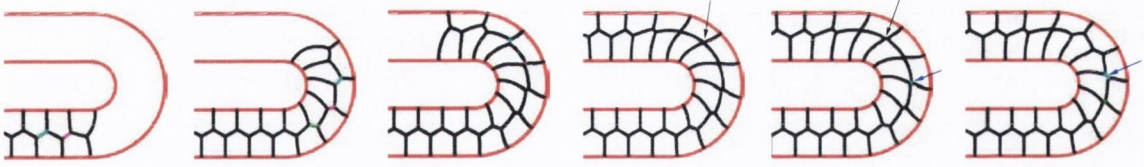


Figure 8.14: Case 2: The leading 3-sided bubble is on the inside as the structure enters the bend. We see that the tube first fills with bubbles before any T1 processes takes places, creating the same initial setup as case 3.

also show that cases 1 and 2 can behave very differently when the parameter values of the system are changed. In particular the previously reported inverse relationship between the areas of the bubbles and the critical T1 velocities is not valid for the experimental setup of case 3.

In the experimental system, at a critical velocity v_{crit} the shortest film in the bend shrinks to zero length, triggering the T1. Before this sets in, all bubbles have 4 interior edges. Upon the flipping of the edge two pairs of 5- and 3-sided bubbles are generated, of which one pair follows the foam flow and leaves the bend. The other one moves into the bend to release the strain. This topology is sufficient to cause a T1 process for all the subsequent bubbles that enter the bend, even if the velocity is reduced to $v \rightarrow 0$. Also, for large velocities more than one T1 process can occur in the bend. This is observed experimentally and reproduced by the simulations.

8.5 Variation of system parameters

In our simulations, we setup a chain of bubbles in one of the possible initial structures described above. All bubbles have the same area A_b . A single bubble of area A_o , spanning the width of the channel, is placed at one end of the tube and inflated at a rate \dot{A}_o in order to push the other bubbles around the bend. The bubbles therefore move at a velocity

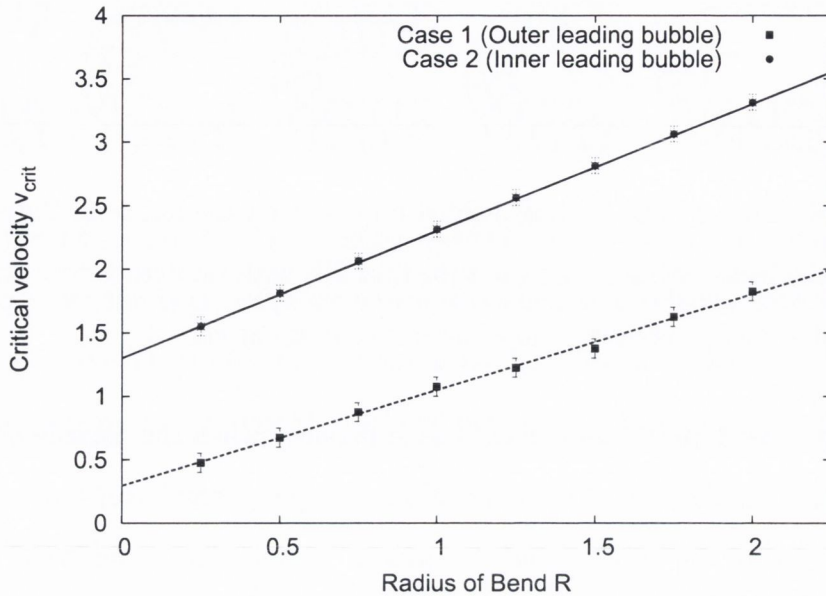


Figure 8.15: Variation of the critical T1 velocity v_{crit} with the radius of the tube. A clear linear relationship is seen for both cases. The slopes of the lines shown are $m = 0.75 \pm 0.02$ (Case 1) and $m = 1$ (Case 2).

$$v = \frac{\dot{A}_o}{d} \quad (8.18)$$

where d is the width of the tube.

Here we will first present results for the variation of the critical T1 velocity with various system parameters for case 1 and case 2. We have varied the radius of the bend R , the width of the tube d and the area of the bubbles A_b . The behaviour of case 2 is the same as that of case 3. We will then outline how the first quantitative estimate of the viscous drag parameter λ was obtained by comparing the minimum edge lengths of the bubbles as they pass around the U-bend at a velocity below v_{crit} .

8.5.1 Variation of the radius of the bend

As the train of bubbles is pushed around the U-bend a shear is imposed on the system. Firstly, we consider the effect of varying the radius of the bend R . It is

clear that increasing the radius of the bend will decrease the shear rate for a given velocity of the bubble train. (We need only consider the extreme case of an infinitely large radius, which would correspond to a straight tube and no shear stress on the system.) Simulations were done to ascertain the critical T1 velocity for the cases of a leading outer bubble (case 1) and a leading inner bubble (case 2). Both sets of simulations were run for a system of bubbles with area $A_b = 1$, in a tube of diameter $d = 2$ with the viscous drag parameter $\lambda = 1$. A clear linear relationship between v_{crit} and the radius of the bend is found for both cases as shown in Figure 8.15. For all values of radii considered, v_{crit} was higher for the case of the inner leading bubble (case 2) than for the outer leading bubble (case 1).

For the leading outer bubble case the first T1 process occurs as the structure enters the bend. There is then a succession of single T1 events as the subsequent bubbles enter the bend. However, for the case of the leading outer bubble, the bend is first filled with bubbles before the T1 processes take place. For larger radii, more bubbles are of course required to fill the bend. This can mean that for larger radii, multiple T1 events occur almost simultaneously in the bend (See Figure 8.14) and that multiple three-sided and five-sided bubbles can then be observed in the structure that exits the bend.

8.5.2 Variation of the width of the tube

Increasing the width of the tube d will cause two effects which will tend to decrease the critical velocity v_{crit} . Firstly, given that in travelling around the bend a film located at the outer edge of the bend will travel a distance πd greater than a film located at the inner edge, increasing d will increase the shear imposed on the structure. Secondly, for the relaxed structure in the straight tube, the lengths of the films that lie perpendicular to the sides of the tube are fixed at a length $d/2$. Thus increasing the width of the tube will increase the length of the films that lie

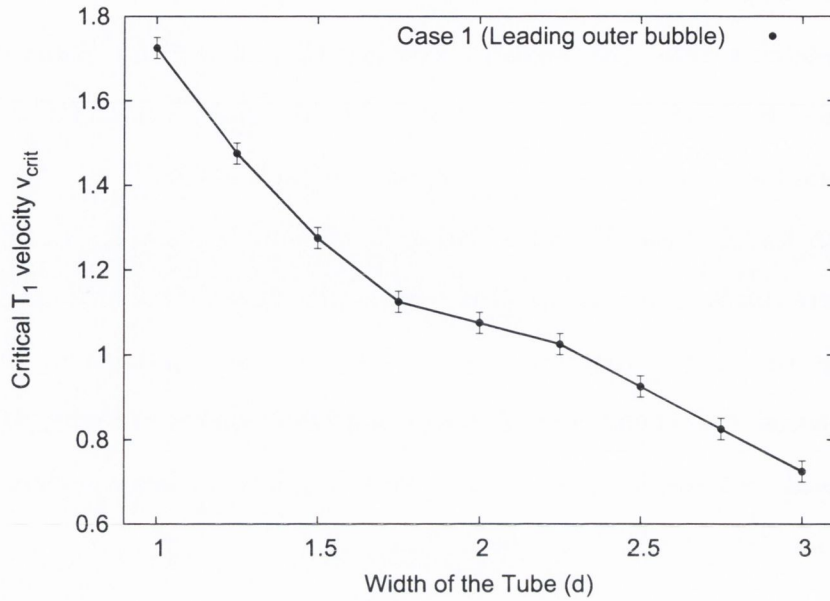


Figure 8.16: Variation of the critical T1 velocity v_{crit} with the width of the tube for the case of the leading outer bubble (case 1).

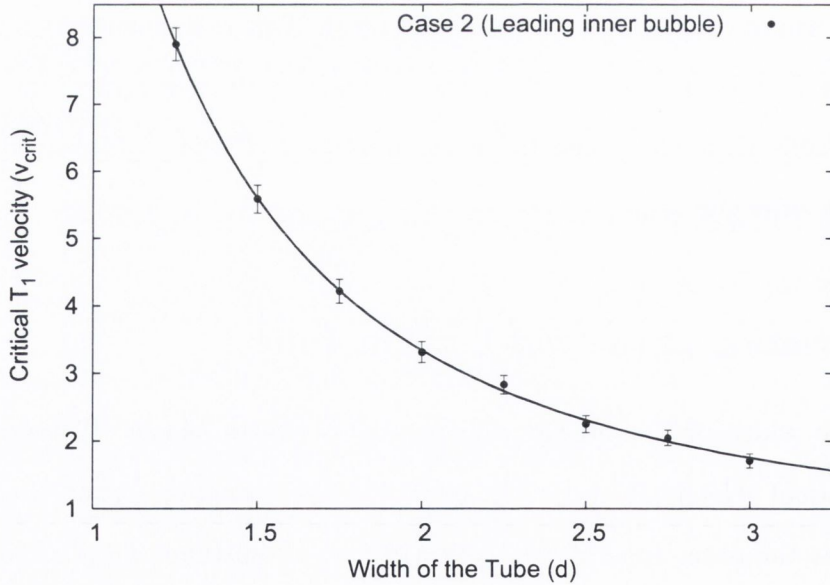


Figure 8.17: Variation of the critical T1 velocity v_{crit} with the width of the tube for the case of the leading inner bubble (case 2). The line is a fit of the function $f(d) = a(d)^b + c$, with $a = 11.6 \pm 0.1$, $b = -2.0 \pm 0.1$ and $c = 0.5 \pm 0.2$.

perpendicular to the edges of the tube and consequently the length of the edges that will undergo the T1 processes will decrease, so that the total area of the bubbles remains constant. As these edges are shorter entering the bend, it will require less shear on the structure to cause them to shrink to zero length and for a T1 to occur.

We find quite similar behaviour for both the case of the leading outer bubble (case 1) and the leading inner bubble (case 2). The simulation of case 1 was done with a tube of radius $R = 1$, with bubbles of area $A_b = 1$ and the viscous drag parameter $\lambda = 1$. The variation of the critical T1 velocity with the width of the tube d can be seen in Figure 8.16. We find that v_{crit} decreases as the width of the tube is increased.

Simulations of case 2 were run using a tube with radius $R = 2$, with bubbles of area $A_b = 1$ and the viscous drag parameter $\lambda = 1$. A fit to the data suggests the relation $v_{\text{crit}} \propto d^{-2}$ (See Figure 8.19).

8.5.3 Variation of the area of the bubbles

Varying the area of the bubbles shows the largest variation in behaviour between the case of the outer and inner leading bubble. Increasing the area of the bubbles A_b , while keeping the width of the tube d fixed, and thus the length of the films that span the width of the tube fixed, will cause the lengths of the edges that will undergo a T1 process in the bend to increase. This should cause v_{crit} to increase as the areas of the bubbles increase. This is indeed the behaviour that we find for case 2, that of the inner leading bubble (See Figure 8.19).

The case of the outer leading bubble (case 1) shows the opposite behaviour (See Figure 8.19). Here it is found that $v_{\text{crit}} \propto 1/A$. As the area of the bubbles is increased the length of the edge that undergoes the T1 as the structure enters the bend is decreased and so is v_{crit} . This occurs solely as a result of the end of effect of the finite sized bubble train. As case 2 has been shown to replicate the behaviour

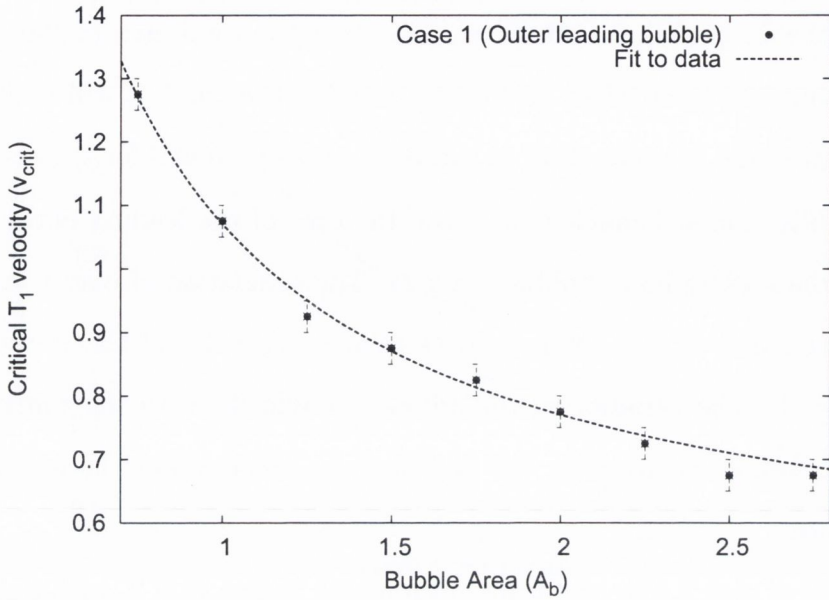


Figure 8.18: Variation of the critical T_1 velocity v_{crit} with the area of the bubbles for case 1. The data is fit to the function $f(A_b) = 0.6/A_b + 0.47$

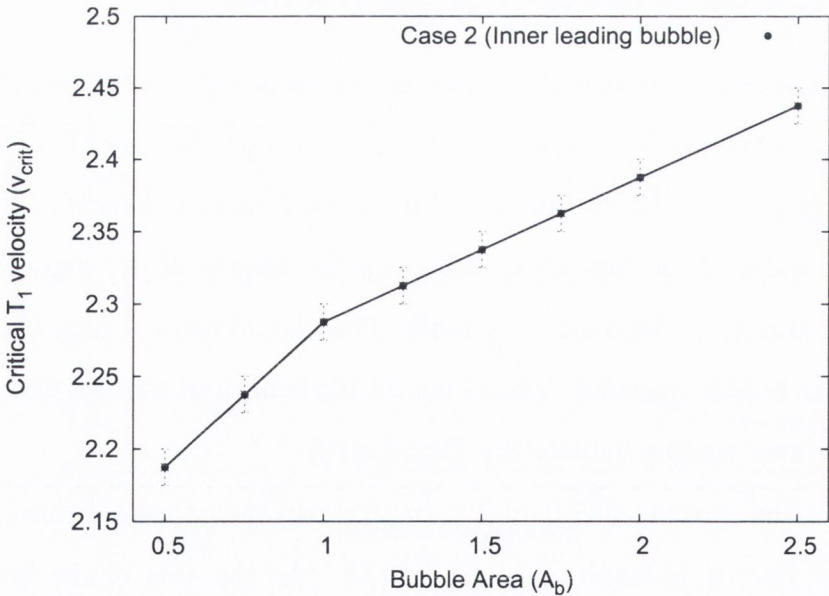


Figure 8.19: Variation of the critical T_1 velocity v_{crit} with the area of the bubbles for case 2.

of the experimental system (case 3), this inverse relationship of v_{crit} with area will not be seen in the experimental system (case 3).

For small bubble areas it is not possible to make a stable structure of the kind we consider in this work, instead a structure where three or more bubbles span the channel width is required. For large bubble areas, the structure dissociates into a “bamboo” structure with plane parallel films separating bubbles that span the channel width.

We will now outline how we have achieved quantitative agreement between the viscous froth model and the experimental system.

8.5.4 Determining the viscous drag parameter λ

The direct experimental measurement of the critical velocity v_{crit} is subject to significant errors. Thus in attempting to make a quantitative measure of the viscous drag parameter λ in our experimental system, we consider instead the minimum edge length of the films that would undergo a T1 at v_{crit} (see Fig. 8.20), when the foam is passed around the U-bend at a velocity below v_{crit} . As the foam moves through the bend, the length of these films decrease and then increases again, going through a well defined minimum length L , which is measured as a function of the foam flow velocity v . In the experiment, a very dry foam is used with a liquid fraction of less than 1%. The velocity v is increased very slowly to provide quasi-steady conditions. By doing this we can extrapolate to find v_{crit} for $L \rightarrow 0$, and determine the drag coefficient λ by fitting the numerical prediction to the experimental data. This is possible because λ acts as a scaling parameter for the velocity in Eqn. 8.1.

We set up a viscous froth simulation of the U-bend using the physical parameters of the experimental system: channel width $d = 7 \times 10^{-3}$ m, inner channel radius $R = 1.5 \times 10^{-3}$ m, bubble area $A_b = 1.86 \times 10^{-5}$ m² and the line tension $= 3 \times 10^{-5}$

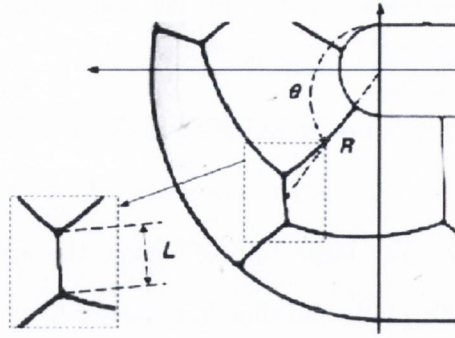


Figure 8.20: We measure the shortest edge length L as a function of foam flow velocity v around the U-bend. If this edge gets short enough, a T1 neighbour switching process occurs.

J/m. The line tension is the 2D analogue of the surface tension. It is estimated for the system by multiplying the surface tension of the solution (3×10^{-2} J/m²) by the depth (0.5×10^{-3} m) of the channel, and by the factor 2 in order to take account of the fact that each film consists of two interfaces. The drag parameter λ is replaced by an arbitrarily chosen $\lambda_{sim} = 1$ kg m⁻¹ s⁻¹, and later determined by fitting the experimental to the computational data. The tube is fully filled with foam (Case 3) and pushed around the bend at a range of velocities lower than v_{crit} . The minimum line length L_{sim} (shown in Figure 8.20) is determined for each velocity. The simulation data is fitted to a power law

$$L_{sim} = av_{sim}^b + d, \quad (8.19)$$

using a , b and d as fitting parameters. We obtain values of $a = -1.26 \times 10^{-3}$, $b = 1.29$ and $d = 1.98$ cm. To estimate a value for λ we fit the experimental data with the function

$$L_{exp} = a(2\lambda v_{exp})^b + d \quad (8.20)$$

where the factor 2 takes into account the drag occurring on the top and bottom plates.

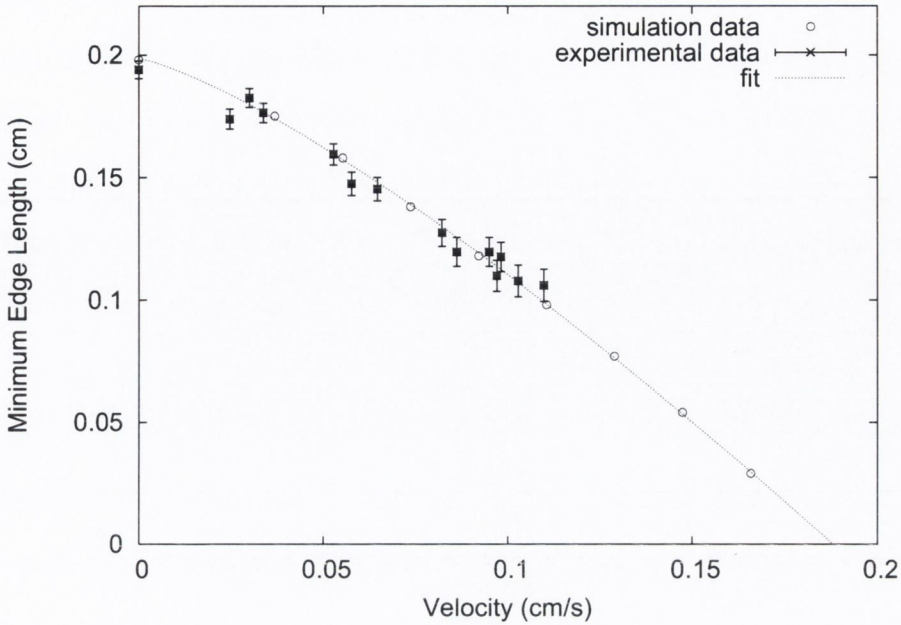


Figure 8.21: Determination of the viscous drag parameter λ through fitting data from viscous froth simulations to the experimental results. The critical velocity is found to be $v_c = 0.19$ cm/s. The minimum film length for zero velocity is taken from a quasi-static simulation.

From this procedure we obtain the value of $\lambda \approx 14 \text{ kgm}^{-1}\text{s}^{-1}$. Fig. 8.21 shows the experimental and simulation data, in which the latter was rescaled using the obtained λ parameter. A direct comparison of this value with previous estimates for the viscous drag [16, 19] is not straightforward as for example using a different value of α in Eqn. (8.1) changes λ .

8.6 Conclusion

In this work we have applied the viscous froth model to the flow of an ordered array of bubbles around a U-bend. We have highlighted the importance of the initial structure that is used before the bubbles are pushed through the bend. Previous simulations, which were compared to experimental results, used an initial structure

which does not replicate the full behaviour of the experimental system. We have performed a detailed analysis of how the variation of various system parameters affect the critical velocity at which a T1 process will take place in the bend. We have also obtained the first quantitative estimate of the value of the viscous drag parameter $\lambda \approx 14 \text{ kgm}^{-1}\text{s}^{-1}$. This estimate of λ will assist in the design of future experiments, which will also aim to establish a relationship between λ and the liquid fraction of the foam.

Chapter 9

Conclusion and Outlook

In this thesis we have presented new and exciting results that give insights into the packing behaviour of bubbles and grains.

We began by considering the behaviour of Newton's Cradle in terms of a simple 1D granular system where the interactions between the spheres are the same as those commonly considered in sphere packing models [53]. We provide the most complete description to date of the underlying physics of Newton's Cradle, bringing together simulation, experiment and theory. This work highlights how seemingly simple systems can exhibit complex behavior and provides us with an excellent introduction to the nature of the interactions between soft spheres.

We then went on to consider the role of shape in granular packings, providing a detailed description of the variation of the packing properties of systems composed of elliptical grains [29]. We find a very interesting variation in the packing fraction Φ with the ellipticity of the grains. We are also able to separate out the contribution to the packing of the grains from the rotational and translational degrees of freedom of the ellipses. Here we demonstrate that the increase in packing fraction that we observe as the shape of the grains transitions from circular to elliptical is due to the additional degree of freedom that the elliptical grains have, with the large increase

in Φ not observed in simulations where we disallow rotations of the grains.

We have considered the packing behaviour of objects with arbitrary shape in sequential packing models [31, 32], defining a new model which we have termed “Rotational Random Apollonian Packing” (RRAP), in which asymmetric objects additional rotational degree of freedom is taken into account. Our new RRAP model shows the dramatic effect that allowing asymmetric objects to rotate during the packing process has on the packing properties of these systems. This work has highlighted the need for the consideration of the rotational degree of freedom in future theories that consider the behaviour of such sequential packing models.

We have continued the theme of packing of objects with arbitrary shape when we consider our new model that describes the packing-driven shape evolution of a system of grains. This novel model allows the structure of the packing of the grains itself to determine the evolution of the shape of the grains. We see a very interesting behaviour, with the grains having a strong tendency toward angularity and over long term simulations forming triangular shapes. The behaviour of this system provides insights into how the abrasive forces that are felt between grains when randomly packed together may effect their shape evolution.

We have turned the traditional packing model “inside-out” by considering a system composed of Hooke’s Law interactions under extension only, and hence a model of elastic strings that are loose under compression [29]. The behaviour of this model was initially very surprising to us as it behaves so differently from the classical system of compressed sphere and disc packings [65]. We have highlighted these differences and performed a detailed analysis of the behaviour of the system at the onset of rigidity. As this model has shown such interesting behaviour, future work will investigate the elastic properties of the system at and above the onset of rigidity.

We have considered a dynamic model for 3D sphere packings which is the 3D

equivalent of the model we used in simulating Newton's Cradle [53]. We have performed simulations releasing spheres onto fixed square and triangular packed layers to investigate the degree to which the order in the top layer will propagate throughout the sample. These results have been compared to wet bubble packings which have been seen to produce a surprising degree of order [99]. The sphere simulations have highlighted the differences between the packing behaviour of simple sphere systems and that seen in the wet bubble experiment. While we find that ordered surface layers can indeed in certain regimes greatly assist in the ordering process of spheres deposited onto them, we are still unable to explain the spontaneous ordering in the experiment that is observed regardless of the method by which the foam sample is produced.

We have further investigated bubble packings in 2D foams and considered a dynamical model that incorporates the viscous drag on quasi-2D foam from the plates that confine them [58]. We see that this is a very important effect in certain circumstances and have performed a detailed analysis of a T1 process that occurs in a packing of bubbles that are passed sufficiently fast enough around a U-bend. These results have shown that previous simulations had considered an initial orientation of the foam structure that is not representative of the behaviour of the experimental system where the U-bend is full of foam prior to beginning the experiment. We have also determined a value for the viscous drag parameter λ in the experimental system. This estimate of λ will assist in the design of future experiments which will investigate the designing of new channel geometries for use in the potential application of this technology to the handling of small liquid and gas samples.

In conclusion, in this work we have presented original ideas and research results that contribute greatly to the study of packing problems. We have defined new models, considered new shapes and even turned the problem of packing "inside-

out". At its core this has been a computational investigation and the computational tools developed, and in particular the `ARBITRARYPACKER` software, with its ability to consider the packing properties of any desired two-dimensional shape, offer a limitless potential to further explore what scientists have considered for thousands of years - that of how things pack together.

Appendix A

Scaling relationships in PLG models.

Packing limited growth models like those investigated in Chapter 4 show a power-law variation for the limiting distribution of the radii of the packed objects

$$N(r) \propto r^{-\alpha} \tag{A.1}$$

and in the decay in the pore space volume for large n :

$$\rho(n) \propto n^{-\beta}. \tag{A.2}$$

Here we will outline the derivation due to Dodds and Weitz [31, 32] of the scaling relationship used to estimate α from β , in Chapter 4. Using this relation a more accurate estimation of α is obtained than attempting to directly fit to the power-law in Eqn. A.1. We also show the derivation of their model which they use to make theoretical predictions of the power-law exponents in the RAP model,

They consider an RAP packing of spheres and assume the following form for the

probability distribution of sphere radii after n spheres have been packed:

$$P(r; n) = \begin{cases} \frac{\alpha-1}{\alpha} r_c^{-1} & \text{for } r < r_c \\ \frac{\alpha-1}{\alpha} r_c^{-1} \left(\frac{r}{r_c}\right)^{-\alpha} & \text{for } r \geq r_c \end{cases} \quad (\text{A.3})$$

where r_c is the maximum size of any sphere that may be added. This makes the assumption that $P(r; n)$ above the cutoff scale r_c follows the limiting power law form while below the distribution is essentially flat. Dodds and Weitz have shown from numerical simulations that this is a reasonable assumption to make. The corresponding frequency distribution is then given by:

$$N(r; n) = \frac{\alpha-1}{\alpha} n r^{\alpha-1} r^{-\alpha} = k r^{-\alpha} \quad (\text{A.4})$$

for $r > r_c$. As the prefactor k must be constant:

$$r_c = \left(\frac{\alpha-1}{ak} n\right)^{1/(\alpha-1)} \propto n^{-1/(\alpha-1)} \quad (\text{A.5})$$

Dodds and Weitz also investigate the form of $P_{\text{ins}}(r; n)$, the probability distribution of the $(n+1)$ th sphere's radius to be inserted into the packing, writing an exact expression:

$$P_{\text{ins}}(r; n) = \frac{\int dV \delta(D_n(\vec{x}) - r)}{\int dV} \quad (\text{A.6})$$

where the integrals are over the pore space, and $D_n(\vec{x})$ is the distance from the point \vec{x} to the closest pore boundary after n spheres have been inserted. In the limit of very small radii this integral may be solved exactly as:

$$\lim_{r \rightarrow 0} P_{\text{ins}}(r; n) = \frac{S(n)}{\Phi(n)} \quad (\text{A.7})$$

where $S(n)$ and $\Phi(n)$ are the surface area and available pore space in the existing in packing. They propose that $P_{\text{ins}}(r; n)$ can be modeled as a purely flat distribution,

$$P_{\text{ins}}(r; n) = \begin{cases} r_c^{-1} & \text{for } r < r_c \\ 0 & \text{for } r \geq r_c \end{cases} \quad (\text{A.8})$$

again verifying their assumptions using numerical simulations. From Eqn. A.7 and A.8, we see that

$$r_c = \Phi(n)/S(n). \quad (\text{A.9})$$

From $N(r; n)$ they determine $S(n)$ and $\Phi(n)$ as

$$S(n) = \frac{k\alpha V_d}{\alpha - d} r_c^{-(\alpha-d)} \quad (\text{A.10})$$

$$\Phi(n) = \frac{k\alpha V_d}{(d+1)(d+1-\alpha)} r_c^{d+1-\alpha} \quad (\text{A.11})$$

where as in Chapter 4, V_d is the volume of a unit radius sphere. Using Eqns. A.9, A.10 and A.11 they find an estimate of α as

$$\hat{\alpha} = d + \frac{d+1}{d+2}. \quad (\text{A.12})$$

While from Equations A.4 and A.11 they obtain the scaling relationship:

$$\Phi(n) \propto n^{-\beta} \propto n^{-(d+1-\alpha)/(\alpha-1)}, \quad (\text{A.13})$$

from which the relationship between α and β in $d = 2$ is:

$$\alpha = 1 + \frac{2}{1+\beta}. \quad (\text{A.14})$$

This equation is used in Chapter 4 to determine α . Note that while this scaling relationship is derived for spheres, it is valid for objects of any shape [32].

Appendix B

Additional data for RAP and RRAP simulations.

This appendix contains supplementary data from the packing limited growth models considered in Chapter 4. Tables of the values obtained for β , β' , α and α' are shown and graphs of the variation of α and α' .

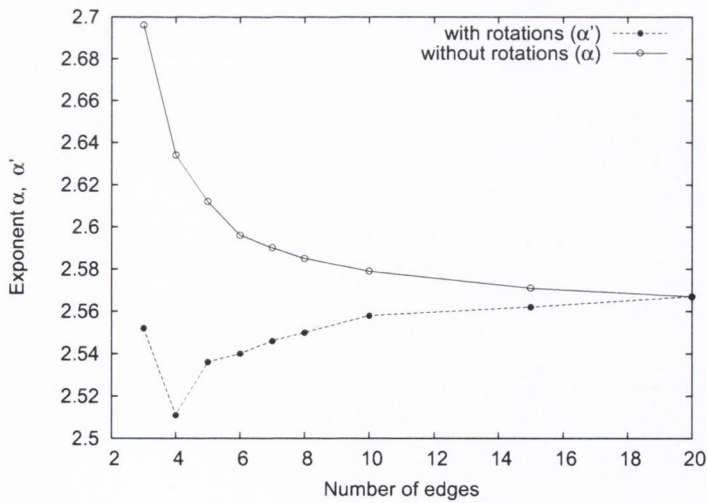


Figure B.1: Variation of exponents α and α' as the number of edges of the packed objects increases and the objects transition for a straight edged to a circular shape.

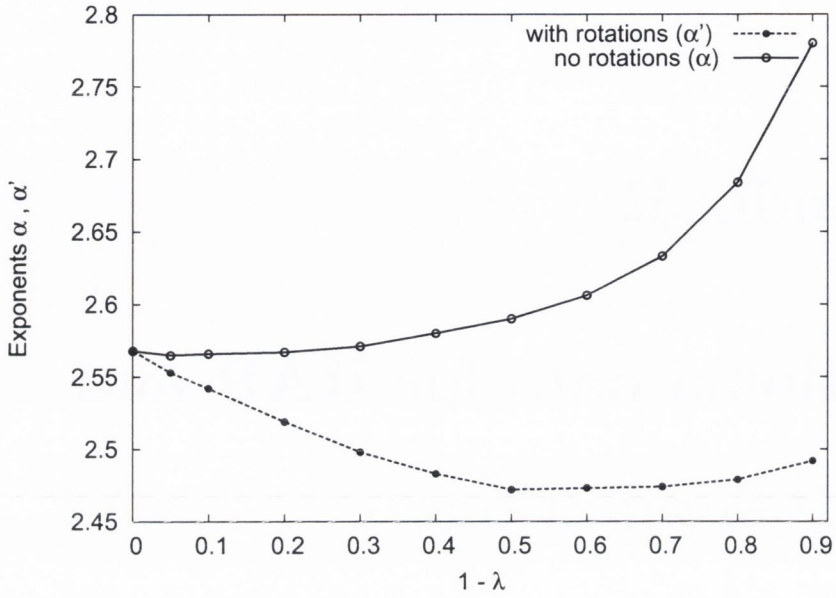


Figure B.2: Variation of exponents α and α' with ellipticity.

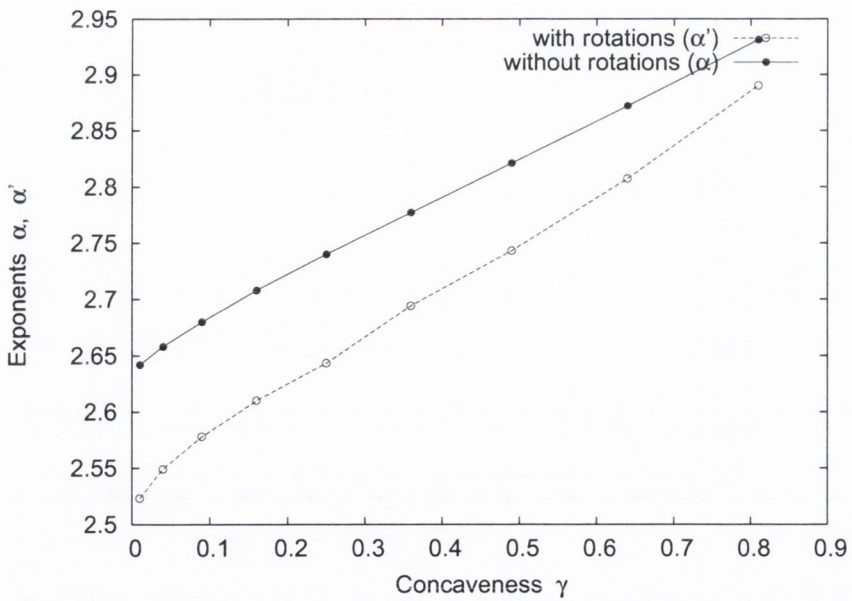


Figure B.3: Variation of exponents α and α' with the concaveness γ of the object.

n_{edge}	β	β'	α	α'
triangle	0.179(1)	0.288(2)	2.696(1)	2.552(2)
square	0.224(2)	0.323(2)	2.634(2)	2.511(2)
pentagon	0.241(1)	0.302(1)	2.612(1)	2.536(1)
hexagon	0.253(2)	0.299(2)	2.596(2)	2.540(2)
septagon	0.258(2)	0.294(2)	2.590(2)	2.546(2)
octagon	0.262(2)	0.291(2)	2.585(2)	2.550(2)
10-sided	0.267(2)	0.284(1)	2.579(2)	2.558(1)
15-sided	0.273(2)	0.280(2)	2.571(2)	2.562(2)
20-sided	0.275(2)	0.279(2)	2.567(2)	2.564(2)
circle	0.277(2)	-	2.566(2)	-

Table B.1: Variation of exponents β , β' , α and α' for the transition from straight edged to circular objects.

λ	β	β'	α	α'
1.000	0.276(1)	0.276(3)	2.568(1)	2.568(3)
0.950	0.278(1)	0.288(2)	2.565(1)	2.553(2)
0.900	0.277(2)	0.297(4)	2.566(2)	2.542(4)
0.800	0.276(1)	0.317(1)	2.567(1)	2.519(1)
0.700	0.273(1)	0.335(4)	2.571(1)	2.498(4)
0.600	0.266(1)	0.348(2)	2.580(1)	2.483(2)
0.500	0.258(1)	0.359(3)	2.590(1)	2.472(3)
0.400	0.245(1)	0.358(4)	2.606(1)	2.473(4)
0.300	0.225(1)	0.357(2)	2.633(1)	2.474(2)
0.200	0.188(1)	0.352(2)	2.684(1)	2.479(2)
0.100	0.124(1)	0.341(2)	2.780(1)	2.492(2)

Table B.2: Variation of exponents β , β' , α and α' with ellipticity λ .

γ	β	β'	α	α'
0.01	0.218(1)	0.313(2)	2.642(1)	2.523(2)
0.04	0.206(1)	0.292(2)	2.658(1)	2.549(2)
0.09	0.190(1)	0.267(2)	2.680(1)	2.578(2)
0.16	0.171(1)	0.242(2)	2.708(1)	2.610(2)
0.25	0.150(1)	0.217(2)	2.740(1)	2.643(2)
0.36	0.125(1)	0.181(2)	2.777(1)	2.694(2)
0.49	0.098(1)	0.148(2)	2.821(1)	2.743(2)
0.64	0.068(1)	0.107(2)	2.872(1)	2.807(2)
0.81	0.036(1)	0.058(2)	2.931(1)	2.890(2)

Table B.3: Variation of exponents β , β' , α and α' with concaveness γ .

Appendix C

Implementation of a Cell List

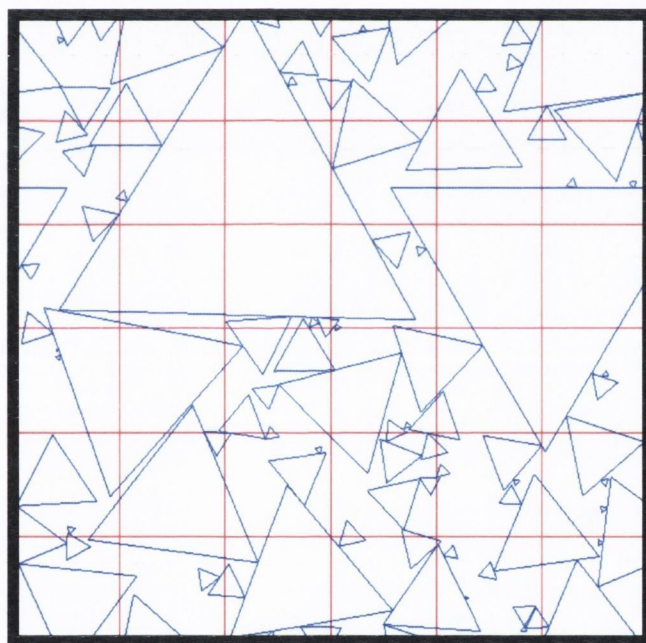


Figure C.1: RAP packing of triangles with the simulation box broken up into a number of smaller cells. In the example shown 36 cells are used, while in our RAP simulations of large systems we generally use 2074 cells.

The `ARBITRARYPACKER` software implements a cell list technique to greatly improve performance in PLG simulations where a large number of packed objects

21	22	23	24	25
16	17	18	19	20
11	12	13	14	15
6	7	8	9	10
1	2	3	4	5

Figure C.2: The simulation box is split up into a number of smaller cells. Each cell is given an index as shown.

are considered [102]. A cell list is a tool used to divide up the simulation box into smaller cells and to keep track of which cell each object's center is located within (See Figure C.1). Every cell is given an index and at the start of the simulation for every cell the indices of its neighbouring cells are determined. For example in figure C.2, cell 8 would have neighbours 2, 3, 4, 7, 9, 12, 13 and 14. So if an object is located in cell 8, to determine its interaction with other objects in the packing it is only necessary to loop over the objects located in the neighbouring cells. This of course gives a very large performance boost for large systems.

However, this simple application of the cell list, assumes that all objects have a maximum diameter equal to the cell diameter. For systems with a very large polydispersity, like those found in Chapter 4, this implementation needs to be modified. In this case we have done so by labeling those objects that have a diameter greater

than the cell diameter. When the interaction of a growing object with the existing packing needs to be determined, we loop over all the objects in the neighbouring cells and also all the objects that have been labelled as being larger than the cell diameter. The cell size is chosen so that in a PLG simulation involving up to 100,000 objects, only around 300 would be larger than the cell diameter. (This corresponds to breaking up the simulation box into 2074 cells.) The cell list gives an excellent performance increase, as without it as each object was added to the packing, we would need to check for contact interactions with up to 100,000 other objects.

Bibliography

- [1] Y. A. Andrienko, N. V. Brilliantov, and P. L. Krapivsky. Pattern-formation by growing droplets the touch-and-stop model of growth. *Journal Of Statistical Physics*, 75(3-4):507–523, 1994.
- [2] Y. A. Andrienko, N. V. Brilliantov, and J. Kurths. Complexity of two-dimensional patterns. *European Physical Journal B*, 15(3):539–546, 2000.
- [3] T. Aste. Circle, sphere, and drop packings. *Physical Review E*, 53(3):2571–2579, 1996.
- [4] T. Aste. Volume fluctuations and geometrical constraints in granular packs. *Physical Review Letters*, 96(1):018002, January 2006.
- [5] T. Aste, M. Saadatfar, A. Sakellariou, and T. J. Senden. Investigating the geometrical structure of disordered sphere packings. *Physica A-Statistical Mechanics And Its Applications*, 339(1-2):16–23, August 2004.
- [6] T. Aste, M. Saadatfar, and T. J. Senden. Geometrical structure of disordered sphere packings. *Physical Review E*, 71(6):061302, June 2005.
- [7] T. Aste and D. Sherrington. Glass transition in self-organizing cellular patterns. *Journal Of Physics A-Mathematical And General*, 32(41):7049–7056, October 1999.

- [8] T Aste and D Weaire. *The Pursuit of Perfect Packing*. Bristol and Philadelphia: IOP Publishing Ltd, 2000.
- [9] Grünbaum B and Shepard G C. *Tilings and Patterns*. W.H. Freeman and Company, 1987.
- [10] Ogborne B Bathurst R and Richfield J. The last word. *New Scientist*, 2211, 06 Nov 1999.
- [11] C. Bennet. Serially deposited amorphous aggregates of hard spheres. *Journal of Applied Physics*, 43(6):2727–2734, 1972.
- [12] J. D. Bernal and J. Mason. Co-ordination of randomly packed spheres. *Nature*, 188(4754):910–911, 1960.
- [13] J. G. Berryman. Random close packing of hard-spheres and disks. *Physical Review A*, 27(2):1053–1061, 1983.
- [14] K Brakke. *The Motion of a Surface by its Mean Curvature*. Princeton University Press, Princeton, NJ, 1978.
- [15] K Brakke. The surface evolver. *Experimental Mathematics*, 1:141, 1992.
- [16] F. P. Bretherton. The motion of long bubbles in tubes. *J. Fluid Mech.*, 10:166, 1961.
- [17] N. V. Brilliantov, P. L. Krapivsky, and Y. A. Andrienko. Random space-filling-tilingfractal properties and kinetics. *Journal Of Physics A-Mathematical And General*, 27(11):L381–L386, 1994.
- [18] F Bueche. *Principles of Physics*. McGraw-Hill Book Co., international student edition edition, 1986.

- [19] I. Cantat, R. Delannay, and N. Kern. Dissipation in foam flowing through narrow channels. *Europhysics Lett.*, 65(5):726–732, 2003.
- [20] O. Carvente and J. C. Ruiz-Suarez. Crystallization of confined non-brownian spheres by vibrational annealing. *Physical Review Letters*, 95(1):018001, 2005.
- [21] V Ceanga and Y Hurmuzlu. A new look at an old problem: Newton’s cradle. *Journal Of Applied Mechanics-Transactions Of The Asme*, 68:575–583, 2001.
- [22] Q. Chen and D. Y. Li. Computer simulation of solid particle erosion. *Wear*, 254(3-4):203–210, 2003.
- [23] H T Croft, K J Falconer, and R K Guy. *Unsolved Problems in Geometry*. Springer, 1991.
- [24] W Crummett and A Western. *University physics : models and applications*. Dubuque, IA :William C. Brown, 1994.
- [25] Opengl Architecture Review Board Dave Shreiner. *OpenGL(R) Reference Manual*. Addison-Wesley Professional, 1999.
- [26] P. G. de Gennes. Granular matter: a tentative view. *Reviews Of Modern Physics*, 71(2):S374–S382, 1999.
- [27] D. V. De Pellegrin and G. W. Stachowiak. Evaluating the role of particle distribution and shape in two-body abrasion by statistical simulation. *Tribology International*, 37(3):255–270, 2004.
- [28] D. V. De Pellegrin and G. W. Stachowiak. Simulation of three-dimensional abrasive particles. *Wear*, 258(1-4):208–216, 2005.
- [29] G. Delaney, D. Weaire, S. Hutzler, and S. Murphy. Random packing of elliptical disks. *Philosophical Magazine Letters*, 85(2):89–96, 2005.

- [30] G. W. Delaney, D. Weaire, and S. Hutzler. Onset of rigidity for stretched string networks. *Europhysics Letters*, 72(6):990–996, December 2005.
- [31] P. S. Dodds and J. S. Weitz. Packing-limited growth. *Physical Review E*, 65(5):056108, 2002.
- [32] P. S. Dodds and J. S. Weitz. Packing-limited growth of irregular objects. *Physical Review E*, 67(1):016117, 2003.
- [33] A. Donev, I. Cisse, D. Sachs, E. Vario, F. H. Stillinger, R. Connelly, S. Torquato, and P. M. Chaikin. Improving the density of jammed disordered packings using ellipsoids. *Science*, 303(5660):990–993, 2004.
- [34] A. Donev, F. H. Stillinger, P. M. Chaikin, and S. Torquato. Unusually dense crystal packings of ellipsoids. *Physical Review Letters*, 92(25):255506, 2004.
- [35] A. Donev, S. Torquato, F. H. Stillinger, and R. Connelly. Comment on "jamming at zero temperature and zero applied stress: The epitome of disorder". *Physical Review E*, 70(4):043301, October 2004.
- [36] A. Donev, S. Torquato, F. H. Stillinger, and R. Connelly. Jamming in hard sphere and disk packings. *Journal Of Applied Physics*, 95(3):989–999, 2004.
- [37] D Donnelly and Jb Diamond. Slow collisions in the ballistic pendulum: A computational study. *American Journal Of Physics*, 71:535–540, 2003.
- [38] U Dornbusch, R Williams, C Moses, and D Robinson. Life expectancy of shingle beaches: measuring in situ abrasion. *Journal of Coastal Research*, 36:249–255, 2002.
- [39] W. Drenckhan, S. J. Cox, G. Delaney, H. Holste, D. Weaire, and N. Kern. Rheology of ordered foamson the way to discrete microfluidics. *Colloids And Surfaces A-Physicochemical And Engineering Aspects*, 263(1-3):52–64, 2005.

- [40] B. Dubertret, T. Aste, H. M. Ohlenbusch, and N. Rivier. Two-dimensional froths and the dynamics of biological tissues. *Physical Review E*, 58(5):6368–6378, November 1998.
- [41] M. Durand, J. F. Sadoc, and D. Weaire. Maximum electrical conductivity of a network of uniform wires: the lemlich law as an upper bound. *Proceedings Of The Royal Society Of London*, 460(2045):1269–1284, 2004.
- [42] D. J. Durian. Foam mechanics at the bubble scale. *Physical Review Letters*, 75(26):4780–4783, 1995.
- [43] D. J. Durian. Bubble-scale model of foam mechanics: Melting, nonlinear behavior, and avalanches. *Physical Review E*, 55(2):1739–1751, February 1997.
- [44] J. A. Glazier and D. Weaire. The kinetics of cellular-patterns. *Journal Of Physics-Condensed Matter*, 4(8):1867–1894, 1992.
- [45] H Gould and J Tobochnik. *An Introduction to Computer Simulation Methods: Applications to Physical System*. Pearson Education POD, 2nd edition edition, 1996.
- [46] T Green and P Grassia. In preperation.
- [47] T. C. Hales. Sphere packings .1. *Discrete & Computational Geometry*, 17(1):1–51, 1997.
- [48] A.E. Hawkins. *The Shape of Powder-Partice Outlines*. John Wiley & Sons Inc., 1993.
- [49] F Herrmann and P Schmalzle. Simple explanation of a well-known collision experiment. *American Journal Of Physics*, 49:761–764, 1981.
- [50] F Herrmann and M Seitz. How does the ball-chain work. *American Journal Of Physics*, 50:977–981, 1982.

- [51] H. J. Herrmann, G. Mantica, and D. Bessis. Space-filling bearings. *Physical Review Letters*, 65(26):3223–3226, 1990.
- [52] E.J. Hinch and S. Saint-Jean. The fragmentation of a line of balls by an impact. *Proceedings Of The Royal Society Of London Series A-*, 455:3201–3220, 1999.
- [53] S. Hutzler, G. Delaney, D. Weaire, and F. MacLeod. Rocking newton’s cradle. *American Journal Of Physics*, 72(12):1508–1516, 2004.
- [54] S. Hutzler, D. Weaire, and R. Crawford. Moving boundaries in ordered cylindrical foam structures. *Philosophical Magazine B-Physics Of Condensed Matter Statistical Mechanics Electronic Optical And Magnetic Properties*, 75(6):845–857, June 1997.
- [55] H. M. Jaeger, S. R. Nagel, and R. P. Behringer. Granular solids, liquids, and gases. *Reviews Of Modern Physics*, 68(4):1259–1273, 1996.
- [56] L. P. Kadanoff. Built upon sand: Theoretical ideas inspired by granular flows. *Reviews Of Modern Physics*, 71(1):435–444, 1999.
- [57] K. Kawasaki, T. Nagai, and K. Nakashima. Vertex models for two-dimensional grain-growth. *Philosophical Magazine B*, 60(3):399–421, 1989.
- [58] N. Kern, D. Weaire, A. Martin, S. Hutzler, and S. J. Cox. Two-dimensional viscous froth model for foam dynamics. *Physical Review E*, 70(4):041411, 2004.
- [59] T. Kinoshita, T. Wenger, and D. S. Weiss. A quantum newton’s cradle. *Nature*, 440(7086):900–903, April 2006.
- [60] R. Korner and D. Stoyan. Modeling abrasion processes by operations of mathematical morphology. *Particle & Particle Systems Characterization*, 16(2):66–70, 1999.

- [61] Bragg L. and Nye J. F. *Proc. R. Soc. London Soc. A.*, 90:474–482, 1947.
- [62] M. D. Lacasse, G. S. Grest, and D. Levine. Deformation of small compressed droplets. *PHYSICAL REVIEW E*, 54(5):5436–5446, November 1996.
- [63] L Landau and E Lifshitz. *Theory of Elasticity (Course of Theoretical Physics)*, volume Vol. 7. Oxford, New York, Pergamon Press, 2nd english ed. edition, 1970.
- [64] P. B. Landon, C. L. Gilleland, B. Jarvis, B. D. Waters, K. Inoue, and R. Glosser. Self-assembly of colloidal silica into opals with large ordered single crystals. *Colloids And Surfaces A*, 259(1-3):31–33, May 2005.
- [65] A. J. Liu and S. R. Nagel. Nonlinear dynamics : Jamming is not just cool any more. *Nature*, 396(6706):21–22, 1998.
- [66] A J Liu and S R Nagel. *Jamming and Rheology*. London, New York: Taylor and Francis, 2001.
- [67] FRS Lord Rayleigh. The ultimate shapes of pebbles, natural and artificial. *P Roy Soc Lond A Mat*, 181:107, 1942.
- [68] W. N. Man, A. Donev, F. H. Stillinger, M. T. Sullivan, W. B. Russel, D. Heeger, S. Inati, S. Torquato, and P. M. Chaikin. Experiments on random packings of ellipsoids. *Physical Review Letters*, 94(19):198001, May 2005.
- [69] S. S. Manna. Space filling tiling by random packing of disks. *Physica A*, 187(3-4):373–377, 1992.
- [70] S. S. Manna and H. J. Herrmann. Precise determination of the fractal dimensions of apollonian packing and space-filling bearings. *Journal Of Physics A-Mathematical And General*, 24(9):L481–L490, 1991.

- [71] J C Maxwell. *A Treatise on Electricity and Magnetism*. Oxford (1891) reprinted by Dover, New York (1954), 1891.
- [72] E Mazur. *Peer Instruction - A User's Manual*. Prentice Hall, New Jersey, 1997.
- [73] W. W. Mullins. 2-dimensional motion of idealized grain boundaries. *Journal Of Applied Physics*, 27(8):900–904, 1956.
- [74] A Murta. The general polygon clipper library used to determine the overlap of objects in ARBITRARYPACKER is available for download from: <http://www.cs.man.ac.uk/aig/staff/alan/software/>.
- [75] D. R. Nelson, M. Rubinstein, and F. Spaepen. Order in two-dimensional binary random arrays. *Philosophical Magazine A-Physics Of Condensed Matter Structure Defects And Mechanical Properties*, 46(1):105–126, 1982.
- [76] J Neumann. Metal interfaces. *American Society for Metals*, page 108, 1952.
- [77] J. R. Nicholls and D. J. Stephenson. Monte-carlo modeling of erosion processes. *Wear*, 186(1):64–77, 1995.
- [78] H Ohanian. *Principles of Physics*. W.W. Norton & Company, Inc., first edition edition, 1994.
- [79] C. S. O'Hern, S. A. Langer, A. J. Liu, and S. R. Nagel. Jamming. *The American Chemical Society*, 223:U452–U452, 2002.
- [80] C. S. O'Hern, S. A. Langer, A. J. Liu, and S. R. Nagel. Random packings of frictionless particles. *Physical Review Letters*, 88(7):075507, 2002.
- [81] C. S. O'Hern, L. E. Silbert, A. J. Liu, and S. R. Nagel. Jamming at zero temperature and zero applied stress: The epitome of disorder. *Physical Review E*, 68(1):011306, 2003.

- [82] C. S. O'Hern, L. E. Silbert, A. J. Liu, and S. R. Nagel. Reply to "comment on 'jamming at zero temperature and zero applied stress: The epitome of disorder'". *Physical Review E*, 70(4):043302, 2004.
- [83] T. Okuzono and K. Kawasaki. Intermittent flow behavior of random foams: a computer experiment on foam rheology. *Physical Review E*, 51(2):1246–1253, 1995.
- [84] G. Y. Onoda and E. G. Liniger. Random loose packings of uniform spheres and the dilatancy onset. *Physical Review Letters*, 64(22):2727–2730, 1990.
- [85] O. Pouliquen, M. Nicolas, and P. D. Weidman. Crystallization of non-brownian spheres under horizontal shaking. *Physical Review Letters*, 79(19):3640–3643, 1997.
- [86] M Reinsch. Dispersion-free linear-chains. *American Journal Of Physics*, 62:271–278, 1994.
- [87] H. J. Schope. Formation of dried colloidal monolayers and multilayers under the influence of electric fields. *Journal Of Physics-Condensed Matter*, 15(33):L533–L540, August 2003.
- [88] R. J. Speedy. On the reproducibility of glasses. *Journal Of Chemical Physics*, 100(9):6684–6691, May 1994.
- [89] M Sternheim and J Kane. *General Physics*. John Wiley & Sons, second edition, 1991.
- [90] H. T. C. Stoof. Quantum physics - equilibrium on hold. *Nature*, 440(7086):877–878, April 2006.
- [91] M. Sullivan, K. Zhao, C. Harrison, R. H. Austin, M. Megens, A. Hollingsworth, W. B. Russel, Z. D. Cheng, T. Mason, and P. M. Chaikin. Control of colloids

- with gravity, temperature gradients, and electric fields. *Journal Of Physics-Condensed Matter*, 15(1):S11–S18, 2003.
- [92] M. Tanemura and T. Matsumoto. Density of the p2gg-4c1 packing of ellipses .1. *Zeitschrift Fur Kristallographie*, 212(9):637–647, 1997.
- [93] J. M. Thijssen. *Computational Physics*. Cambridge University Press, 1999.
- [94] M. F. Thorpe, M. Lei, A. J. Rader, D. J. Jacobs, and L. A. Kuhn. Protein flexibility and dynamics using constraint theory. *Journal Of Molecular Graphics & Modelling*, 19(1):60–69, 2001.
- [95] J. Tobochnik and P. M. Chapin. Monte-carlo simulation of hard-spheres near random closest packing using spherical boundary-conditions. *Journal Of Chemical Physics*, 88(9):5824–5830, May 1988.
- [96] S. Torquato, T. M. Truskett, and P. G. Debenedetti. Is random close packing of spheres well defined? *Physical Review Letters*, 84(10):2064–2067, 2000.
- [97] F L Toth. *Bull. Am. Math. Soc.*, 70:468–481, 1964.
- [98] A. van der Net. Private communication.
- [99] A. van der Net, W. Drenckhan, I. Weaire, and S. Hutzler. The crystal structure of bubbles in the wet foam limit. *Soft Matter*, 2(2):129–134, February 2006.
- [100] Marvin J W. The shape of compressed lead shot and its relation to cell shape. *Am. J. Bot.*, 26:280–8, 1939.
- [101] Nowacki W. *Schweiz. Miner. Petrog. Mitt.*, 28:502, 1948.
- [102] W.T. Vetterling W. H. Press, S. A. Teukolsky and B. P. Flannery. *Numerical Recipes in C*. Cambridge University Press, 1988.

- [103] Z. U. A. Warsi. *Fluid Dynamics: Theoretical and Computational Approaches*. CRC Press, 1998.
- [104] D. Weaire and S. Hutzler. *The Physics of Foams*. Oxford, 1999.
- [105] D. Weaire and S. McMurry. Some fundamentals of grain growth. *Solid State Physicsadvances In Research And Applications, Vol 50*, 50:1–36, 1997.
- [106] D. Weaire and R. Phelan. A counterexample to kelvin conjecture on minimal-surfaces. *Philosophical Magazine Letters*, 69(2):107–110, February 1994.
- [107] S. R. Williams and A. P. Philipse. Random packings of spheres and spherocylinders simulated by mechanical contraction. *Physical Review E*, 67(5):051301, 2003.
- [108] J. M. Wills. Spheres and sausages, crystals and catastrophesand a joint packing theory. *Mathematical Intelligencer*, 20(1):16–21, 1998.
- [109] J Wilson and A Buffa. *College Physics*. Prentice-Hall Inc., Upper Saddle River, New Jersey, 07458, 4th edition edition, 2000.
- [110] D Wolf. *Computational Physics*, chapter Modelling and computer simulation of granularmedia, pages 64–95. Springer-Verlag Berlin, 1996.
- [111] Z. C. Zhou, B. Joos, and P. Y. Lai. Elasticity of randomly diluted central force networks under tension. *Physical Review E*, 68(5):055101, November 2003.
- [112] J. X. Zhu, M. Li, R. Rogers, W. Meyer, R. H. Ottewill, W. B. Russell, and P. M. Chaikin. Crystallization of hard-sphere colloids in microgravity. *Nature*, 387(6636):883–885, June 1997.